THE UNIVERSITY OF MICHIGAN

COLLEGE OF ENGINEERING
Department of Aeronautical and Astronautical Engineering
Aircraft Propulsion Laboratory

DEVELOPMENT AND OPERATION OF AN ARC HEATED HYPERSONIC TUNNEL

P. M. Sherman, Project Supervisor

ORA Project 02953

under contract with:

Department of the Navy
Office of Naval Research
Mathematical Sciences Division
Washington, D. C.
Contract No. Nonr-1224(31) NR 061-108

administered through:

OFFICE OF RESEARCH ADMINISTRATION ANN ARBOR

July 1963

TABLE OF CONTENTS

LIST OF FIGURES

LIST OF FIGURES (continued)

LIST OF FIGURES (continued)

1.0 INTRODUCTION

The many problems connected with hypersonic flight (some common to both lifting vehicles and ballistic systems), have sustained the interest in experimental facilities for the study of these problems. Simulation of flight conditions at high velocities and moderate altitudes requires a facility which will provide both high stagnation temperatures and pressures. While this is an aim of the subject facility, there are two added reasons for achieving the high stagnation pressure. A high stagnation pressure minimizes the effects of freezing the gas composition in the nozzle expansion process, and provides an increased test section density. (The point at which freezing occurs has been shown to be a strong function of pressure.) The increased density obtained, at a given Mach number, facilitates test section measurements by minimizing rarefaction difficulties. Optical techniques become more feasible and fruitful.

Most present hypersonic facilities operate at the minimum stagnation temperatures necessary to avoid condensation. This means that operating conditions, when stated in terms of altitudes, often mean density altitude rather than actual conditions at the given altitude. If simulated free stream temperature is desired for the very high Mach number region, a stagnation temperature considerably higher than that merely to prevent condensation is required.

Obtaining a very high stagnation temperature even at a moderate density becomes a problem. Obtaining the combined high temperature with a very high pressure becomes even more of a problem. Given the energy transfer necessary to obtain the extreme conditions, there is still the problem of containing the working fluid. When extreme temperatures are involved, arc heating immediately suggests itself, since extreme temperatures are characteristic of arc columns. Electrical energy can also be stored easily and can be released rapidly and locally, with the desired high temperature resulting.

Since high velocity means high energy, and energy is expensive, laboratory facilities must have a limited run time for economy reasons. In particular, this suggests some blow-down arrangement or short pulse design.

Like all facilities the hotshot represents a compromise. It is possible to obtain a relatively long run time (50 msec) as well as high stagnation temperatures and pressures. The inductance type hotshot represents a comparatively safe and economical large energy facility. The blow down arrangement permits the use of different working fluids.

This report summarizes some of the work done in connection with the design and operation of the facility. It does not, however, repeat the design considerations discussed at length in Reference 1.

2.0 FACILITY DESCRIPTION

a. General Layout

A plan view of the laboratory layout is shown in Figure 1. The major components are the energy supply system, which includes motor, generator and coil; arc chamber; nozzle-test section; vacuum tank. The new section of building constructed to house the facility included several special features. Perhaps the most important of these are the extremely heavy concrete isolated mounting pads for optical equipment. These are 15 in. thick and each has 12-12 in. diameter column footings which go 10 ft into the ground. (Vibration has been the limiting factor on the sensitivity of some optical systems of a similar type. The special construction should eliminate this problem.) Special floor mountings were constructed for the energy supply and the arc chamber. The energy supply (except the coil) is bolted down as is the arc chamber. The other components are free to move.

Personnel protection was based on the philosophy that energy should be absorbed rather than deflected, and to be most effective the protection should be close to the source and/or close to the personnel (rather than half-way in between). Along these lines sand bags were placed close to the areas where the highest pressures are developed and sand-filled walls were used for the tunnel control cubicle.

b. Energy Supply

Large amounts of energy must be supplied to the working fluid in order to obtain high velocities. The energy is obtained by storing it over a long period of time and discharging it over a short period of time. The energy is taken from an ordinary small motor and first stored as kinetic energy of a heavy flywheel. It is then restored in the magnetic field of a large coil, charged by a unipolar generator. A schematic of the circuit is shown in Figure 2.

The motor brings the flywheel-rotor of the unipolar generator up to a maximum speed of 10,000 rpm. At this speed the kinetic energy stored is 20×10^6 joules. The period of time for this to occur is about 15 minutes. The field of the unipolar generator is then turned on (by closing switch S_1), and current is built up in the coil. When peak current is reached, in about 3 seconds, switch S_2 is opened and current is transferred to the arc-chamber electrode part of the circuit. S_3 is a fuse-switch arrangement designed to carry current until switch S_2 is completely opened. When current builds up in S_2, a combination of resistance heating and magnetic forces force it open. An arc is thereby initiated, resulting in a high voltage and fast dissipation of current (about 10 milliseconds), thus heating the gas in the arc chamber, increasing temperature and pressure to the required values.

The coil is designed to store 6×10^6 joules at the peak design current of 315,000 amperes. Design of the coil-energy storage system is described in Reference 1. It is based on an Allis-Chalmers unipolar generator which is rated to deliver 60,000 amperes continuously but was installed for pulsed operation with a peak current of 500,000 amperes at 45 volts. (Somewhat minor modifications had to be made to the generator installation, both mechanical and electrical, after the system was initially checked out.) The current level is controlled by both generator field current level and flywheel rpm. Ordinarily less than 1/3 of the energy stored in the flywheel is transferred to the coil so that the rpm decreases about 25% during the run. Figure 3 shows a

photograph of the energy supply system. The units are numbered in accordance with those in Figure 1.

The sand bags which appear on the top of the coil in Figure 3 were placed there to keep the top cables of the coil from bouncing up. During the run, when current is passed through the coil, the parallel conductors tend to squeeze together, decreasing the total cross sectional area of the coil, and increasing the overall average coil diameter. During the rapid decay of the current the compressed insulation tends to make the coil cables fly apart.

Originally omission of fuse-switch S_3 (Figure 2) and initiation of an arc directly across the electrodes, was considered. If this is done, switch S_2 must completely break a circuit carrying up to 300,000 amperes. That would mean that there is always a danger of extended arcing at switch S_2 instead of inside the arc chamber. The latter problem is eliminated by use of the fuse-switch S_3 which is designed to carry current for a short period of time, until switch S_2 is open enough to prevent arcing across its contacts. Switch S_2 then is a transfer switch rather than a breaker and switch S_3 becomes the breaker (this idea was originally employed at AEDC Tullahoma). Ideally, switch S_2 should be omitted completely. However, that is not possible because of the small size of the arc chamber and the comparatively long current build up time in the coil. It was possible to design a small switch to carry a large current for milliseconds but not for seconds. With the double switch arrangement it is still necessary to open the transfer switch rapidly (about 5 in. in 10×10^{-3} sec). A compressed air cylinder (1500 psia) with nylon-piston-solenoid valve arrangement is used for the purpose. The circuit employed is shown in Figure 4 and a photograph of the switch is shown in Figure 5. The design considerations for the fuse-switch S_2 is discussed in Appendix A. The external electrodes shown in Figure 5 were used to develope the switching system.

Connection between the generator and coil is made by means of two solid aluminum bus bars, 4 x 20 in. in cross section, on 7.5 in. centers. The connections between the transfer switch and the arc chamber is made by similar bars, but placed on 4.25 in. centers, plus vertical copper connecting bars

(4 x 5 in. cross section) clamped to a section of copper coaxial bus which becomes the coaxial electrodes in the arc chamber. Insulation is made up of layers of mylar and cardboard.

The solid aluminum bars were employed for economy. (Laminated bars used at other high current facilities have many advantages.) Two considerations are important in the design of the bus bars. One is the inductance of the bars, the other is the forces between parallel conductors carrying high currents. Both the coaxial arrangement and the parallel plate arrangement basically permit minimizing inductance. Parallel bars must be close together to minimize inductance and far apart to minimize repulsive forces. The present design must withstand repulsive forces computed to be up to 15,000 lbs/ft at 300,000 amperes. The computed inductance of the generator coil connection is less than about 3×10^{-6} henries, of the switch-electrode connection, also less than about 3×10^{-6} henries. (The resistance of the vertical bus bars plus coaxial bus bars is about 25×10^{-6} ohms, neglecting contact resistance.)

Current measurement is made by means of a Halltron Current Transducer. It is a semi-conductor (about 1/2 in. square x 1/32 in. thick) whose Hall effect output is employed. The circuit is shown in Figure 6. Arc voltage is indicated in two ways as shown in Figures 2 and 6.

When two large solid surfaces are in contact to provide for an electrical connection, if only one point on the surface provides the actual contact, the high current approaching the point in one conductor has a large component in the same direction as the current in the mating conductor. This will result in a large repulsive force between the two conductors for large total currents. It is therefore important to maintain contacts which "guarantee" more than one point of actual contact—such as the "fingers" used on switches. All of the connections on the subject facility employ fingers, a series of screws, threaded connections or soft silver shims.

c. Arc Chamber

The maximum anticipated energy transfer to the gas was judged to be 2×10^6 joules. For a given energy transfer, the stagnation chamber becomes smaller as the stagnation conditions become more extreme. Also, as the chamber becomes smaller, the decay of stangation conditions with run time becomes greater unless the throat size is correspondingly decreased. Of course, the more extreme the stagnation conditions, particularly pressure, the more expensive the chamber. The design point of 80,000 psi for a 60 $in.^3$ chamber represents a compromise, considering throat size, decay of stagnation conditions and cost. (Cost of fabrication increases very rapidly for pressures exceeding about 60,000 psia.)

A cylindrical shape was chosen as most feasible. For the given power input and small chamber size, the surface of the chamber is so small that radial holes for transducers, electrodes, charging port, or "dump" port become necessary. That is, there is not enough space in the ends of the cylinder for all necessary inserts. This is a disadvantage in a high pressure chamber, since the hoop stress is greatly increased by the existence of radial holes. Radial holes result in stress concentrations near the hole and therefore should be avoided if at all possible. The hoop stress on the inner surface of a cylindrical chamber under pressure, is of course larger than the internal pressure. Only in the limit, for an infinitely thick wall does the maximum hoop stress become equal to the internal pressure. Radial holes increase the maximum stress, so that for a chamber with radial holes, the maximum stress far exceeds the internal pressure.

The design arrived at, as shown in Figure 7, included three small radial holes. The design was based on Lame's equation, that is, the exact solution for an elastic thick-walled cylinder. Stress concentrations at the radial holes were considered in terms of a modified stress concentration factor based on the exact solution for the stress distribution at a hole in an infinite slab, since no solution exists for the actual case of a cylinder.

The high stress concentrations combined with the limited strength of available materials meant that pre-stressed shells would have to be employed. The greater the number of shells employed, the more uniform the stress distribution. However, cost of fabrication increases rapidly with number of shells so that a minimum number of shells for the best available material represented the best compromise. This resulted in three shells with initial and final stress distributions as derived in Appendix B. The final distribution is the maximum stress at a hole resulting from 80,000 psi internal pressure superposed on the initial stress due to shrinking. The shrink fit pressure was first obtained for the inner two shells which are then considered one shell to determine the shrink-fit pressure for the outermost shell. The necessary interference between shells is then computed based on an ultrasonic measurement of modulus of elasticity. The pre-stressing is accomplished by heating the outer shell and slipping it over the inner and letting it cool.

Structural problems due to high stagnation temperatures are minimized by a short operating time. In addition a liner is employed to insulate the basic structure from the hot gas without the liner itself providing any structural support. Ideally the surface of such a liner should not melt or sublimate.

Studies were made (see Appendix C) to determine the heat transfer to the arc chamber under a few typical initial conditions. Two problems were considered: (1) conduction and radiation to the inside walls of the arc chamber liner, and (2) forced convection to a radial port insert. Since the determination of heat transfer rates depends upon a knowledge of the time varying gas properties while the tunnel blows down, an analysis was first made to determine the effects of variation from the perfect gas laws, and energy loss by radiation, on the gas properties themselves.

The surface temperature of the liner as a result of conduction only was computed using a simplified model. If the gas is assumed to act like an infinitely long solid with the proper thermal diffusivity, then conduction to a copper liner results in a surface temperature rise of only a few hundred degrees at the most extreme stagnation conditions. The liner temperature resulting from radiation

is a more severe problem. A simplified model was employed to compute the temperature one could expect. Radiation from the gas was assumed to be completely absorbed by the wall and wall re-radiation was neglected. It can be shown that for the short time involved, the cylindrical solution simplifies to that for an infinite one dimensional slab. The expression for the net radiative heat transfer simplifies for the case of a gas at high density and temperature radiating to a black walled container at a low temperature relative to the gas temperature, to the Stefan-Boltzman law. If the decay of stagnation conditions with time, due both to mass outflow through the throat and radiative heat transfer to the wall, is considered, then the increase in liner wall temperature is not prohibitively high. For a gas temperature of $10,000^{\circ}K$ at an initial density of 8 lbs/ft^3 the outside wall temperature of a 1/2 in. thick copper liner increases less than $100^{\circ}K$. The temperature of the inside surface of the liner goes through a maximum ($\sim 1500^{\circ}K$) very rapidly (in about 10 milliseconds) and decays rapidly. The copper liner at ~ 1/16 in. depth reaches a temperature peak ($900^{\circ}K$) more slowly (in ~ 50 milliseconds) and decays more slowly. The "radiation heat pulse" broadens, becoming very flat as the outside surface of the liner is reached. A liner of somewhat higher conductivity would make the peak liner temperature lower and result in somewhat higher temperature at the outer surfaces.

In addition to protecting the arc chamber pressure shell from exposure to the hot gas, the liner acts as the outer electrode for the coaxial electrode arrangement. A change in the liner dimensions also allows some change in internal volume without alteration to the arc chamber shell, and a resultant change in stagnation conditions. Clearance between the liner and the arc chamber shell is kept small enough so that the liner will not expand beyond its elastic limit even at peak design pressure. The material chosen for a combination of good conductivity and high compressive strength was a hardened beryllium copper alloy (about 50% the conductivity of copper with a proportional limit of ~ 80,000 psia.) The liners for the radial holes are of steel; press fit into the holes.

In addition to the structural problems in dealing with a high temperature high pressure gas, there is also a sealing problem to prevent leakage of hot gas which can cause damage to the chamber structure. The seals, tested hydraulically to 100,000 psia, employ a combination of o-ring and steel wedge rings. The o-ring seals at low pressure and puts the initial load on the steel wedge rings. In addition, the o-rings are removed from the inside surface of the chamber so that gas between baffling surfaces as well as the surfaces themselves provide some protection from the hot gas and the arc column.

For operations at extreme temperature and pressure conditions a quick exhaust valve to minimize chamber damage becomes essential. Such a valve must be fast acting to be effective. The design employed is shown in Figure 8. An ordinary detonation cap is employed to rupture a diaphragm. The second diaphragm which provides the seal is then ruptured by the pressure in the chamber. The advantage of this arrangement is simplicity. The two diaphragms combined this way, act as one of a thickness equal to the two together. The thickness of the top diaphragm which can be easily ruptured by the cap, is enough to withstand considerably more than one-half the maximum chamber pressure by itself. The second diaphragm is then thinner than that required to withstand one-half the chamber pressure. There should therefore be reasonable surety of diaphragm rupture and consequent quick exhaust. The cap is placed in the mounting in an upside-down position so that it more efficiently blows outward, with the direction of the exhaust, to minimize detrimental effects to the inside of the arc chamber. The cap is triggered by a sensing coil placed inside the energy storage coil. During the discharge in the arc chamber the rapid decay of current in the energy storage coil induces a signal ($\sim$ 40 volts) in the sensing coil which in turn is transferred to a delay circuit set so that the detonation cap will receive $>$ 5 amperes, a given time ($\sim$ 35 msec) after the signal resulting from the current discharge. Figures 9 and 10 show the circuits employed. The dump valve exhausts to the roof through a 6 in. pipe.

For insulation between inner and outer electrode epoxy-glass was chosen for operation at high pressures. Natural mica is used to take the large axial load on the inner electrode. For moderate pressures, delrin and nylon are used. There is one very good ground made at the arc chamber. Any other grounds are avoided.

A baffle is placed in front of the throat entrance as shown in the sketch of Figure 7. The baffle reduces the amount of contamination in the flow and prevents the arc column from entering the throat area.

A mylar diaphragm is placed as shown in Figure 7, for operation at moderate conditions. For the more extreme pressures, there is provision for a larger metal diaphragm or a nylon plug may be used instead. (The latter method has been used in a free jet expansion study.)

Figure 11 shows a photograph of the arc-chamber mounted in its cradle with its parts laid out. The chamber and cradle move on tracks and are locked to the stand by means of a conical plug inserted into a conical hole in a "center-board". The stand is bolted into channels in the floor constructed for the purpose.

As shown in Figure 7 the throat section is replaceable and the initial part of the nozzle is part of the arc chamber. Figure 12 shows the arc chamber, the arc-chamber nozzle-test section arrangements, and the vertical dump valve exhaust pipe.

d. Nozzle Test Section

In the abstract, if any amount of energy can be added to the stagnation chamber fluid, any corresponding velocity should be obtainable by expanding through a nozzle. The "real-gas" expansion through a nozzle, however, limits this process. Some of the energy transferred to the stagnation gas is "frozen" in it. That is, it is not recovered in the form of kinetic energy. In addition, the boundary layer growth may be such that the displacement thickness increases faster than the nozzle radius, and a more rapid increase of the nozzle radius may cause boundary layer separation in the nozzle, with a resultant

decrease in effective nozzle radius. Several aspects of the boundary layer problem are discussed in a separate report, Reference 3.

A conical nozzle was chosen for versatility, simplicity and economy. The total included angle of 15^{o} was a compromise between a small angle for minimum gradients in the axial direction, as well as minimum possibility boundary layer separation, and a large angle for minimum boundary layer thickness or maximum uniform core diameter. It now appears that the angle could have been increased without any danger of separation. Nozzle area ratios are changed by changing the nozzle throat section diameter. The throat is designed as a cylindrical section so the true constant cone angle is maintained, when the diameter of the throat is varied from ~ .02 in. to ~ .15 in. The throat sections used have been of beryllium copper and tungsten. For the less extreme temperatures, commercial copper should work well.

The test section is in the nozzle itself at a station where the nozzle is ~ 19 in. in diameter, so that the nozzle is quite short (~ 6 feet from throat to test section). Windows (1 1/4 in. thick) 15 in. in diameter provide for a 12 in. schlieren view. Closures to replace the windows were provided for an uninterrupted inside conical surface when desired.

The nozzle-test section is in one section mounted on wheels for easy removal. Provision was made for mechanically isolated model support as well as model lead access ports; in the tank just downstream of the test section. The test section-nozzle can be removed without interfering with the model. Alternate test sections (such as a cylindrical one built recently for the study of underexpanded jets), can easily be inserted without undue cost.

e. Vacuum System

The 400 ft^3 vacuum section pumped down by a Stokes rotary pump—10 in. diffusion pump combination was described in Reference 1. A heavy iron mesh "catcher" was placed near the downstream end of the vacuum tank. The effect of this porous surface on the starting shock has not been determined.

A vacuum reference and calibration system was designed and built with a small chamber, separate mechanical pump, small diffusion pump, and a McLeod gage with refrigerated trap as a primary reference. Thermocouple gages and ionization gages are used in the large vacuum system. An Alphatron is very convenient and does excess duty for many kinds of interim checks.

Figures 13 and 14 show the tunnel looking south and north respectively. Figure 15 shows the instrument-control room enclosure. It is insulated and connected to the one common ground.

3.0 OPERATING CONDITIONS AND MEASUREMENTS MADE

Computed design operating limitations were discussed in Reference 1 for up to a maximum energy transfer to the gas of 2×10^6 joules. This assumed an efficiency of energy transfer from the coil of about 30%. The initial operating conditions were in the region of 15,000 psia stagnation pressure and $3000^{\circ}K$ stagnation temperature with nitrogen as the working gas. At these conditions the efficiency appears to be close to 50%. The percent efficiency should not alter appreciably since the major part of the loss would be at the switch, and for a given circuit would remain a given proportion of the total energy stored in the coil. The maximum stagnation condition would then be somewhat higher than those shown in Reference 1. Figure 16 shows approximate stagnation conditions as a function of energy transfer.

The air data were taken from Reference 6. For densities above 100 times atmospheric density intermolecular forces become important and an equation of state is not available. This region of the curves in Figure 16 was extrapolated from the lower values. The nitrogen data were taken from Reference 7 which takes intermolecular forces into consideration and extends into the higher density region. As can be seen in Figure 16 the stagnation conditions for nitrogen differ considerably from that of air, for a given energy transfer, at the more extreme conditions.

Although any good determination of test section conditions must be made by test section measurements rather than computations based on stagnation chamber measurements, initially, pressure measurements made were used to determine free stream Mach number assuming isentropic flow through the nozzle.

The computer program employed by VKF, AEDC, Tullahoma, sometime ago (Reference 4) (since replaced by one based on a heat transfer measurement), was employed to calculate free stream Mach number. It is not a good calculation since it assumes an overall average temperature in the arc chamber based on constant volume heat transfer, and equilibrium isentropic flow through the nozzle. (The sample calculations in Reference 4 show a total temperature behind a normal shock to be in some cases greater than stagnation chamber stagnation temperature by as much as 9%. This appears to be lack of accuracy in the calculation which is based on empirical expressions, rather than a program error.)

The stagnation pressure in the arc chamber was measured by means of a Kistler No. 601 crystal transducer with a high pressure adaptor and non-magnetic housing. The total pressure behind a shock was recorded by means of a variable reluctance differential gage (in the range 0 - 1/2 psia and 0 -3 psia) of the type made by Hidyne (Reference 5) with Hidyne amplifiers and recorded on a CEC oscillograph.

The differential type pressure transducer was mounted close to the opening of a pitot tube and at right angles to it. One side of the transducer was connected to the vacuum reference. (Immediately after the run there is time to open it to the test section pressure so that the transducer does not see the final differential pressure of one atmosphere to the reference vacuum system.) The gages are calibrated immediately before and after each set of measurements.

Figure 17 is a photograph of an early oscillograph trace showing typical traces of current, voltage and arc chamber pressure, as well as one blunt body stagnation point pressure measurement. (Note sharp decay in arc chamber pressure after dump valve opens, with flow break-down soon after.)

Figure 19 shows the results of a pressure rake measurement made with the rake shown in Figure 18 offset in the vertical position to show pressure fall-off due to boundary layer. The boundary layer appears to be somewhat thinner than anticipated and could not be "seen" in measurements such as that shown in Figure 20 taken with the rake centered. Based on very limited data, one would expect the core flow to be about 15 in. in diameter. This means that the boundary layer is considerably thinner than that for similar facilities which have smaller nozzle angles and much longer nozzle lengths. Much more data are required to predict test section uniformity. Among the problems encountered has been the prediction of the way in which the diaphragm opens and its effect on the flow.

Samples were taken of foreign particles in the test section as accumulated on surfaces of several sizes held perpendicular to the stream. These were smaller than could be measured by an ordinary microscope and so were placed under an electron microscope. Most of the particles were found to be considerably less than 1 micron in diameter. It should be noted that the foreign matter in a stream measured by accumulation of particles on a body in the stream may be more a function of the size of particle than of the total quantity of foreign material. If the particles are larger in size, more will be collected, if small in size, less will be collected.

For the low test section densities usually obtained at high Mach numbers, a very sensitive schlieren system is required. This means that a long focal length is desirable, which in turn depends to some extent on the space available. Folding usually becomes necessary, but with each additional optical offset there is a decrease in image quality. A double pass 12 in. system was chosen for its sensitivity and the minimum space requirement on one side of the test section. The parallel design was considered advisable because of the better image quality and the built-in versatility. (The parabolic mirror surface is close to that of a sphere, so that it could be used in a non-parallel arrangement if desired.)

The system was checked for sensitivity by means of a glass wedge of known wedge-angle and a microdensitometer to record the variation in light intensity as

indicated by a given photographic emulsion. Details of the system are discussed in Appendix D. The system has recently been delivered and has not been used, as yet.

The measurement of velocity by photographing the convection of a blast wave downstream has been employed in several hypersonic facilities (see Appendix E). Toward that end, circuits for initiation of a spark disturbance and for a time delayed initiation of a schlieren spark source were built and checked at relatively high pressure statically. Use under tunnel conditions awaits complete check-out of the new, more sensitive schlieren system. The circuits are described in Appendix E.

Early in the present program, it appeared that a direct measurement of free stream density could be made by means of a probe employing a glow discharge. Such a discharge has characteristics which depend on the state of the medium gas in general and the gas density in particular. Several ideas for such a probe were explored with good results but a great deal of further work must be done to perfect a convenient scheme. The exploratory work done is described in Appendix F.

4.0 CONCLUSIONS

It appears that there are many advantages to an inductance type hot-shot facility. Energy can be effectively stored in a coil over a long period of time and quickly transferred to the working fluid by means of arc heating, thus achieving very high stagnation temperatures and pressures. The fluid can then be expanded to very high Mach numbers, with quasi-steady flow extending over a reasonable length of time. There are three main problems associated with the hot shot facility, however. They are: (1) radiation losses at temperatures above $4000^{\circ}K$, (2) foreign substances (from the arc chamber) entering the working fluid, and (3) test section measurements. These problems are to some extent common to any facility operating at very high temperatures.

As the temperature of the working fluid increases, heat transfer by radiation increases exponentially, so that above about 4000°K there is a rapid loss of energy with time with concombitant decay of stagnation conditions. This loss can be somewhat diminished by the use of reflecting wall surfaces—or insulating materials which can withstand the high temperatures. Perhaps a much more promising approach, in view of the present day materials limitations, is programmed energy input. That is, the transfer of energy to the working fluid at the same rate that energy is being lost through radiation to heat-sink walls. The inductance energy storage system may be particularly adaptable to this scheme.

The contamination (foreign substances in the working fluid) is also a problem common to all high temperature facilities. It appears that a really pure working fluid at high temperature is not possible in any facility. The problem becomes how to minimize the contamination, and how to determine the exact composition. This leads to the third problem mentioned—that of test section measurements.

At high temperatures, "real-gas" phenomena such as deviation from thermal equilibrium become important. It becomes too difficult to compute the test section conditions based on stagnation chamber measurements. Measurements must therefore be made in the test section itself to determine the condition of the working fluid. The combination of high velocity (high stagnation temperature) and low density in the test section makes the "usual" measurement of static free stream pressure and determination of density gradients by schlieren photography extremely difficult. The lack of knowledge of composition at extreme conditions complicates the problem further. New techniques for determining the state of the gas must be explored. The perfection of such techniques has proven to be very limited without extensive funds.

REFERENCES

1. Sherman, P. M., Early, H. C., Lawrence, W. N., "Design Considerations for Arc Heated Hypersonic Tunnel," The Univ. of Mich. Report 02953-1-F, 1960; ASTIA AD-240708.
2. Hall, J. G., Russo, A. L., "Studies of Chemical Nonequilibrium in Hypersonic Nozzle Flows," Combustion Institute Western States Section, Los Angeles, Nov. 1959.
3. Sichel, Martin, "The Effect of the Boundary Layer Upon the Flow In a Conical Hypersonic Wind Tunnel Nozzle," The Univ. of Mich. Report 02953-2-F, 1963.
4. Grabau, M., Humphrey, R. L., Little, W. J., "Determination of Test-Section, After-Shock and Stagnation Conditions in Hotshot Tunnels using Real Nitrogen at Temperatures from 3000 to 4000^{O}K," Arnold Engineering Development Center, AEDC TN 61-82, July 1961.
5. Smotherman, W. E., Maddox, W. V., "Variable Reluctance Pressure Transducer Development," Arnold Engineering Development Center, AEDC TDR-63-135, July 1963.
6. Hilsenrath, J., Klein, M., Wooley, H. W., "Tables of Thermodynamic Properties of Air Including Dissociation and Ionization from 1500^{O}K to 15,000^{O}K," Arnold Engineering Development Center, AEDC TR-59-20, Dec. 1959.
7. Smith, C. E., Jr., "Thermodynamic Properties of Nitrogen," Lockheed Missiles and Space Co. Report No. 6-90-62-111, Dec. 1962.
8. Grover, F. W., "Inductance Calculations," VanNostrand Co., 1946.
9. Sunde, E. D., "Earth Conduction Effects in Systems," VanNostrand Co., 1949.
10. Humphrey, R. L., Little, W. J., Seeley, L. A., "Mollier Diagram for Nitrogen," AEDC-TN-60-83.

APPENDIX A

THE ARC-INITIATING FUSE-SWITCH

by

D. D. McBride and P. O. Handy

NOMENCLATURE

A	Cross-sectional area of fuse
a	See Figure A-2
B	Electromagnetic field strength
C_1	Integration constant
C_2	Integration constant
C_3	Integration constant
C_4	Integration constant
C_P	Specific heat
C_{P_f}	Specific heat of fuse
E	Modulus of elasticity
F	Force distribution on fuse
F_L	Force distribution at tip of fuse
F_0	Force distribution at clamp end of fuse
I	Current
I	Moment of inertia
I_2	Current through co-axial buss and fuse
I_{T_S}	Main buss bar final current
I_{T_t}	Main buss bar current as function of time
K	Experimental constant
k	Conversion coefficient
L	See Figure A-2
ℓ	See Figure A-2
M	Moment on fuse
M	Mass
M_f	Mass of fuse
P	Effective load at tip of fuse
R	See Figure A-2
R	Resistance
R_c	Resistance of co-axial buss

R_{f_r}	Resistance of fuse at reference temperature T_r
R_{f_T}	Resistance of fuse as function of temperature
R_s	Resistance of main transfer switch
r	See Figure A-2
T	Temperature
T_A	Temperature of fuse at main switch opening (at time, $t = \tau$)
T_B	Temperature of fuse at breakage (at time, $t = t_B$)
T_0	Initial temperature of fuse
T_r	Reference temperature
t	Time
t_B	Time from main switch opening to fuse breakage
V	Shear force on fuse
x	See Figure A-2
y	Deflection of fuse
δ	Mass density of fuse
Θ	Slope of fuse
θ	See Figure A-2
θ_1	See Figure A-2
θ_2	See Figure A-2
μ	Permeability of free space
ρ	Resistivity of fuse
τ	Current buildup time
ϕ	See Figure A-2

INTRODUCTION

The unit shown as S_3 in Figure 2 is not really what is conventionally considered either a fuse or a switch. It is a copper bar, installed in parallel with the electrodes, which is designed to break in such a manner that the contact points at the break widely separate very rapidly, initiating an arc across the electrodes. The bar must be designed to carry part of the current during the relatively long (approximately 3 second) current buildup in the coil as well as the total current for the short time necessary to allow the main transfer switch S_2 to open completely.

This switching method was designed by first using the arrangement shown in Figure 5. A "V" shaped copper bar (~ 1/4 in. x 1/8 in. x 4 in.) fastened to the bottom ends of the external electrodes, separated and flattened out against the vertical external electrode bars (as can be seen in Figure 5) initiating an arc which travelled up the vertical bars extremely rapidly (as indicated by Fastax photographs). The arc tends to maintain itself with the arc column roots at the top outermost edge of the vertical bars, the arc column stretching into a large arch.

To prevent an arc from being maintained at the main transfer switch S_2, the resistance in the fuse-switch (hereafter called simply the fuse) S_3 part of the circuit should be so small that the voltage across it is smaller than that necessary to maintain an arc at S_2 (about 20 volts) or approximately 100×10^{-6} ohms at 200,000 amperes.

The time between the opening of the main switch S_2 and the breaking of the fuse S_3 is of critical importance. If the fuse breaks pre-maturely, the main switch may not be completely open and an arc may be maintained across the main switch itself while a late opening fuse allows a waste of energy by dissipation through the circuit resistance. A delay time of 25 milliseconds was chosen for optimum performance.

After testing several different fuse designs and materials, an annealed copper fuse of the configuration shown in Figure A-1, was chosen for its simplicity and reliability.

This appendix describes the method of calculating fuse size to give a certain breakage time.

CALCULATION OF THE FORCE ACTING TO BREAK THE FUSE

Figure A-2 shows a schematic of the fuse configuration chosen for the arc chamber. The repulsive force distribution between the two bars in the electromagnetic field generated by the current is given by

$$F = I\int_0^{\ell} B d\ell \qquad \text{(A-1)}$$

where

$$B = \frac{\mu I}{4\pi}\int_0^{a} \frac{\sin\theta\ dx}{r^2} \quad . \qquad \text{(A-2)}$$

(See Krause, John D., Electromagnetics, McGraw Hill, Inc., 1953, pp. 145-167.) (In Equation A-2, μ is the permeability of free space and I is the current through the bars.) Now:

$$dx \sin\theta = r d\theta$$

and

$$r \sin\theta = R + \ell \sin\phi \quad ;$$

therefore,

$$r = \frac{R + \ell \sin\phi}{\sin\theta} \quad .$$

Substituting this into Equation A-2 and noting that as x varies between 0 and a, θ varies between θ_1 and θ_2,

$$B = \frac{\mu I}{4\pi} \int_{\theta_1}^{\theta_2} \frac{\sin \theta d\theta}{R + \ell \sin \phi} \tag{A-3}$$

$$= \frac{\mu I}{4\pi (R + \ell \sin \phi)} [- \cos \theta]_{\theta_1}^{\theta_2} \tag{A-4}$$

It can be seen from Figure A-2 that

$$\cos \theta_2 = - \frac{\ell \cos \phi}{\sqrt{(R + \ell \sin \phi)^2 + (\ell \cos \phi)^2}}$$

$$\cos \theta_1 = \frac{a - \ell \cos \phi}{\sqrt{(a - \ell \cos \phi)^2 + (R + \ell \sin \phi)^2}} .$$

Therefore, from Equations A-1 and A-4:

$$F = \frac{I^2 \mu}{4\pi} \int_0^{\ell} \left[\frac{\ell \cos \phi}{(R + \ell \sin \phi) \sqrt{(R + \ell \sin \phi)^2 + (\ell \cos \phi)^2}} \right. \tag{A-5}$$

$$\left. + \frac{a - \ell \cos \phi}{(R + \ell \sin \phi) \sqrt{(a - \ell \cos \phi)^2 + (R + \ell \sin \phi)^2}} \right] d\ell$$

This equation assumes the fuse to be of curved cross-section (the center of curvature being at the centerline of the center electrode) and of infinitely small thickness.

If the fuse is considered to be a beam, rigidly clamped at one end, the situation can be approximated by a one-dimensional beam problem. Equation A-5 can be numerically integrated to give a force distribution similar to that in Figure A-3. Approximating this distribution by the linear force distribution shown in Figure A-4 simplifies the problem considerably.

The beam equations are as follows:

Load:

$$F = F_0 + \frac{F_L - F_0}{L} x \tag{A-6}$$

Shear:

$$V = \int F \, dx$$

$$= F_0 x + \frac{F_L - F_0}{2L} x^2 + C_1 \tag{A-7}$$

Moment:

$$M = \int V \, dx$$

$$= \frac{F_0}{2} x^2 + \frac{F_L - F_0}{6L} x^3 + C_1 x + C_2 \tag{A-8}$$

Slope:

$$\Theta = \int \frac{M}{EI} dx$$

$$= \frac{1}{EI} \left[\frac{F_0}{6} x^3 + \frac{F_L - F_0}{24 L} x^4 + \frac{C_1}{2} x^2 + C_2 x + C_3 \right] \tag{A-9}$$

Deflection:

$$y = \int \Theta \, dx$$

$$= \frac{1}{EI}\left[\frac{F_0}{24}x^4 + \frac{F_L - F_0}{120\,L}x^5 + \frac{C_1}{6}x^3 + \frac{C_2}{2}x^2 + C_3 x + C_4\right] \qquad \text{(A-10)}$$

The boundary conditions on the beam are given by:

at $x = L$, $V = 0$ $M = 0$ at $x = 0$, $\Theta = 0$ $y = 0$

Applying these boundary conditions, the constants are found:

$$C_1 = -\frac{F_L + F_0}{2}L \qquad C_2 = \frac{2F_L + F_0}{6}L^2$$

$$C_3 = 0 \qquad C_4 = 0$$

Thus Equation A-10 becomes

$$y = \frac{1}{EI}\left[\frac{F_0}{24}x^4 + \frac{F_L - F_0}{120\,L}x^5 - \frac{F_L + F_0}{12}Lx^3 + \frac{2F_L + F_0}{12}L^2x^2\right] \qquad \text{(A-11)}$$

and the deflection at the tip of the beam is

$$y_L = \frac{11F_L + 4F_0}{120\,EI}L^4 \qquad \text{(A-12)}$$

This deflection due to a linear force distribution across the beam can now be equated to the deflection caused by a single load P at the tip of the beam. The load P required to satisfy this equation can then be considered to be the effective force tending to break the fuse at the tip.

For an end loaded cantilever beam, the deflection at the tip is

$$y_L = \frac{PL^3}{3\,EI} \qquad \text{(A-13)}$$

Equating Equations A-12 and A-13 and solving for P:

$$P = \frac{11F_L + 4F_0}{40}L \qquad \text{(A-14)}$$

The numerical constants for the fuse configuration used are:

$L = 3.2$ cm $\qquad R = 1.6$ cm

$a = 4.8$ cm $\qquad \phi = 39^{o}$

and, $\mu = 4\pi \times 10^{-7} \frac{\text{henries}}{\text{meter}}$. Using these values in Equations A-5 and A-14 gives a value for P as a function of current.

$$P = .1548\ I^2 \times 10^{-7} \text{ lbs}$$

where the current I is in amperes.

PREHEATING OF FUSE PRIOR TO MAIN SWITCH OPENING

When an electric current flows through a resistance, heat is produced which raises the temperature of the material according to the relationship

$$k\ I^2\ R\ dt = M\ C_P\ dT \quad . \qquad \text{(A-15)}$$

When I is the current in amperes, R is the resistance in ohms, t is the time in seconds, M is the mass in grams, C_P is the specific heat in calories per gram - ^{o}C, and T is the temperature in ^{o}C, the constant k is equal to 0.2389.

A schematic drawing of the parallel circuit of the arc chamber prior to the opening of the main switch is shown in Figure A-5. From the figure it is seen that

$$I_2 = \frac{I_{T_t} R_s}{R_s + R_c + R_{f_T}} \qquad \text{(A-16)}$$

Equation A-15 when applied to heating of the fuse becomes

$$\frac{.2389}{3} R_s^2 R_{f_r} \tau I_{T_s}^2 = M_f C_{P_f} \left\{ (R_s + R_c)^2 (234.5 + T_r) \ln \frac{234.5 + T_A}{234.5 + T_0} + \right.$$

$$\left[2 (R_s + R_c) R_{f_r} + \frac{234.5 R_{f_r}^2}{234.5 + T_r} \right] (T_A - T_0) +$$

$$\left. \frac{R_{f_r}^2}{234.5 + T_r} \left(\frac{T_A^2}{2} - \frac{T_0^2}{2} \right) \right\} . \qquad \text{(A-21)}$$

Both the mass of the fuse M_f and the reference resistance R_{f_r} are functions of the length L and the cross-sectional area A of the fuse and may be represented as follows:

$$M_f = \delta LA$$

$$R_{f_r} = \rho \frac{L}{A}$$

where δ is the mass density of the fuse material and ρ is the resistivity of the fuse material. Equation A-21 now becomes:

$$.0796 R_s^2 \rho \tau I_{T_s}^2 = \delta A^2 C_{P_f} \left\{ (R_s + R_c)^2 (234.5 + T_r) \ln \frac{234.5 + T_A}{234.5 + T_0} + \right.$$

$$\left[2 (R_s + R_c) \rho \frac{L}{A} + \frac{234.5 \rho^2 L^2}{A^2 (234.5 + T_r)} \right] (T_A - T_0) +$$

$$\left. \frac{\rho^2 L^2}{A^2 (234.5 + T_r)} \left(\frac{T_A^2}{2} - \frac{T_0^2}{2} \right) \right\} . \qquad \text{(A-22)}$$

$$. 2389\, I_2^{\,2}\, R_{f_T}\, dt = M_f\, C_{P_f}\, dT \quad . \tag{A-17}$$

Now, the fuse resistance as a function of temperature is obtained from the following considerations.

The resistance of copper decreases with temperature at a rate which is practically linear and if extrapolated would give a resistance of zero at - 234. 5^{o}C. Therefore, if the resistance of the fuse at temperature T is R_{f_T} and the resistance of the fuse at some reference temperature T_r is R_{f_r}, then

$$R_{f_T} = \frac{234.5 + T}{234.5 + T_r} R_{f_r} \quad . \tag{A-18}$$

Assuming a linear buildup of current with time, the main time dependent bus bar current I_{T_t} can be considered to be a linear ratio of the final desired bus bar current I_{T_s}. Thus, considering τ to be the total time for current buildup,

$$I_{T_t} = \frac{t}{\tau} I_{T_s} \tag{A-19}$$

Combining Equations A-16, A-17, A-18, and A-19 and rearranging gives:

$$. 2389 \left(\frac{I_{T_s}^{\,2}\, R_s^{\,2}\, R_{f_r}}{\tau^2} \right) t^2\, dt = M_f\, C_{P_f} \left[\frac{(R_s + R_c)^2\, (234.5 + T_r)}{(234.5 + T)} + 2(R_s + R_c)\, R_{f_r} + \left(\frac{234.5 + T}{234.5 + T_r} \right) R_{f_r}^{\,2} \right] dT \tag{A-20}$$

Integrating Equation A-20 between the limits $0 \leq t \leq \tau$ and $T_0 \leq T \leq T_A$, where T_0 is the initial temperature of the fuse at t = 0, and T_A is the temperature of the fuse at main switch opening, gives:

For a given current buildup time τ, Equation A-22 contains three variables—I_{T_S}, A, and T_A. A graph such as that shown in Figure A-6 may be drawn from Equation A-22 to show the relationship between these three variables.

FUSE HEATING AFTER THE MAIN SWITCH OPENS

The process for finding the temperature of the fuse at breakage is essentially the same as for finding the temperature at the opening of the main switch with the following exceptions:

1) the current is assumed constant at a value of I_{T_S}
2) there is now no parallel circuit; therefore, I_{T_S} is the current passing through the fuse.

Equation A-20 becomes:

$$.2389\, I_{T_S}^{\,2} R_{f_r}\, dt = M_f\, C_{P_f} \left(\frac{234.5 + T_r}{234.5 + T} \right) dT \qquad \text{(A-23)}$$

and integrating between the limits $T_A \leq T \leq T_B$, where t_B is the time from main switch opening to fuse breakage and T_B is the temperature of the fuse at breakage, gives:

$$.2389\, I_{T_S}^{\,2} R_{f_r}\, t_B = M_f\, C_{P_f}\, (234.5 + T_r) \ln \frac{234.5 + T_B}{234.5 + T_A} \qquad \text{(A-24)}$$

or

$$t_B = \frac{M_f\, C_{P_f}\, (234.5 + T_r)}{.2389\, I_{T_S}^{\,2} R_{f_r}} \ln \frac{234.5 + T_B}{234.5 + T_A} \,. \qquad \text{(A-25)}$$

However, from experimental results it was found that since the total current I_{T_S} was not achieved immediately after the main switch opened, the time to breakage was slightly longer than predicted. To allow for this an experimental constant

K is introduced into Equation A-25 giving:

$$t_B = \frac{K M_f C_{P_f} (234.5 + T_r)}{.2389 I_{T_s}^2 R_{f_r}} \ln \frac{234.5 + T_B}{234.5 + T_A} \quad (A\text{-}26)$$

and in terms of ρ, δ, L, and A:

$$t_B = \frac{K\delta A^2 C_{P_f} (234.5 + T_r)}{.2389 I_{T_s}^2 \rho} \ln \frac{234.5 + T_B}{234.5 + T_A} \quad (A\text{-}27)$$

Equation A-27 contains one new variable, T_B (t_B has already been chosen to give optimum performance). A plot of material tensile strength vs. temperature such as that shown in Figure A-7, amounts to another independent equation in no new variables since it is a plot of P/A^2 vs. T_B and P has already been calculated. Thus there now exist three independent equations in four variables and a graph such as that shown in Figure A-8 can be drawn showing cross-sectional area against run current for a breakage time of 25 milliseconds.

CONSTANTS FOR FUSE SIZE DETERMINATION

The constants associated with the present fuse configuration are as follows:

$R_c = 70 \times 10^{-6}\ \Omega$ $\qquad$ $R_s = 15 \times 10^{-6}\ \Omega$

$\rho = 1.724 \times 10^{-6}\ \Omega$ cm $\qquad$ $\delta = 8.9$ gm/cm^3

L = 3.2 cm $\qquad$ $C_{P_{cu}} = .093$ cal/gm ^oC

$\tau = 1.5$ sec $\qquad$ $t_B = 25$ milliseconds

K = 1.3

After the fuse size has been determined, the fuse should be made slightly oversize and a hole drilled at the desired breaking point to adjust the cross-sectional area and to assure that the fuse will break at that point.

APPENDIX B

ARC-CHAMBER PRESSURE VESSEL DESIGN

by

P-L. M. Lu and D. D. McBride
with the guidance of John Taylor

NOMENCLATURE

σ	Stress
θ	Angle between maximum stress concentration and direction of applied stress
N	Proportionality factor of longitudinal to circumferential pre-stress
K	Stress concentration factor
r	radius
p	pressure
m	(outer radius of shell/inner radius of shell)^2
A, B, C	Inner, middle, and outer shells, respectively
E	Modulus of elasticity
δ	Radial Interference

Subscripts

θ	Circumferential direction
n	Normal direction
i	Inner
o	Outer
r	Radial direction
f	(due to interference fit)
z	Axial direction
design	Design value
s	Shearing
A, B, C	(as above)

INTRODUCTION

The arc chamber shell is designed to contain a high pressure hot gas with a maximum operating pressure of 80,000 psi. The basic design procedure centers upon Lame's solution for a thick-walled cylinder and gives a moderately conservative result (based on beginning of yielding) (Reference B-1).

Potomac "A" (Allegheny Ludlum Corp.), a high chromium-molybdenum content steel, was chosen for the shell due to its high strength. At the optimum condition its yielding strength is approximately 230,000 psi and its ultimate tensile strength is above 280,000 psi.

There are three holes in the walls of the arc chamber—a pressure relief passage or "dump valve", a transducer hole, and a charge gas inlet. Because of the discontinuity of material, the maximum concentration of stress will be located at the edge of these holes. There is no available exact solution for the determination of the stress concentration at a hole in a curved wall. However, there is an exact solution for the stress concentration factor at a hole in an infinite flat plate. Because of the relatively small hole diameter in comparison to the wall curvature, this solution is used in this case.

Since no available material is strong enough to withstand the high stress concentration located at the holes, a pre-stress design method is adopted. The chamber wall is therefore divided into three shells. The inner shell is pre-stressed compressively to balance part of the tensile stress caused by the loading pressure and its thickness is computed to give a minimum stress concentration at the holes. The thickness of the middle and outer shells are computed to give as nearly as possible an even stress distribution through the chamber wall. The three holes are located 120^{O} apart to give a more even stress distribution along the circumference of the chamber wall.

The inside diameter of the inner shell is not uniform, becoming greater at the two ends. Therefore, to assure a relatively uniform compressive pre-stress distribution along the chamber core and to decrease the initial compressive stress

at the threaded sections located at both ends, the contours of the middle and outer shells are tapered toward both ends. As a result the thickest part of the chamber wall is located where the loading pressure directly applies.

The maximum outside diameter of the arc chamber is 22 inches and the overall length—determined by the length of the chamber core, the electrode arrangement, and the length of the two end plugs—is 33 1/4 inches. The arc chamber sketch is shown in Figure

DETERMINATION OF STRESS CONCENTRATION FACTOR OF HOLES

It is stated in the previous section that the analysis of stress concentration at a hole in an infinite flat plate will be adapted for this case. The basic solution for the stress at a hole in an infinite flat plate subject to a uniform applied stress, σ_n, in one direction is

$$\sigma_\theta = \sigma_n (1 - 2 \cos 2\theta)$$

where σ_θ is the circumferential stress at the surface of the hole and at an angle θ with the applied stress (Reference B-2).

If an additional uniform stress, $N\sigma_n$, is applied to the plate perpendicular to the original stress σ_n (see Figure B-1), the resultant circumferential stress at the hole is

$$\begin{aligned} \sigma_\theta &= \sigma_n \left\{ 1 - 2 \cos 2\theta + N \left[1 - 2 \cos (2\theta - \pi) \right] \right\} \\ &= \sigma_n \left\{ 1 + N - (1 - N) \, 2 \cos 2\theta \right\} \end{aligned} \qquad \text{(B-1)}$$

The proportion of longitudinal to circumferential pre-stress in the cylinder is not accurately known but is estimated to be of the order of 1 to 5. This corresponds to an N of 0.2.

It is obvious from Equation B-1 that σ_θ will be maximum at $\theta = \pi/2$. Therefore, θ is assigned this value and

$$\sigma_\theta = \sigma_n \left\{ 1 + .2 - (1 - .2)\, 2 \cos \pi \right\}$$
$$= 2.8\, \sigma_n \qquad \text{(B-2)}$$

This coefficient 2.8 is called the stress concentration factor K. With this factor it is found later that the highest principal stress in the arc chamber is 200,000 psi which is far beyond the proportional limit of the material (about 150,000 psi). Therefore a local yielding will be expected, and a redistribution of stress through local relaxation of the material will occur. The local yielding can be judged by means of the appropriate stress-strain curve. Stress-strain measurements were made on specimens taken from each part of the structure. A typical curve is shown in Figure B-4.

In the design of the arc chamber the stress computation which is based on linear elastic analysis will be on the conservative side because of a redistribution of stress at high stress concentration areas.

The assumption stated in the last paragraph must be explained in detail. The discussion requires reference to the notions of limit design, beyond the ordinary investigation based on linearly elastic behavior. Limit refers to the state at which the system has reached its ultimate capacity. The limit considerations become of significance in general where:

a) the ultimate capacity of a system lies well beyond the state at which stress may locally reach a prescribed maximum value, and
b) one is forced to design in the realm of the physical strength limits of the material (this corresponds to the fact that the chamber cannot be significantly strengthened by an increase in size or change in geometry).

This is the case with the arc chamber.

The excess of an ultimate capacity over that capacity which corresponds to the inception of local yielding, is a function of the system's capability for accomplishing a redistribution of stress through local relaxation in the material. This

capability is in turn measured in terms of the nature of stress distribution at the state of local yield (it is implicit that the material be able to withstand the requisite deformation without rupture).

Inversely to this, the existence of stress concentrations implies that nature of stress distribution for which relaxation may occur. Now, one must note the duplicity of concentration of stress, i. e., that the stress diminishes rapidly from a maximum at the hole's surface (as one proceeds radially outward) and that this maximum exists at only two points on the circumference of the hole. The former is revealed in the elastic solution while the circumferential distribution is expressed by Equation B-2.

The above mentioned duplicity is to be associated with the phenomena of re-distribution of stress both circumferentially and radially. Once again this re-distribution will be accomplished as the material in the region of local concentration suffers progressive inelastic deformation.

It is clear from the above argument that for any material which can endure some degree of inelastic deformation, a design based on linear elastic analysis is bound to be quite conservative.

DETERMINATION OF THE O. D. OF THE CHAMBER

From the general expression of Lame's solution, the radial and circumferential stresses on any surface of radius r are

$$\sigma_r = \frac{r_i^2 p_i - r_o^2 p_o}{r_o^2 - r_i^2} - \frac{(p_i - p_o) r_i^2 r_o^2}{r^2 (r_o^2 - r_i^2)} \qquad \text{(B-3)}$$

$$\sigma_\theta = \frac{r_i^2 p_i - r_o^2 p_o}{r_o^2 - r_i^2} + \frac{(p_i - p_o) r_i^2 r_o^2}{r^2 (r_o^2 - r_i^2)} \qquad \text{(B-4)}$$

The chamber walls are first considered to be composed of two shells, The inner shell is subjected to a compressive stress, due to shrink fit, while the outer shell is subjected to a tensile stress. Let this shrink fit pressure between the contacting surfaces of these two shells be called p_{f_1} (see Figure B-2). From Equations B-3 and B-4, the corresponding initial stresses are found:

$$\sigma_r' = \frac{r_2^2 p_{f_1}^2}{r_2^2 - r_1^2}\left(\frac{r_1^2}{r^2} - 1\right)$$

$$\sigma_\theta' = -\frac{r_2^2 p_{f_1}^2}{r_2^2 - r_1^2}\left(\frac{r_1^2}{r^2} + 1\right)$$

where $r_1 \leq r \leq r_2$;

$$\sigma_r' = \frac{r_2^2 p_{f_1}^2}{r_3^2 - r_2^2}\left(-\frac{r_3^2}{r^2} + 1\right)$$

$$\sigma_\theta' = \frac{r_2^2 p_{f_1}^2}{r_3^2 - r_2^2}\left(\frac{r_3^2}{r^2} + 1\right)$$

where $r_2 \leq r \leq r_3$.

The stresses due to a loading pressure inside the chamber are

$$\sigma_r'' = \frac{r_1^2 p}{r_3^2 - r_1^2}\left(-\frac{r_3^2}{r^2} + 1\right)$$

$$\sigma_\theta'' = \frac{r_1^2 p}{r_3^2 - r_1^2}\left(\frac{r_3^2}{r^2} + 1\right) .$$

The final stresses are found from the superposition of the initial compressive stress due to shrink fit and the tensile stress due to loading pressure:

$$\sigma_r = \sigma_r' + \sigma_r''$$

$$\sigma_\theta = \sigma_\theta' + \sigma_\theta'' \quad .$$

The initial stresses at the surface $r = r_1$ due to shrink fit pressure p_{f_1}, are

$$\sigma_\theta'_{r = r_1} = -\frac{2r_2^2 p_{f_1}}{r_2^2 - r_1^2}$$

$$\sigma_r'_{r = r_1} = 0 \qquad \text{(B-5)}$$

$$\sigma_z' << \sigma_\theta'$$

If we use the stress concentration factor K = 2.8, we can equate

$$\left| 2.8\, \sigma_\theta'_{r = r_1} \right| = \sigma_{design} \quad \text{or} \quad \sigma_\theta'_{r = r_1} = \frac{\sigma_{design}}{2.8} \qquad \text{(B-6)}$$

or

$$\left| \frac{5.6\, r_2^2 p_{f_1}}{r_2^2 - r_1^2} \right| = \sigma_{design} \qquad \text{(B-7)}$$

$$p_{f_1} = \frac{\sigma_{design}}{5.6} \frac{r_2^2 - r_1^2}{r_2^2}$$

At the same location the stress due to loading is

$$\sigma_\theta''_{r = r_1} = p \frac{r_3^2 + r_1^2}{r_3^2 - r_1^2} \qquad \text{(B-8)}$$

The final stress is $\sigma_\theta' + \sigma_\theta''$ or

$$\sigma_{\theta\ r = r_1} = -\frac{\sigma_{design}}{2.8} + p\left(\frac{r_3^2 + r_1^2}{r_3^2 - r_1^2}\right)$$

$$= -\frac{\sigma_{design}}{2.8} + p\left(\frac{m+1}{m-1}\right) \qquad \text{(B-9)}$$

where

$$m = \frac{r_3^2}{r_1^2} \qquad \text{(B-10)}$$

If the stress due to the internal loading alone is considered, the stress concentration factor K is found to be equal to 2.0 from Equation B-2. This is true since the longitudinal or axial stress is then equal to the circumferential or hoop stress and N = 1. This is the minimum possibility of the value of K. The maximum possibility has been previously calculated as 2.8. Therefore, the true value of the stress concentration factor present, when both internal loading and pre-stressing are considered, is estimated to be K = 2.2.

The axial stress σ_z can be obtained approximately:

$$\sigma_z = \frac{pr_1^2}{r_2^2 - r_1^2} \qquad \text{(B-11)}$$

and for $\sigma_z = \sigma_\theta$, from Equation B-9,

$$\frac{pr_1^2}{r_2^2 - r_1^2} = -\frac{\sigma_{design}}{2.8} + p\left(\frac{m+1}{m-1}\right)$$

$$r_2^2 = r_1^2\left[\frac{1}{\left(\frac{m+1}{m-1}\right) - \frac{\sigma_{design}}{2.8\,p}} + 1\right] . \qquad \text{(B-12)}$$

It is clear that the material at $r = r_1$, the inner surface, is subjected to triaxial stresses. The maximum shearing stress is equal to one-half the algebraic difference of the two principle stresses whose algebraic difference is the greatest (Reference B-4). Therefore the maximum shear stress located at the edge of the holes at $r = r_1$ can be expressed as

$$\sigma_{s\ r = r_1} = \frac{1}{2}\,(\text{hoop stress} - \text{radial stress})$$

$$= \frac{1}{2}\left[(2.2\,\sigma_{\theta\ r = r_1} + p) - (-p)\right]$$

$$= \frac{1}{2}\,(2.2\,\sigma_{\theta\ r = r_1} + 2p) \qquad \text{(B-13)}$$

but for steel, $\sigma_s = \frac{1}{2}\,\sigma_n$ or $\sigma_s = \frac{1}{2}\,\sigma_{design}$. Therefore from Equation B-13

$$\sigma_{design} = 2.2\,\sigma_\theta + 2p \qquad \text{(B-14)}$$

From Equation B-11 and B-14, r_2 can be found using the fact that $\sigma_\theta = \sigma_z$:

$$r_2^2 = \frac{\left(0.1 + \frac{\sigma_{design}}{2p}\right) r_1^2}{\frac{\sigma_{design}}{2p} - 1} \qquad \text{(B-15)}$$

By re-arranging Equations B-12 and B-15, the loading pressure p can be found:

$$p = \frac{\sigma_{design}}{1.12}\left[\frac{1}{1 + 1.1\left(\frac{m+1}{m-1}\right)}\right] \qquad \text{(B-16)}$$

From Equation B-16 it can be seen that for the limiting case of infinite wall thickness ($m \to \infty$; $\frac{m+1}{m-1} \to 1$), the minimum design stress is 188,000 psi for an operating pressure of 80,000 psi.

If σ_{design} is taken as 200,000 psi, from Equation B-16,

$p = 80,600$ psi for $m = 20$

$p = 81,600$ psi for $m = 25$

$p = 82,400$ psi for $m = 36$

It is seen that the capacity of the chamber is less affected as m increases. A value of m = 25 gives sufficient thickness to split the outer shell in two shells for more even distribution of stresses (this will be explained in more detail below). The basic dimensions of the chamber shells are found to be as follows:

I. D. of inner shell = 4.37 inches

O. D. of inner shell = 10.62 inches

O. D. of outer shell = 22.00 inches

TWO SHELLS VERSUS THREE SHELLS

From Equation B-7 the shrink fit pressure p can be found to be equal to 29,700 psi. The initial circumferential stress on the outer shell can now be found from Equation B-8:

$$\sigma_{\theta}\Big|_{r = 5.31} = \frac{29,700\,(11^2 + 5.31^2)}{11^2 - 5.31^2}$$

$$= 47,800 \text{ psi}$$

The circumferential stress due to the loading pressure, 80,000 psi, is

$$\sigma_{\theta}\Big|_{r = 5.31} = \frac{2.187^2 \times 80,000}{11^2 - 2.187^2}\left(1 + \frac{11^2}{5.31^2}\right)$$

$$= 17,780 \text{ psi} .$$

The final maximum circumferential stress at the hole will be

$$\sigma_{\theta}\Big|_{r = 5.31} = (17,780 + 47,800)\, 2.8$$

$$= 184,000 \text{ psi} .$$

The initial radial stress at r = 5.31 is equal to the shrink fit pressure 29,700 psi. The radial stress due to the loading pressure is

$$\sigma_{r}\Big|_{r = 5.31} = \frac{2.187^2 \times 80,000}{11^2 - 2.187^2}\left(1 - \frac{11^2}{5.31^2}\right)$$

$$= 11,000 \text{ psi} .$$

Then the final radial stress is equal to 11,000 + 29,700 or 40,700 psi. Therefore, the maximum shearing stress is

$$\sigma_{s_{max}} = \frac{184,000 + 40,700}{2} = 112,350 \text{ psi} .$$

This is higher than one half of the design stress, 200,000 psi. Therefore, the outer shell should be split into two shells, each with less shrink fit pressure yet giving the same compressive stress to the innermost shell surface. As a result, the stresses are distributed more evenly throughout.

DETERMINATION OF THE SIZES OF THE THREE SHELLS

The thickness of the innermost shell has already been calculated. The central shell is assumed to be 2 1/2 inches thick, and the outer shell is assumed to be 3.19 inches thick. With these thicknesses, the radii of the three shells are

$$r_1 = 2.187''$$
$$r_2 = 5.31''$$
$$r_3 = 7.81''$$
$$r_4 = 11''$$

Let the inner, central, and outer shell be "A", "B", and "C" shells respectively as shown in Figure B-3. Again by using Lame's solution for thick wall cylinders, the initial stresses on the different shells can be expressed in terms of the corresponding shrink-fit pressures on each shell.

The initial circumferential stresses on A and B cylinders due to the shrink fit pressure p_{f_1} are:

$$\sigma_\theta'_{A\ r = r_1} = \frac{-2\ p_{f_1} \times 5.31^2}{5.31^2 - 2.187^2} \tag{B-16}$$

$$= -2.4\ p_{f_1}$$

$$\sigma_\theta'_{A\ r = r_2} = \frac{-p_{f_1}\ (5.31^2 + 2.187^2)}{5.31^2 - 2.187^2} \tag{B-17}$$

$$= 1.408\ p_{f_1}$$

$$\sigma_\theta'_{B\ r = r_2} = \frac{p_{f_1}\ (5.31^2 + 7.81^2)}{7.81^2 - 5.31^2} \tag{B-18}$$

$$= 2.72\ p_{f_1}$$

$$\sigma_{\theta}{}'_{B\ r = r_3} = \frac{2 \times 5.31^2 \times p_{f_1}}{7.81^2 - 5.31^2} \tag{B-19}$$

$$= 1.72\ p_{f_1}$$

After the assembly of A and B shells, the circumferential stresses on the one unit shell A + B, and shell C due to the shrink-fit pressure p_{f_2} are:

$$\sigma_{\theta}{}'_{A+B\ r = r_1} = \frac{-2 \times 7.81^2\ p_{f_2}}{7.81^2 - 2.187^2} \tag{B-20}$$

$$= -2.17\ p_{f_2}$$

$$\sigma_{\theta}{}'_{A+B\ r = r_2} = \frac{-p_{f_2} \times 7.81^2}{7.81^2 - 2.187^2}\left(1 + \frac{2.187^2}{5.31^2}\right) \tag{B-21}$$

$$= -1.27\ p_{f_2}$$

$$\sigma_{\theta}{}'_{A+B\ r = r_3} = \frac{-p_{f_2} \times (7.81^2 + 2.187^2)}{7.81^2 - 2.187^2} \tag{B-22}$$

$$= -1.17\ p_{f_2}$$

$$\sigma_{\theta}{}'_{C\ r = r_3} = \frac{p_{f_2}\ (7.81^2 + 11^2)}{11^2 - 7.81^2} \tag{B-23}$$

$$= 3.04\ p_{f_2}$$

$$\sigma_{\theta}'_{C\ r = r_4} = \frac{2\ p_{f_2} \times 7.81^2}{11^2 - 7.81^2} \tag{B-24}$$

$$= 2.033\ p_{f_2}$$

The initial radial stresses on the different surfaces of each shell are:

$$\sigma_r'_{r = r_1} = 0 \tag{B-25}$$

$$\sigma_r'_{r = r_2} = -\left[p_{f_1} + \frac{p_{f_2} \times 7.81^2}{7.81^2 - 2.187^2}\left(1 - \frac{2.187^2}{5.31^2}\right)\right] \tag{B-26}$$

$$= -\left[p_{f_1} + .9\ p_{f_2}\right]$$

$$\sigma_r'_{r = r_3} = p_{f_2} \tag{B-27}$$

$$\sigma_r'_{r = r_4} = 0 \tag{B-28}$$

The circumferential stresses due to the loading pressure, 80,000 psi, on A, B, and C shells are:

$$\sigma_{\theta}''_{r = r_1} = \frac{80{,}000\ (11^2 + 2.187^2)}{11^2 - 2.187^2} \tag{B-29}$$

$$= 86{,}400 \text{ psi}$$

$$\sigma_{\theta}''_{r = r_2} = \frac{80{,}000 \times 2.187^2}{11^2 - 2.187^2}\left(1 + \frac{11^2}{5.31^2}\right) \tag{B-30}$$

$$= 17{,}420 \text{ psi}$$

$$\sigma_\theta''_{r = r_3} = \frac{80,000 \text{ x } 2.187^2}{11^2 - 2.187^2}\left(1 + \frac{11^2}{7.81^2}\right) \tag{B-31}$$

$$= 9850 \text{ psi}$$

$$\sigma_\theta''_{r = r_4} = \frac{80,000 \text{ x } 2 \text{ x } 2.187^2}{11^2 - 2.187^2} \tag{B-32}$$

$$= 6600 \text{ psi}$$

The radial stresses on each shell due to the loading pressure are

$$\sigma_r''_{r = r_1} = 80,000 \text{ psi} \tag{B-33}$$

$$\sigma_r''_{r = r_2} = \frac{80,000 \text{ x } 2.187^2}{11^2 - 2.187^2}\left(1 - \frac{11^2}{5.31^2}\right) \tag{B-34}$$

$$= 10,900 \text{ psi}$$

$$\sigma_r''_{r = r_3} = \frac{80,000 \text{ x } 2.187^2}{11^2 - 2.187^2}\left(1 - \frac{11^2}{7.81^2}\right) \tag{B-35}$$

$$= 3240 \text{ psi}$$

$$\sigma_r''_{r = r_4} = 0 \tag{B-36}$$

Equating the sum of all the initial stresses on shell A at $r = r_1$ to the design stress gives:

$$2.8\,(-2.4\,p_{f_1} - 2.17\,p_{f_2}) = -200,000 \text{ psi} \tag{B-37}$$

Let the sum of the final stresses on B shell at $r = r_2$ be equal to 150,000 psi so that if there is any pressure force from the blasting cap in the dump valve plug transmitted to the wall, the resultant stress is still below the design stress.

$$150,000 = K \times \text{circumferential stress} + \text{radial stress}$$
$$= 2.8\,(2.72\,p_{f_1} - 1.27\,p_{f_2} + 17,420) + (10,900 + p_{f_1} + .9\,p_{f_2}) \tag{B-38}$$

p_{f_1} and p_{f_2} can now be obtained from the simultaneous solution of Equations B-37 and B-38:

$$p_{f_1} = 15,380 \text{ psi} \tag{B-39}$$

$$p_{f_2} = 15,950 \text{ psi} \tag{B-40}$$

The initial circumferential stresses at the different surfaces are now found by the use of Equations B-16 through B-24.

$$\sigma_{\theta\,A\,r=r_1} = -2.4p_{f_1} - 2.17\,p_{f_2} = -71,500 \text{ psi}$$

$$\sigma_{\theta\,A\,r=r_2} = -1.408p_{f_1} - 1.27\,p_{f_2} = -41,800 \text{ psi}$$

$$\sigma_{\theta\,B\,r=r_2} = 2.72\,p_{f_1} - 1.27\,p_{f_2} = 21,600 \text{ psi}$$

$$\sigma_{\theta\,B\,r=r_3} = 1.72\,p_{f_1} - 1.17\,p_{f_2} = 6800 \text{ psi}$$

$$\sigma_{\theta\,C\,r=r_3} = 3.04\,p_{f_2} = 48,400 \text{ psi}$$

$$\sigma_{\theta\,C\,r=r_4} = 2.03\,p_{f_2} = 32,300 \text{ psi}$$

Then the final total maximum shearing stresses (with the appropriate stress concentration factor multiplied in) at the different surfaces are:

$$\sigma_{s_{A\ r = r_1}} = [(-71,500 + 86,400)\ 2.2 + 2 \times 80,000]\ \frac{1}{2} = 96,500 \text{ psi}$$

$$\sigma_{s_{A\ r = r_2}} = [(-41,800 + 17,420)\ 2.2 + 10,900 + 15,380 + 14,400]\ \frac{1}{2} = -6410 \text{ psi}$$

$$\sigma_{s_{B\ r = r_2}} = [(21,600 + 17,420)\ 2.8 + 10,900 + 15,380 + 14,400]\ \frac{1}{2} = 75,000 \text{ psi}$$

$$\sigma_{s_{B\ r = r_3}} = [(6800 + 9850)\ 2.8 + 3240 + 15,900]\ \frac{1}{2} = 32,800 \text{ psi}$$

$$\sigma_{s_{C\ r = r_3}} = [(48,400 + 9850)\ 2.8 + 3240 + 15,900]\ \frac{1}{2} = 91,120 \text{ psi}$$

$$\sigma_{s_{C\ r = r_4}} = [(32,300 + 6600)\ 2.8]\ \frac{1}{2} = 54,500 \text{ psi}$$

The initial stress as well as the total stress distribution along the radius of the chamber is shown schematically in Figure B-5.

Determination of Built-in Shell Interferences

With the shrink fit pressures known, it is now possible to find the interference between each pair of shells (Reference B-3). The elastic modulus E of Potomac "A" varies from 30.35×10^6 to 29×10^6 psi. Taking E as 30×10^6, the radial interference between A and B shells is

$$\delta_{A,B} = \frac{2 \times 15,380 \times 5.31^3\ (7.81^2 - 2.187^2)}{30 \times 10^6\ (5.31^2 - 2.187^2)\ (7.81^2 - 5.31^2)}$$

$$= .01125"$$

The radial interference between "A" + "B" and "C" shells is

$$\delta_{A+B,\ C} = \frac{2 \times 15,950 \times 7.81^3 \left(11^2 - 2.187^2\right)}{30 \times 10^6 \left(7.81^2 - 2.187^2\right)\left(11^2 - 7.81^2\right)}$$

$$= .01745''$$

Cylindrical End Closure

The three shell cylindrical section is closed at the two ends by means of a threaded nut at each end as shown in the sketch of the arc chamber arrangement. Since the upstream closure nut forms part of the outer electrode circuit a beryllium-copper alloy (Brush-Beryllium Co. B-25, with ~ 25% of the conductivity of copper) was chosen for its combination of strength and conductivity. Potomac "A" was employed for the downstream nut.

Buttress threads are used on both nuts for the high load in one direction and its smaller tendancy to gall. In choosing the diameter of 6" both the initial stress due to shrink fit as well as working area in the chamber were considered. A large pitch of .4" per thread was chosen for easy assembly.

REFERENCES

B-1. J. Marin and F. P. J. Rimrott, Plastic Design of Thick Walled Pressure Vessels.

B-2. Timoshenko and Goodier, Theory of Elasticity.

B-3. Timoshenko, Strength of Material, Part II.

B-4. Roark, Formulas for Stress and Strain.

APPENDIX C

HEAT TRANSFER TO ARC-CHAMBER SURFACES

by

Roger Dunlap

VARIATION OF EQUILIBRIUM GAS PROPERTIES DURING BLOWDOWN—EFFECTS OF ENERGY LOSS BY RADIATION

Consider a chamber of volume V and area A_c from which a gas exhausts through a throat of area A_t. Assume the region in which the gases have any appreciable velocity has negligible volume compared to the chamber volume. Then, if properties are uniform throughout the volume, the energy and continuity equations are:

$$-Q_r = \frac{\partial}{\partial t}(\rho_c e_c V) + \rho_t u_t A_t \left(h_t + \frac{u_t^2}{2}\right) \tag{C-1}$$

$$\frac{\partial(\rho_c V)}{\partial t} = -\rho_t A_t u_t \tag{C-2}$$

where

ρ = density

h = enthalpy

e = internal energy

u = velocity

Q_r = net heat transfer rate to wall

subscript t = throat conditions

subscript c = chamber conditions

Assuming the nozzle is short compared to the chamber dimensions there will be negligible radiation in the nozzle and, in addition, the flow between the chamber and nozzle can be considered quaisi-steady. Furthermore, if the gas is in equilibrium, the flow in the nozzle can be considered isentropic and we have

$$h_c(t) = h_t(t) + \frac{u_{t(t)}^2}{2} \tag{C-3}$$

$$S_c(t) = S_t(t) \tag{C-4}$$

$$u_t(t) = a_t(t) \tag{C-5}$$

where S is the entropy and a is the speed of sound.

The expression for the net radiative heat transfer, Q_r, simplifies for the case of a gas at high density and temperature radiating to a black walled container of area A_c at low temperature (relative to the gas temperature) to the Stefan-Boltzman law*

$$Q_r = \sigma T_c^4(t)\, A_c \tag{C-6}$$

Since the density in the arc chamber will usually be high when the gas temperature is high and the wall temperature will be much less than the gas temperature when the radiation is important, Equation (C-6) is a good representation of the actual radiative heat transfer to a perfectly absorbing wall (conservative for wall heating).

Equations (C-1)-(C-6) may be re-arranged to give the governing equations

$$\frac{d\rho'_c}{dt} = -\rho'_t a'_t \tag{C-7}$$

$$\frac{dS'_c}{dt} = \frac{T_c'^3}{\rho_c'} \frac{\tau_t}{\tau_c} \tag{C-8}$$

$$h_c'(\tau) = h_t'(\tau) + \frac{\gamma_o}{2} a_t'^2(\tau) \tag{C-9}$$

---

*The Stephan-Boltzman law implies the Plank energy spectrum which is continuous in frequency. A gas at low pressure clearly radiates a line spectrum, the radiation being solely due to electron transitions within "independent" atoms. As the density increases, the line spectrum begins to broaden as a result of interaction between atoms and molecules which give rise to radiation in addition to that caused by the electron transitions. At high densities the gas begins to act more like a solid in which the molecules are very closely spaced and for which a continuous spectrum of frequencies are radiated.

$$S_c'(\tau) = S_t'(\tau) \tag{C-10}$$

where

$$\rho' = \rho/\rho_o \quad , \qquad \tau_t = \frac{V}{A_t a_o}$$

$$a' = a/a_o \quad , \qquad \tau_c = \frac{VP_o}{A_c T_o^4}$$

$$S' = S/R \quad ,$$

$$T' = T/T_o \quad , \qquad \tau = \frac{t}{\tau_t}$$

$$h' = h/RT_o \quad ,$$

and subscript o refers to convenient low temperature reference conditions where $P_o = \rho_o RT_o$ and $a_o^2 = \gamma_o RT_o$.

Equations (C-7)-(C-10) together with the thermal and calorie equations of state (tables and graphs in the general case) determine the solution for temperature, pressure, density, etc., in the arc chamber. Only in the case of a perfect gas with no radiation ($\tau_c \to \infty$, S_c = constant) can the equations be integrated analytically. For this special case we get the well-known results

$$\frac{\rho_c(t)}{\rho_c(o)} = \left\{ 1 + \left(\frac{\gamma - 1}{2}\right)\left(\frac{\gamma + 1}{2}\right)^{\frac{-\gamma + 1}{2(\gamma - 1)}} \frac{t}{V/A_t a_c(o)} \right\}^{\frac{2}{1 - \gamma}} \tag{C-11}$$

$$\frac{P_c(t)}{P_c(o)} = \left\{ \frac{\rho_c(t)}{\rho_c(o)} \right\}^{\gamma} \tag{C-12}$$

$$\frac{T_c(t)}{T_c(o)} = \left\{ \frac{\rho_c(t)}{\rho_c(o)} \right\}^{\gamma - 1} \tag{C-13}$$

The time variation of air properties for typical initial conditions where radiation can be neglected ($T_c(0) = 4000^{\circ}K$, $P_c(o) = 20,000$ psia, $V = 60$ in.^{3}, $A_t = 0.196$ in.^{2}—dump port) are presented in Figures C-1 to C-3. The equilibrium solution, based on a numerical integration of Equations (C-7)-(C-10) in conjunction with the Mollier Diagram[C-1] for air and the NBS air tables,[C-2] is compared to the perfect gas solutions (Equations (C-11)-(C-13) for $\gamma = 1.2$ and $\gamma = 1.4$. The equilibrium variation of temperature, pressure, and density is bounded by the perfect gas $\gamma = 1.2$ and $\gamma = 1.4$ variations. The time required to empty all of the gas through the dump port is about 100 milliseconds under these conditions.

It may be remarked that the blowdown time, t_{max}, ($t = t_{max}$ when $P \simeq$ one atmosphere) is fairly insensitive to γ and therefore may be estimated by the inversion of Equations (C-11) and (C-12):

$$\frac{t_{max}}{V/A_t\sqrt{RT_c(o)}} = \frac{1}{\gamma^{1/2}}\left(\frac{2}{\gamma - 1}\right)\left(\frac{2}{\gamma + 1}\right)^{\frac{-\gamma + 1}{2(\gamma - 1)}}\left[\left(\frac{P_c(o)}{P_{atm}}\right)^{\frac{\gamma - 1}{2\gamma}} - 1\right] \qquad \text{(C-14)}$$

Equation (C-14) is plotted in Figure C-4. The blowdown time is seen to decrease inversely with the square root of the initial temperature and increase nearly linearly with the logarithm of the initial pressure (in atmospheres).

To investigate the effect of radiation, Equations (C-7)-(C-10) were integrated numerically for an initial temperature of $10,000^{\circ}K$ and an initial density of 8 lbs/ft^3, where the air was now assumed to exit through the tunnel throat ($A_t = .008$ in.^{2}). The chamber volume was 60 in.^{3} and the chamber inside area was 116 in.^{2}. Solutions for the pressure, density, and temperature variations are presented in Figures C-5 to C-7. The equilibrium solutions are again bounded by the perfect gas solutions for $\gamma = 1.2$ and $\gamma = 1.4$. Both solutions required a numerical integration. The equilibrium solution was effected by assuming a gas with constant C_p and C_v and a constant compressibility factor over a small change in gas

properties. The specific heat and compressibility were changed in accordance with the equilibrium values at the beginning of each new step in the numerical integration.

The effect of radiative energy loss on the variation of the gas properties is presented in Figure C-8 where the temperature and pressure variations with radiation are compared to those which would have been obtained by neglecting the radiation (perfect gas, $\gamma = 1.2$ in both cases). It is apparent that the radiation has an appreciable effect on the variation of arc chamber temperature with time, as expected.

HEAT TRANSFER TO THE ARC CHAMBER LINER

The following analysis is concerned with estimating the heating of the arc chamber liner due to conduction and radiation. The gas was considered to have negligible velocity along the walls of the container and therefore convection was not considered.

Conduction Problem

The model used to estimate the order of magnitude of the liner heating due to conduction is indicated below. The gas is assumed to act

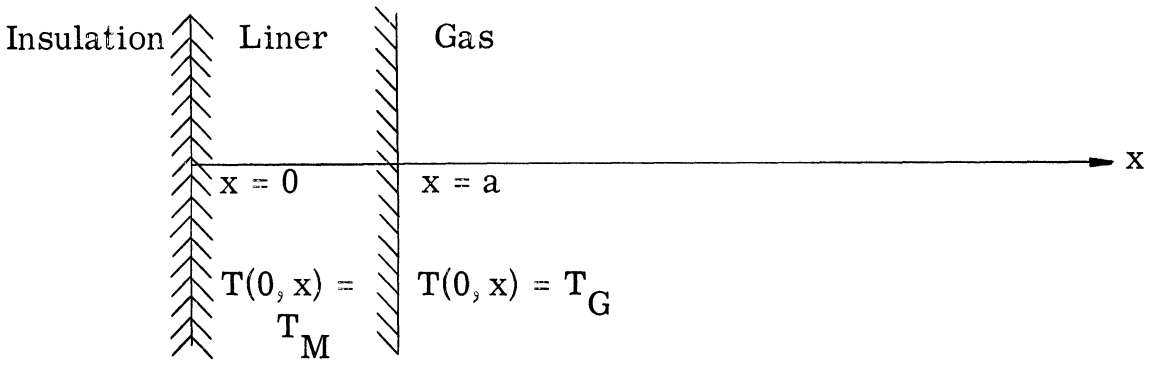

like an infinitely long solid with the proper density and thermal conductivity. No induced gas motion is accounted for and the gas temperature is not allowed to drop due to the tunnel blowing down. Initially the gas is at a high temperature and the liner at low temperature. The problem is to determine the interface

temperature, $T(a, t)$ for $t > o$. The mathematical formulation of the problem is as follows:

$$\frac{\partial T}{\partial t} = K_m \frac{\partial^2 T}{\partial x^2}, \qquad (o < x < a,\ t > o) \tag{C-15}$$

$$\frac{\partial T}{\partial t} = K_G \frac{\partial^2 T}{\partial x^2}, \qquad (x > a,\ t > o) \tag{C-16}$$

$$T(x,o) = T_m, \qquad (x < a)$$

$$T(x, o) = T_G, \qquad (x > a)$$

$$\frac{\partial T}{\partial x}(o, t) = o; \lim_{x \to \infty} T(x, t) = T_G, \qquad (t > o) \tag{C-17}$$

$$T(a-o, t) = T(a+o, t), \qquad (t \geq o)$$

$$k_m \frac{\partial T}{\partial x}(a-o, t) = k_G \frac{\partial T}{\partial x}(a+o, t), \qquad (t > o)$$

where

$$K = \frac{k}{\rho c} = \text{thermal diffusity}$$

k = thermal conductivity

ρ = density

c = specific heat

subscript m pertains to liner

subscript G pertains to gas

The solution for the interface temperature $T(a, t)$ is found by use of the Laplace Transform to be

$$\frac{T(a, t)}{T_G} = \frac{1+\lambda}{2}\left(\frac{T_c}{T_G} - 1\right)\left\{1 + \left[1 - \frac{1}{\lambda}\right]\sum_{n=1}^{\infty} \lambda^n \operatorname{erfc}\left(\frac{na}{\sqrt{K_m t}}\right)\right\} + 1 \tag{C-18}$$

where

$$\lambda = \frac{1 - \frac{k_G}{k_m}\sqrt{\frac{K_m}{K_G}}}{1 + \frac{k_G}{k_m}\sqrt{\frac{K_m}{K_G}}}$$

A typical temperature rise predicted by Equation (C-18) for the gas and copper materials indicated below was $T(\frac{1}{2}$ in., 1 sec) = 570^{o}K.

Copper (Berylco 50 alloy)	Gas (Air)
$T_m = 280^{o}K$	$T_G = 10,000^{o}K$
$\rho_m = 8.75$ gm/cm^3	$\rho_G = 8.0$ lbs/ft^3
$C_m = 0.1 \frac{cal}{gm\text{-}^{o}C}$	$C_{V_G} = 0.75 \frac{cal}{gm\text{-}^{o}C}$
$k_m = 0.55 \frac{cal}{cm\text{-}sec\text{-}^{o}C}$	$k_G = 4.47 \times 10^{-3} \frac{cal}{cm\text{-}sec\text{-}^{o}C}$

The model used here is quite conservative (except for neglect of free and forced convection) and shows that the order of magnitude of the temperature rise due solely to conduction is a few hundred degrees. The solution to the radiation problem below shows that the wall temperature rise due to radiation is of the order of fifteen hundred degrees Kelvin.

Radiation Problem

The cylindrical model used to determine the liner heating due to radiation is indicated below. Radiation from the gas was assumed to be completely absorbed by the wall and wall re-radiation was neglected (a good approximation for a gas at high density, and high temperature relative to the wall temperature).

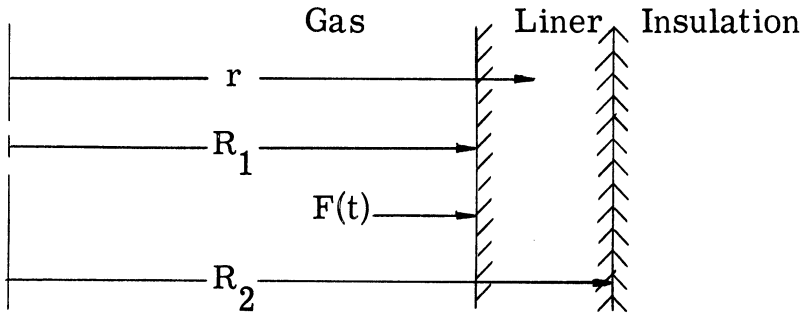

For a liner insulated at the outer boundary with an arbitrary heat transfer rate, F(t), at the inner boundary, the boundary value problem can be written:

$$\frac{\partial T}{\partial t} = K\left(\frac{\partial^2 T}{\partial r^2} + \frac{1}{r}\frac{\partial T}{\partial r}\right) \tag{C-19}$$

$$\left.\begin{aligned} &\frac{\partial T}{\partial r}(R_1,\ t) = -\frac{F(t)}{k},\ t > o \\ &\frac{\partial T}{\partial r}(R_2,\ t) = o,\ t > o \\ &T(r,\ o) = T_o,\ R_1 \leq r \leq R_2 \end{aligned}\right\} \tag{C-20}$$

The solution to this problem can be found, after considerable manipulation, by using Laplace Transform techniques(C-3) to find the solution for the case when F(t) = k and then applying the Duhamel formula(C-4) for the general case. The solution is

$$T(r,t) - T_o = -\frac{K\pi}{kR_1}\int_o^t d\tau\, F(t-\tau)\sum_{n=1}^{\infty} A_n x_n e^{-\frac{Kx_n^2\tau}{R_1^2}} \tag{C-21}$$

where

$$A_n = \frac{J_1(x_n)\, N_o\left(x_n \frac{r}{R_1}\right) - N_1(x_n)\, J_o\left(x_n \frac{r}{R_1}\right)}{1 - \frac{J_1^2(x_r)}{J_1^2\left(\frac{R_2}{R_1} x_n\right)}} \tag{C-22}$$

and the x_n's are the positive roots of the characteristic equation

$$J_1(x)\, N_1\left(\frac{R_2}{R_1} x\right) - J_1\left(\frac{R_2}{R_1} x\right) N_1(x) = o \tag{C-23}$$

$J_n(x)$ is Bessels function of n^{th} order and $N_n(x)$ is the Neumann function of n^{th} order( ).

It is of interest to simplify this solution for the range of interest in the case of the arc chamber, vis., small times. Consider the temperature at the inside wall, $T(R_1, t)$. The temperature solution becomes

$$T(R_1, t) - T_o = \frac{2K}{kR_1} \int_o^t d\tau\, F(t - \tau) \sum_{n=1}^{\infty} \frac{e^{-\frac{Kx_n^2 \tau}{R_1^2}}}{\left[\frac{J_1^2(x_n)}{J_1^2\left(\frac{R_2}{R_1} x_n\right)} - 1\right]} \tag{C-24}$$

The convergence of the series in Equation (C-24) is very slow for small values of $K\tau/R_1^2$ so that many terms are required to get an accurate answer. It behooves one, therefore, to investigate the asympotic values of x_n and the function of J_1 in the brackets. For large n,

$$x_n = \frac{n\pi}{\frac{R_2}{R_1} - 1}, \qquad n \to \infty \tag{C-25}$$

$$\frac{J_1^2(x_n)}{J_1^2\left(\frac{R_2}{R_1} x_n\right)} - 1 = \frac{R_2}{R_1} - 1, \qquad n \to \infty$$

An example of how rapidly these asympotic values are approached is shown below for $R_2/R_1 = 6.5$. It is apparent that the convergence to the asympotic expressions is quite rapid. As long as a large number of terms are required to evaluate the series (small time) it becomes accurate to write the temperature in terms of the expansions listed below for large n. Thus,

$$T(R_1, t) - T_o \simeq \frac{2K}{k(R_2 - R_1)} \int_o^t d\tau\, F(t - \tau) \sum_{n=1}^{\infty} \exp\left[-\frac{K\pi^2 \tau n^2}{(R_2 - R_1)^2}\right] \tag{C-26}$$

n	Xn		$\left[\frac{J_1^2(x_n)}{J_1^2(6.5\,x_n)} - 1\right]^{-1}$	
	Exact	Asympotic	Exact	Asympotic
1	.6275	.571	.115	.182
2	1.177	1.142	.136	.182
3	1.743	1.713	.163	.182
4	2.305	2.285	.170	.182
5	2.8750	2.855	.1725	.182

Furthermore, the sum of the above series, S, is given by the inequality,

$$I < S < 1 + I \qquad \text{C-27)}$$

where

$$I = \int_0^x \exp\left[-\frac{K\pi^2\tau x^2}{(R_2 - R_1)^2}\right] dx = \frac{(R_2 - R_1)}{2\sqrt{K\pi\tau}} \qquad \text{(C-28)}$$

For small time $I >> 1$ and $S \simeq I$ so that the temperature formula (C-26) becomes

$$T(R_1, t) - T_o \simeq \frac{1}{k}\sqrt{\frac{K}{\pi}} \int_0^t \frac{F(t - \tau)}{\sqrt{\tau}}\, d\tau \qquad \text{(C-29)}$$

This is identical to the exact solution to the radiation problem for an infinite one-dimensional slab. The situation in which a cylinder "looks like" a slab is clearly when the radius of the cylinder is large compared to its thickness. Also, a finite slab behaves like an infinite slab for small times since the heat received at one face does not penetrate very deeply. For small times then the above limiting solution, Equation (C-29), is to be expected. The requirement for this limiting solution to be accurate, in view of the two approximations

made, is

$$t << \frac{(R_2 - R_1)^2}{K\pi^2} \tag{C-30}$$

For the parameters of interest the one-dimensional semi-infinite slab solution, Equation (C-29), is a very accurate approximation for the cylinder solution. For $x > o$ the slab solution is given by the equation

$$T(x, t) - T_o = \frac{1}{k}\sqrt{\frac{K}{\pi}} \int_o^t \frac{F(t - \tau)}{\sqrt{\tau}} e^{-\frac{x^2}{4K\tau}} d\tau \tag{C-31}$$

A graph of the copper liner temperature variation (Equations (C-29) and (C-31)) at the inside and outside walls and at an interior point, as a result of radiation heating from a gas initially at $10,000^{o}K$ and 8 lbs/ft^3, is given in Figure C-9. As pointed out previously the radiative heat transfer rate was assumed to be $F(t) = \sigma T_{gas}^4(t)$. The gas temperature distribution was taken from Figure C-5. It can be seen that the liner wall temperature goes through a maximum of about $1500^{o}K$ very rapidly and then decays. This "heat pulse" from the gas (the radiation decreases very rapidly due to the rapid decay of gas temperature, Figure C-5) "travels" through the liner, decaying in amplitude and broadening in width. There is very little temperature rise at the outer wall and the liner is effective in absorbing the heating and protecting the arc chamber. Since the melting point of pure copper is $1356^{o}K$, there may be a small amount of copper lost from the inside walls of the liner.

In view of the large amount of energy lost by radiation (see Figure C-8, for example) it becomes important to consider the dynamics of the energy input from the arc and therein account for radiative energy losses. It may very possibly be that maximum gas temperatures of $10,000^{o}K$ cannot be predicted when radiation is accounted for.

HEAT TRANSFER TO DUMP PORT INSERT

The following analysis is concerned with estimating the heating of the dump port insert due to forced convection while gas is escaping through it. The insert was considered to be a hollow cylinder of length as shown below.

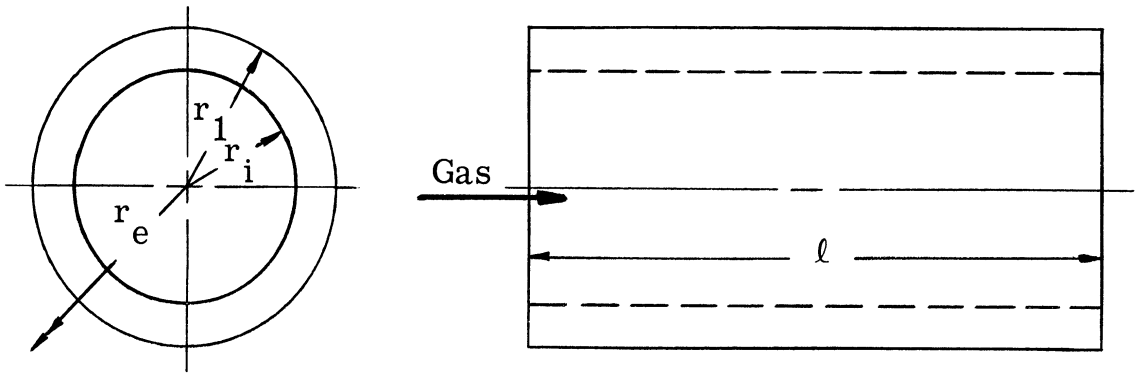

This insert is imbedded in the thick steel walls of the arc chamber and is effectively insulated at some distant radius, r_e*.

The heat transfer to the inside wall of the insert is taken to be the average heat transfer over a flat plate of length ℓ and is given by the expression (C-6)

$$\bar{q}_w = E\,[T_G(t) - T_w(t)] \tag{C-32}$$

where

$$E = \frac{0.664\,(k_G)_w}{\ell}\,P_{r_w}^{1/3}\sqrt{\frac{u_G \ell}{(\gamma_G)_w}} \tag{C-33}$$

and E = heat transfer coefficient

$\bar{q}_w$ = average heat transfer rate over the length ℓ

T_G = gas temperature in the mainstream

*As it turns out, the times involved are so short that there is no appreciable temperature rise at r_1 and therefore the insert can be considered to be insulated very close to $r = r_1$.

T_w = wall temperature

k_G = thermal conductivity of the gas

P_r = Prandtl Number

U_G = gas velocity in the mainstream

γ_G = kinematic viscosity of the gas

subscript w pertains to conditions at the wall

In the solution of the conduction problem to determine the insert temperature, the heat transfer coefficient, E, will be assumed constant. According to Equation (C-31) this assumption is conservative for wall heating since E varies approximately as $T_G^{1/4} P_G^{1/2}$ and therefore decreases with time. It should also be pointed out that E could be considerably higher if the boundary layer is turbulent over most of the length ℓ. Thus, while the solutions to be given below will indicate the relative effectiveness of the insert in protecting the arc chamber walls, the actual temperatures computed should be considered only as order of magnitude estimates of the temperatures which may exist.

The solution for the insert temperatures may be written with the aid of the Duhamel formula as

$$\frac{T(r,t) - T_o}{T_G(o) - T_o} = \phi(r,t) + \int_o^t \frac{\partial}{\partial(t-\tau)} \left[\frac{T_G(t-\tau)}{T_G(o)} \right] \phi(r,\tau)\, d\tau \qquad \text{(C-34)}$$

where

$$\phi(r,t) = \frac{T^c(r,t) - T_o}{T_G(o) - T_o} \qquad \text{(C-35)}$$

$T^c(r,t)$ is the solution for the case when $T_G(t) = T_G(o)$ and T_o is the initial insert temperature (room temperature).

Advantage may again be taken of the small times involved and $\phi(r,t)$ may be taken as the solution, $\phi(x,t)$, for the case of a semi-infinite one-dimensional slab subject to the heat transfer given by Equation (C-32) at the boundary

x = o and insulated at x = ∞. Proof that $\phi(r, t) \simeq \phi(x, t)$ for the conditions of interest will be shown below when the cylinder and slab solutions are compared in a typical example.

Proceeding to the solution for $\phi(x, t)$ we have the following boundary value problem:

$$\begin{aligned} &\frac{\partial \phi}{\partial t} = K \frac{\partial^2 \phi}{\partial x^2}, \qquad x > o, \qquad t > o \\ &\phi(x, o) = o, \qquad x > o \\ &\frac{\partial \phi(o, t)}{\partial x} = -\frac{E}{k} [T_G(o) - T_o][1 - \phi(o, t)], \qquad t > o \\ &\lim_{x \to \infty} \phi(x, t) = o, \qquad t > o \end{aligned} \tag{C-36}$$

The solution to this problem is

$$\phi(x, t) = \operatorname{erfc}\left(\frac{x}{2\sqrt{Kt}}\right) - \left[\exp\left(\frac{\alpha x}{\sqrt{K}} + \alpha^2 t\right)\right] \operatorname{erfc}\left(\frac{x}{2\sqrt{Kt}} + \alpha\sqrt{t}\right) \tag{C-37}$$

where

$$\alpha = \frac{E\sqrt{K}}{k}$$

Equations (C-33), (C-34), and (C-37) (with $\phi(x, t)$ substituted for $\phi(r, t)$) together with the gas temperature variation determine the desired insert temperatures.

The computational procedures for determining the desired temperatures can be further facilitated by taking additional advantage of the small times involved and by expressing the gas temperature analytically for the case of a perfect gas. (The true insert temperatures will be bounded by the perfect gas solutions for $\gamma = 1.2$ and $\gamma = 1.4$.) From above, the gas temperature can be written

$$\frac{T_G(t)}{T_G(o)} = \frac{1}{[1 + Bt]^2} \tag{C-38}$$

where

$$B = \frac{(\frac{\gamma - 1}{2})(\frac{\gamma + 1}{2})^{-\frac{\gamma + 1}{2(\gamma - 1)}}}{V/A_t a_c(o)} \tag{C-39}$$

Thus,

$$\frac{T(x,t) - T_o}{T_G(o) - T_o} = \phi(x,t) - 2B \int_o^t \frac{\phi(x,\tau)d\tau}{[(1 + Bt) - B\tau]^3} \tag{C-40}$$

First consider the case for x = o, i. e., the inside wall temperature. By expanding the exponential and error function in Equation (C-37) for small values of $\alpha\sqrt{t}$ and retaining only first order terms, Equation (C-40) becomes integrable. The result is

$$\frac{T(o,t) - T_o}{T_G(o) - T_o} = \frac{\alpha}{\sqrt{\pi}} \left\{ \frac{t^{1/2}}{1 + Bt} + \frac{J_1}{1 + Bt} + \frac{2\alpha^2}{B}[t^{1/2} - J_1] + \frac{2\alpha^4}{B^2}[(3 + Bt)t^{1/2} - 3J_1(1 + Bt)] \right\} - \alpha^2 \left\{ \frac{t}{1 + Bt} + \alpha^2 \left[\frac{t}{B} - \frac{1}{B^2} \ln (1 + Bt) \right] \right\} \tag{C-41}$$

where

$$J_1 = \frac{1}{2\sqrt{B(1 + Bt)}} \ln \left[\frac{(1 + Bt) + \sqrt{Bt(1 + Bt)}}{(1 + Bt) - \sqrt{Bt(1 + Bt)}} \right] \tag{C-42}$$

For $x \neq o$, $\phi(x,t)$ cannot be put in power series form since there is no expansion for $\exp(x^2/4kt)$ for small time. However it is useful to expand the

error function for small time (large argument) and there results

$$\phi(x, t) = \frac{4K\alpha}{x^2\sqrt{\pi}} \frac{t^{3/2}}{e^{\frac{x^2}{4Kt}}\left[1 + \frac{2\alpha\sqrt{K}\,t}{x}\right]}, \qquad x \neq o \tag{C-43}$$

In summary, the insert temperature for x = o is given by Equations (C-41) and (C-42), and for x > o by Equations (C-40) and (C-43). For x > o a numerical integration cannot be avoided. *

Evidence of both the applicability of the slab solution and the further small time approximations is shown in Figure C-10 where the inner wall temperature solution given by Equation (C-40) is compared with the exact (computer) solution for a cylinder.(C-7) The cylinder solution presents $\phi(r, t)$ graphically so that a numerical integration using Equation (C-34) was necessary. Aside from the scatter introduced by this numerical integration, there appears to be nearly perfect agreement between the cylinder and slab solutions. The initial gas conditions and geometry for this solution were those corresponding to the solutions in Figures C-1 to C-3. The insert material was a low carbon steel

$$\left(k = .00722 \frac{BTU}{ft\text{-}sec\text{-}^oR}, \quad \rho c = 64 \frac{BTU}{ft^3\text{-}^oR}\right)$$

and the heat transfer coefficient was $E = 0.695 \frac{BTU}{ft^2\text{-}sec\text{-}^oR}$. The value of E was arbitrarily reduced from $0.985 \frac{BTU}{ft^2\text{-}sec\text{-}^oR}$ which is computed from Equation (C-33) so that the parameters involved would coincide with the cylinder solutions of Reference C-7.

Both the inner and outer wall temperatures are shown for AISI Type 304 stainless steel $\left(k = .00261 \frac{BTU}{ft\text{-}sec\text{-}^oR}, \rho c = 59.3 \frac{BTU}{ft^3\text{-}^oR}\right)$ in Figure C-11. The

*Of course, these solutions are restricted to small times which, in physical terms, means that the thickness over which heating occurs is small compared to the radius of the insert.

initial gas conditions and chamber geometry were the same as in Figure C-10. These calculations were based on Equations (C-40), (C-41), and (C-43) (slab solution, E given by Equation (C-33)). The equilibrium gas case is bounded by the $\gamma = 1.2$ and $\gamma = 1.4$ perfect gas cases. It can be seen that the insert is very effective in protecting the arc chamber walls. In view of the negligible rise in temperature at the outer wall of the insert it appears feasible to use a better conductor for the higher initial gas temperatures in order to prevent melting of the insert. Other materials and initial gas conditions should be checked.

REFERENCES

C-1. Feldman, S., "Hypersonic Gas Dynamic Charts for Equilibrium Air," Avco Research Laboratory, January, 1957.

C-2. Hilsenrath, J., Klein, M., and Woolley, H. N., Tables of Thermodynamic Properties of Air Including Dissociation and Ionization from 1500°K to 15,000°K, AEDC-TR-59-20, December, 1959.

C-3. Carslaw, H. S., and Jaeger, J. C., Conduction of Heat in Solids, Oxford University Press, First Edition, 1946.

C-4. Churchill, R. V., Operational Mathematics, McGraw-Hill, Second Edition, 1958.

C-5. Jahnke, E., and Emde, F., Tables of Functions, Dover Publications, Fourth Edition, 1945.

C-6. Cohen, C. B., and Reshotko, E., Similar Solutions for the Compressible Laminar Boundary Layer with Heat Transfer and Arbitrary Pressure Gradient, NACA Report 1294, 1956.

C-7. Hatch, J. E., Schacht, R. L., Albers, L. U., and Saper, P. G., Graphical Presentation of Difference Solutions for Transient Radial Heat Conduction in Hollow Cylinders with Heat Transfer at the Inner Radius and Finite Slabs with Heat Transfer at One Boundary, NASA TR R-56, 1960.

APPENDIX D

SCHLIEREN DESIGN CONSIDERATIONS

by

K. R. Sivier

INTRODUCTION

The very low flow densities achieved in Hotshot tunnels result in serious problems in flow visualization. For example, conventional optical systems (i. e., those sensitive to light ray deflections greater than about 2 seconds of arc) become ineffective, even for the strongest shock waves, as the flow Mach number approaches 20. Thus, visual study of bow shocks, separated flows, wakes, etc., are precluded in the very flow regime which justifies the Hotshot tunnel. In addition, a sensitive flow visualization technique is required for direct flow velocity measurements by means of a spark-created flow disturbance, e. g., Reference D-1.

In order to provide the Hotshot tunnel with an effective flow visualization tool, a high sensitivity schlieren system was designed and procurred. Following Reference D-2, the system was designed for a sensitivity of 1 microradian (approximately 0. 2 seconds of arc). Conversations with schlieren system fabricators confirmed that, although this was an extreme requirement in terms of current manufacturing practices, it was nevertheless a feasible requirement. Since most of the auxiliary equipment was already on hand (light source, knife-edge, mounting piers), it was necessary to procure only the optics and the mounting cells.

In procurring the system, a deviation from standard practice was used. Instead of specifying the quality of each optical component, a performance-type specification was prepared. This specification required that the manufacturer fabricate each component of the system such that the assembled system would possess the one microradian sensitivity. As part of the contract, the manufacturer was to assemble and test the complete optical system in his shop. A demonstration of the one microradian sensitivity was required before the system was accepted for delivery.

SYSTEM DESIGN

Introduction

In the design of the system, only the geometry necessary to obtain a one microradian sensitivity was considered. Problems involving the quality of the optical components, corrections for off-axis aberrations, etc., were handled by the use

of a performance-type specification which left the solution of these problems to the supplier of the system. The geometric design itself was based on the material presented in References D-2 and D-3. A system aperture of 12 inches was selected to be compatible with the window ports in the test section.

System Descriptions and Design Equations

Figure D-1 shows sketches of the three types of schlieren systems considered: i. e., single-pass parallel (Toepler), double-pass parallel, and double-pass non-parallel. The double-pass systems possess an advantage, over the single-pass, of being basically twice as sensitive because the light rays pass twice through the optical disturbance in the test section. The double pass does not significantly degrade the image quality as long as the light deflections (by the disturbance) are small and the mirror is kept close to the test section.

In the sketches of double-pass systems in Figure D-1, the beam splitters permit the incident and reflected beams to be coincident. However, the use of a beam splitter results in a 75% loss in light intensity. This loss may prove unacceptable in high sensitivity systems which, typically, have large focal lengths. As an alternate method, the incident and reflected beams can be separated by a small, beveled folding mirror placed just ahead of the knife edge, if a small angle of non-coincidence can be tolerated. Additional information on non-parallel and double-pass systems may be found in Section II-(j)-(5), pages 21 and 22, Reference D-2.

In the absence of the knife edge, the illumination of the image plane is given by (Equation 13, Reference D-2)

$$I_o = \frac{Bbh}{m^2 f_1^2} \qquad \text{(D-1)}$$

where I_o = illumination in candles per square meter (= meter-candles)

B = source brightness in candles/cm^2 (= stilb)

b = source width in cm.

h = source height in cm.

m = magnification of the image on the image plane

and f_1 = focal length of the first mirror in a single pass system, in meters

= f_p, the focal length of the parabolic mirror in a double-pass parallel system

= R, the radius of curvature of the spherical mirror in a double-pass, non-parallel system.

The height of the source image, at the knife edge, is $(f_2/f_1)h$ where

f_2 = focal length of the second mirror in a single pass system, in meters,

= f_p or R in double pass systems.

Therefore, if the knife edge is used to cut off all of the source image except a height h', then the illumination of the image plane becomes

$$I = \frac{Bbh'}{m^2 f_1 f_2} \qquad \text{(D-2)}$$

where I = illumination in meter-candles

and h' = height of the source image not cut off by the knife edge, in cm.

Equation D-2 can be used directly to check the adequacy of the light source once the various system parameters have been selected.

If the disturbance, in the test section, produces an angular deflection of ϵ in the rays of the light beam, then the change in illumination at the corresponding point on the image plane is (Equation 15, Reference D-2)

$$\Delta I = \frac{Bbn\epsilon}{m^2 f_1} \qquad \text{(D-3)}$$

where ϵ = angular light ray deflection (measured in the plane perpendicular to the knife edge) occurring in one pass through the test section disturbance, in radians

and n = number of times the light ray passes through the disturbance

= 1, for the single-pass system

= 2, for the double-pass systems.

Now the relative illumination change caused by the disturbance ϵ is

$$C = \frac{\Delta I}{I} = \frac{nf_2}{h'} \epsilon \tag{D-4}$$

or solving for ϵ gives

$$\epsilon = \frac{Ch'}{nf_2} \tag{D-5}$$

Equation D-4 is the principal geometric design equation relating the geometric parameters (n, h', f_2) with the performance parameters (C, ϵ).

The Design

Equation D-5 shows the advantage of the double-pass systems. Compared to an otherwise similar single-pass system, the double-pass system will be able to detect one-half the angular disturbance and, hence, is said to have twice the sensitivity. This advantage was the principal reason for selecting a double-pass system in the present case. (An additional factor in the selection was that the layout of the schlieren pads would have made a long focal length, single-pass system awkward and impractical.)

In designing the system, high sensitivity was taken as the principal consideration. Specifically, a sensitivity of at least one microradian was desired. However, it was also felt that a high image quality, consistent with the sensitivity requirement, should be obtained. Therefore, in order to avoid image degradation due to a non-parallel system, the double-pass parallel system was selected.

To determine the minimum design focal length of the system, it was necessary to estimate the minimum acceptable values for C and h'. Following the criteria of Reference D-3, which agreed in this respect with a standard schlieren system specification used by the von Karman Facility, Aro, Inc., a minimum value of 0.1 for C was selected. For h', a value of 0.1 mm ($\cong$ 0.004 inches) was selected. This value is conservative; values for h' as low as 0.001 inches can be used.

Using the above values for C and h', Equation D-4 can be used to determine the focal length required to obtain a sensitivity to an ϵ of 1×10^{-6} radians; i. e.,

$$f_p = \frac{Ch'}{n\epsilon} = \frac{(0.1)(0.1)}{(2)(1 \times 10^{-6})(25.4)}$$

$$= 196.7 \text{ inches} = 16.4 \text{ ft.}$$

Figure D-2 shows the floor layout in the Hypersonic tunnel area. The schlieren pad on the east side of the tunnel made it impractical to consider a long focal length, single-pass system: such a system would have required an awkward folded arrangement. In laying out the system, three conditions were imposed.

(1) The schlieren system was to be located on the schlieren pads.

(2) The existing light source and mirror piers were to be used. The size of these piers determined how close to the edge of the pads the optical components could be placed. The resulting effective optical boundaries of the pads are shown in Figure D-2.

(3) The system was to be usable at any tunnel station from the center of the test section upstream to as close to the arc chamber face as possible.

Figure D-2 shows that, because of the effective pad boundaries, the greatest east-west optical path on the west pad is 14 feet. Since this is less than the minimum required focal length of the system (16.4 feet), it was necessary to fold the optical path on the west pad. Because of this basic necessity to fold the system, it became possible to increase the focal length of the system without making any change in the basic arrangement of the system. Therefore, the focal length was increased to 20 feet. This resulted in a theoretical geometric sensitivity of about 0.8 microradians.

Figure D-3 shows the final arrangement of the system. The maximum path, before folding, was used to minimize the off-axis angle. Since the lack of light intensity will be a serious consideration, a small non-coincidence of incident and

reflected beams was permitted so that a small transfer mirror could be used just ahead of the knife edge. (As finally procured, a beam splitter was also included for use in those cases where sufficient light was available and maximum picture quality was desired.) Finally, an aspherical corrector lens was included to correct the image for aberrations due to the off-axis arrangement.

Light Source Adequacy

The light source adequacy was determined by comparing the exposure (illumination times exposure time) available from a given light-source/photographic-system combination with the exposure required by standard films. The available exposure was calculated by the following relation, which is based on Equation D-2.

$$E = It = \frac{Bbh' t}{m^2 f_p^2} \qquad \text{(B-6)}$$

Three light sources were considered: (1) the BH-6 mercury arc lamp (General Electric); (2) the PEK-109 mercury arc lamp (PEK Labs., Sunnyvale, California); and (3) a conventional spark source. These sources were evaluated in conjunction with Fastax motion picture photography and 4 x 5-inch, single frame photography. The Fastax image is about 10 mm in length giving a magnification of 3.3×10^{-3} for the 12-inch aperture schlieren system. The magnification for the 4 x 5-inch image is 0.24.

The source image height, h', at the knife edge was taken as 0.1 mm for all cases. The source width was dependent on the source: (1) although the BH-6 arc is about 25 mm long, a 1 mm source width was assumed; (2) the PEK-109 has an arc size of 0.012 x 0.012 inches yielding a maximum source width of about 0.3 mm; (3) the spark source width was assumed to be 1 mm.

Exposure time is dependent on the type of photography used. For the Fastax photography, the minimum exposure time was taken to be about 1×10^{-4} seconds; corresponding to a framing rate of about 7000 frames per second. For single

frame photography, two modes were considered; shutter controlled exposure at 1×10^{-3} second and spark or flash photography. Existing equipment allows the BH-6 tube to be flashed with a duration of about 5×10^{-6} seconds. The spark duration was taken as 0.1×10^{-6} seconds.

Values of source brightness were obtained as follows: (1) the BH-6 value of 30,000 stilb from Reference D-2; (2) the PEK-109 value of 140,000 stilb from the PEK brochure; and (3) the spark brightness of about 1×10^{-8} stilb from Reference D-3.

The results of the exposure calculations are presented in Table D-1. Table IV from Reference D-2 shows that an exposure of 1×10^{-3} meter-candle-seconds corresponds to an ASA rating of 400. Since standard film is available in this speed range, all photographic modes considered are possible except for the BH-6 flash. Even this may be possible by using ultra-fast film (e. g., Polaroid 3000) reducing the image size, and increasing the source width.

INITIAL EVALUATION

The schlieren system was fabricated by Tinsley Laboratories, Berkeley, California. As part of the contract, they performed a demonstration test of the system in their shop. This test served to demonstrate the sensitivity and quality of the system.

Because of the sensitivity of the system, room air disturbances made short exposure pictures and direct viewing relatively useless. To eliminate the room air disturbances, long time exposure pictures (30 to 60 seconds in length) were made. The long exposures served to "integrate" the disturbances and permit a relatively clear field in the picture.

In order to satisfy the one microradian disturbance requirements, it would have been necessary to use a glass wedge (index of refraction of about 1.5) with an angle of about 0.4 seconds of arc. Tinsley was not able to produce a 0.4 second wedge of sufficient quality to be useful. Therefore, an indirect

TABLE D-1

Exposures Obtainable with Various
Light-Source/Photography-System Combinations

f_p = 20 ft (= 6.1 m); h' = 0.1 mm

Fastax Photography: m = 3.3×10^{-2}

Source	Brightness, B Stilb*	Assumed Source Width, b mm	Exposure Time, t sec	Exposure, E meter-candle-sec**
BH-6	3.0×10^{4}	1.0	1×10^{-4}	2.44×10^{-3}
PEK-109	1.4×10^{5}	0.3	1×10^{-4}	3.41×10^{-3}

Single Frame Photography: m = 0.24

Source	Mode	Brightness, B Stilb	Assumed Source Width, b mm	Exposure Time, t sec	Exposure, E meter-candle-sec
BH-6	Shutter	3.0×10^{4}	1.0	1×10^{-3}	3.37×10^{-3}
BH-6	Flash	3.0×10^{4}	1.0	5×10^{-6}	1.68×10^{-5}
PEK-109	Shutter	1.4×10^{5}	0.3	1×10^{-3}	4.70×10^{-3}
Spark	----	1.0×10^{8}	1.0	1×10^{-7}	1.12×10^{-3}

* 1 Stilb = 1 candle/cm^2

** 1 meter-candle-sec = 1 $\frac{\text{candle-second}}{(\text{meter})^2}$

demonstration, using a 2 second optical wedge, was made. With the system adjusted to maximum sensitivity and the 2 second wedge in the field of view, a series of time exposures were taken on glass photographic plates. Exposures ranged from 30 to 60 seconds.

The developed plates were analyzed using a microdensitometer to provide quantitative measurements of the image density on the plates. A reproduction of a typical plate is shown in Figure D-4a and the corresponding density data are shown in Figure D-5a. By comparing the average image density for the several plates, it was possible to determine the slope of the log density to log exposure curve for the plates. This slope then was used to convert the image density data into relative exposure data. Since, for any given plate, all points were exposed the same length of time, the relative exposure is directly proportional to the relative image illumination. Illumination data, corresponding to the density data of Figure D-5a, are shown in Figure D-5b.

The illumination data for the general field were compared to those for the optical wedge. This yielded information on the change in image illumination due to the 2 second optical wedge. Averaging the results from all plates, showed that the wedge produced an illumination change of about 55%. This corresponds to about 11% for a 0.4 second wedge; this was taken as a demonstration that the system met the one microradian sensitivity specification.

The above tests were done without the windows in the optical path. A later check was made of the image quality with the windows included. A reproduction of a plate made in this test is shown in Figure D-4b. Note that a different wedge was included in this picture. This picture illustrates the reduction in image quality introduced by the windows.

REFERENCES

D-1 Merrit, G. E., "Velocity Measurements in the University of Southampton Hypersonic Gun Tunnel," Univ. of Southampton AASU Report No. 172, Apr. 1961.

D-2 Holder, D. W., and North, R. J., "Optical Methods for Examining the Flow in High-Speed Wind Tunnel, Part I, Schlieren Methods," AGARDograph 23, Nov. 1956.

D-3 Thomas, G. M., "A Schlieren System for the Stanford Spark-Heated Hypersonic Wind Tunnel and Studies of Blast Wave Propagation," Stanford University Aeronautical Engineer Thesis, June 1961.

APPENDIX E

SPARK VELOCITY MEASUREMENTS

by

E. Oktay and K. R. Sivier

INTRODUCTION

The velocity of the flow in a hypervelocity wind tunnel can be measured by means of a spark-generated disturbance; e. g. , References E-1, E-2, and E-4. With this method, a shock wave is generated by a high energy spark formed between two electrodes placed in the flow. The shock wave travels outward from the original spark column and, at the same time, is transported downstream with the velocity of the flow. At some known time interval after the spark discharge, a schlieren picture is taken of the shock wave. By measuring the distance the center of the shock wave has traveled from the electrodes and knowing the time interval, the flow velocity can be determined.

The apparatus, necessary to make such flow velocity measurements, has been assembled and preliminary tests of its operation have been made. The following discussion describes the design and operation of the apparatus and summarizes the results of the preliminary tests.

APPARATUS

The apparatus consists of the following components: trigger unit, double stage time delay unit, disturbance spark system, initiating spark source for the BH-6 mercury lamp used as the schlieren light source, schlieren light source, phototube, and oscilloscope. The block diagram for the apparatus is shown in Figure E-1, and details of individual components in the system are shown in Figures E-2 through E-7.

Upon the triggering of the double stage time delay unit, the delayed pulse No. 1 initiates the disturbance spark and, approximately one hundred microseconds later, the delayed pulse No. 2 fires the schlieren light source. An inductive pickup detects the initiation of the disturbance spark and triggers the oscilloscope. The phototube detects the firing of the light source and its output is recorded on the oscilloscope to determine the time interval between the generation of the shock wave and schlieren picture.

For the experiments with flow (tunnel operation), the double stage time delay unit is triggered by the output of an inductive pickup, excited by the collapse of the field of the tunnel's energy supply coil. For the present static experiments, the inductive pickup is replaced by the trigger unit shown in Figure E-3.

Delayed pulses No. 1 and No. 2 are put out by the transformers in the plate circuits of tubes 2 and 4 of the double stage time delay unit shown in Figure E-2. This unit is designed such that the time delay between the input from the trigger unit and the delayed pulse No. 1 is adjustable from 5 to 50 milliseconds, and the time delay between the delayed pulse No. 1 and the delayed pulse No. 2 is adjustable from 10 to 800 microseconds. The time delay of both pulses is changed to the desired value by changing the rise time of voltage to the firing level on the grids of tubes 2 and 4.

The disturbance wave is created by discharging a 0.3 μfd/8KV (9.6 joules) capacitor at the electrode tips in the tunnel test section. A 5C22 thyratron functions as a switch in the discharge circuit shown in Figure E-4. In order to eliminate excessive external inductance, RG 8/U coaxial cable is used between the capacitor and the electrodes.

For the static tests reported here, a BH-6 mercury lamp was used as the schlieren light source. The BH-6 lamp was flashed by discharging a 2 μfd/3KV (9 joules) capacitor through it. In this circuit, Figure E-5, a system of three probes was used as the switching element. The time duration of the BH-6 flash is about five microseconds.

An inductive pickup from the discharge of the disturbance spark capacitor triggers the scope, and the output of a phototube from the spark at the three probe system is connected to the input of a Tektronix 551 oscilloscope. Since there is no time delay between the breakdown of the three-probe system and the flashing of BH-6 lamp, the time delay between the initiation of the disturbance spark and the flashing of the schlieren light source is thus determined.

PRELIMINARY TESTS AND RESULTS

After the components were assembled, the system was operated in conjunction with a small (6 inches in diameter and 13 inches long) vacuum chamber.

At this phase of the experiment there were two major problems: (a) the functioning of the double stage time delay unit was not consistent, and (b) a proper grid circuit was required for the 5C22 thyratron, Reference E-3.

It was noted that the inconsistency in the functioning of the double stage time delay unit was due to the failure of 2D21 thyratrons. Also, the screen grids of these thyratrons have a significant effect on the operation of the tubes, and improper voltage settings of these supressor grids result in inconsistent time delays.

Using the small vacuum chamber as a substitute for the tunnel test section, it was possible to set up the system as shown in Figure E-1, and a satisfactory functioning of the system was obtained. The spark was initiated in the vacuum chamber, and the light source was flashed; the time interval between the two events was recorded on the oscilloscope.

No detailed or quantitative study was made to determine the range of vacuums where a spark can be initiated. Due to the physical size of the vacuum chamber, the largest possible electrode gap was 3/4 inch, whereas for the actual experiment it is planned to have an electrode gap of three inches. Since the electrode gap distance and the vacuum are interrelated in initiating a spark, data obtained with a 3/4-inch gap would not be useful for a three inch gap.

As the second step, the electrodes were installed in the tunnel test section. At this phase, the following electrical problem was encountered. It was noted (see Figure E-5) that the cathode of the 5C22 was at ground potential prior to firing and rose to 8 KV (charging potential of the capacitor) upon the firing of the tube. This change of the potential of the 5C22 was transmitted to the 110 V. outlet through the filament transformer of the tube.

For the first tests, the electrode gap was 5/32 inch, resulting in a nearly spherical wave. Figure E-8 shows a typical schlieren photograph of such a wave taken eighty microseconds after the disturbance spark was initiated at the electrode tips. The vacuum inside the test section was about 220 mm Hg, and the charging potential of the capacitor was 9 KV. This picture shows the poor optical quality of the plate glass tunnel windows which were used during these tests.

Figure E-9 shows an axial view of a cylindrical wave from a spark initiated between electrode gap of 1 7/8 inch, taken 200 microseconds after the spark was initiated. The vacuum was 150 mm Hg, and the charging potential of the capacitor was 9 KV. Both pictures were taken on Polaroid type 52 film.

CONCLUSIONS

On the basis of the preliminary tests of the flow velocity apparatus, the following conclusions can be drawn:

1. The apparatus functions properly and appears to be ready for use in measuring flow velocities.
2. The BH-6 lamp can be flashed sufficiently fast to satisfactorily "stop" the shock wave motion.
3. The existing schlieren system is inadequate for use under tunnel operating conditions, i. e. , ambient pressures below 1 mm Hg. Flow velocity measurements will require the use of the high sensitivity schlieren system described in Appendix D.

REFERENCES

E-1 Merritt, G. E., "Velocity Measurements in the University of Southampton Hypersonic Gun Tunnel," Univ. of Southampton, AASU Report No. 172, April 1961.

E-2 Karamcheti, K., Vali, W., Kyser, J. B., and Rasmussen, M. L., "Measurements of Pressure and Speed of Flow in a Spark-Heated Hypersonic Wind Tunnel," Arnold Engng Development Center, AEDC-TDR-62-218, November 1962.

E-3 Karamcheti, K., Vincenti, W. E., "Development of Tracer Spark System for the Measurement of Hypersonic Flow Fields," Dept of Aeronautics and Astronautics, Stanford Univ., December 1962.

E-4 Thomas, G. M., "A Schlieren System for the Stanford Spark-Heated Hypersonic Wind Tunnel and Studies of Blast Wave Propagation," Dept. of Aeronautics and Astronautics, Stanford Univ., June 1961.

APPENDIX F

GASEOUS DISCHARGE PHENOMENA IN HYPERSONIC FLOW DIAGNOSTICS

by

C. E. Bond
with the laboratory assistance of E. Oktay

NOMENCLATURE

A	Glow cross sectional area
a	Acceleration
d	Electrode separation distance
E	electric field intensity
e	electron charge
F	force
I	current
I_o	Initial electron current at cathode
j	Current density
L	Total length of collision chain in "relay model"
M	Mass of positive ion
N	Total number of electrons reaching anode
n	Number of electrons reaching x
n_o	Number of initial electrons at cathode
P	Pressure
Q	Effective transfer cross section
q	Charge density
s	Number of collisions in "relay model" chain
t	Time
t_{av}	Average time between collisions
u	Ionic drift velocity
V	Free stream velocity
V_C	Cathode fall in voltage
V_S	Spark breakdown voltage
w	Width of glow
x	Axial distance from glow edge of cathode dark space, positive toward cathode

α	First Townsend coefficient
$\bar{\alpha}$	Townsend's mean coefficient in dark space
γ	Ratio between electronic and ionic current at cathode
λ	Free path length
λ_o	Mean free path
π	3.1416
ρ	Mass density

INTRODUCTION

The development of laboratory facilities capable of producing high-energy hypersonic gas flows has opened up a vast area of challenging new possibilities for gas dynamics research. But the opportunity for research under new and extreme conditions rests upon a concomitant development of new experimental techniques appropriate to these new conditions. For research in high-energy hypersonic flow, the standard aerodynamic measurement techniques are entirely inadequate. Standard techniques are based on assumptions of completely isentropic, non-radiative, non-ionized, non-dissociated, equilibrium flow of a gas of known chemical composition. None of these assumptions is permissible for hypervelocity flow diagnostics. It therefore becomes necessary to devise a new complex of measurement techniques for hypervelocity flow diagnostics in order to take full advantage of new opportunities for gas dynamic research presented by the development of new hypersonic laboratory facilities.

In devising any new diagnostic technique, the goal is to obtain a signal whose characteristic is, among other things, related in some known way to a flow variable of interest. The signal is produced as the result of some experiment performed on a flow sample. The experiment must not disturb the flow to the point where there is any significant change in the variable being measured. In hypervelocity flow it is difficult to devise diagnostic experiments which do not cause radical changes in the variables of interest. This is also true of supersonic flow, of course, but fortunately with the assumptions mentioned above, accurate relationships between the undisturbed values and the disturbed values can be derived. In supersonic flow there is thus little to be gained by pursuing additional limited-disturbance techniques; in hypervelocity flow with its proliferation of flow unknowns such pursuits appear much more attractive.

In this context it appears that the gaseous electrical discharge offers a promising avenue for diagnostic research. Electrons, which are here the essential charge and signal carriers, are extremely light and mobile. Thus the ratio

of signal to disturbance can be quite large and the response quite rapid. For example, in a uniform field the breakdown voltage for an electric spark depends on conditions in the gas between the electrodes pertaining before breakdown occurs. Breakdown voltage is thus a "signal" which should be masked only to the extent that the electrodes disturb the flow. This has been shown to be the case in Reference F-1 where it was found that in air-flow at a Mach number of 5.8 the spark-breakdown voltage is dependent only on conditions in the stream just before breakdown and that if corrections are made for the density changes through the electrode boundary layer, the breakdown voltage depends only on the product of density with electrode separation distance, ρd, according to the Paschen curve obtained in still air. Two problems in applying this example to the measurement of density in a hypervelocity flow are first, obtaining a calibration curve equivalent to the still "air" Paschen curve so that chemical composition is accounted for and second, calculating or eliminating the necessary correction for electrode boundary layer.

Another example of an electric discharge which causes little flow disturbance is the Townsend discharge, which is defined in References F-2, F-3, and F-4, for example, as a non-selfsustaining discharge in which electrons released at the cathode by some external agency are accelerated by an electric field to the point where they cause additional ionization by collision, but which is defined in References F-5 and F-6, for example, as the self-sustaining discharge which occurs at higher current when a secondary emission mechanism (such as positive ion bombardment at the cathode) just becomes capable of sustaining the discharge. Both these will be referred to here as Townsend discharges. A Townsend discharge always occurs just before spark breakdown. But whereas the spark breakdown potential can only be measured at specific instants in time, the Townsend discharge can provide a continuous signal. Four problems in applying the Townsend discharge to the measurement of density are: measuring the effects of chemical composition, determining the effect of velocity, measuring the small current involved, and where applicable, controlling the emission of electrons at the cathode.

The glow discharge obviates the problem of controlling cathode emission since it is self-sustained, providing its own cathode electrons by ion and photon bombardment. The glow adds considerably more energy to the gas than does the Townsend discharge and thus requires more attention to the problem of flow disturbance. As with the Townsend discharge, the voltage-current characteristic of the glow discharge is related to gas density. And like the Townsend discharge the glow discharge is influenced by electrode surface conditions, only moreso. But unlike the Townsend discharge the glow mechanism requires a space charge, the cathode dark space. This space charge could present problems of confining the glow discharge that are not encountered with the Townsend discharge. It should also enhance velocity effects.

The radio frequency electrodeless ring discharge is of interest here because in addition to being dependent upon properties of the gas it is—unlike the glow discharge—not dependent on electrode surface conditions. The electrodeless ring discharge adds a considerable amount of energy to the gas. Devices based on radio frequency discharges must of course be calibrated in a way which takes into account the energy lost through radiation.

Ranking highest in energy addition, the electric arc could be considered, for example, as a possible light source for inflight, time-resolved spectrochemical analysis. But any use of the electric arc pressupposes solution to the difficult problem of stabilizing the arc at such high velocities. This problem is not as serious with the other forms of discharge because they do not require thermal ionization as the arc does.

Perhaps the greatest obstacle to the application of any form of gaseous discharge to the diagnostics of hypervelocity flow produced in the laboratory is the elimination or use of the effects of the chemical contaminants usually found in such flow.

The following sections contain a discussion of related literature, outlines of Townsend, breakdown, and glow theory, a discussion of some rudimentary

experimental work conducted to get an idea of the practical problems involved in discharge density measurements, and, finally, recommendations for further work.

LITERATURE

The basic literature on gaseous discharges is vast. Many of the fundamental discoveries of physics have been made through the study of gaseous discharges; and though the field is still far from exhausted, yet there exists a priceless fund of knowledge which the research engineer cannot afford to ignore in any attempt to apply gaseous discharge phenomena. There will be here, however, no pretense at reviewing any appreciable fraction of this basic literature.

The 1956 edition of Volume XXII of the Handbuch der Physik (Reference F-7), provides an excellent reference on almost every phase of discharge phenomena. It contains several classic review articles which cover in depth and give countless references on such discharge phenomena as electric breakdown, the spark, the glow discharge, the high frequency discharge, the lightning discharge, the Townsend discharge, and the electric arc. It should be noted that all of these articles are written in English except the one on electric arcs—and even this one is available in translation (Reference F-8).

Another classic book which should be mentioned here is the one by Loeb which in its latest version is called "Basic Processes of Gaseous Electronics," Reference F-9. This book is especially valuable for its detailed discussion of modern (1955) experimental techniques in this field. (This is also true to a lesser extent of Loeb's article in the Handbuch, Reference F-10.) It contains exhaustive information on such things as the Townsend coefficients, and its usefulness as a reference is only slightly impaired by the omission of units from some figures and quantities.

Two books which cover gaseous conduction from an elementary point of view are "Gaseous Conductors," by Cobine, Reference F-2, and "Theory of Gaseous Conduction and Electronics," by Maxfield and Benedict, Reference F-11.

Compared to the basic literature, the literature on the application of discharge phenomena to flow diagnostics seems tractable. In a sense this literature is also "basic" since it treats discharge phenomena under a new condition, under the influence of forced convection. Volume IX of the Princeton series (Reference F-12) contains an article on "Electric Discharge Anemometry" which summarizes the work done through 1951 in this field. It serves no purpose to repeat here the review of all the papers mentioned there. But a few remarks will be made in the next three paragraphs.

First it is noted that Fucks (Reference F-13) designed a Townsend discharge probe which exhibited a velocity sensitivity, $(dI/I)/(du/u)$, of from .5 to 1.0.

Referring to Werner's work (Reference F-14) with a glow discharge from pointed electrodes (Corona) which indicated a pressure (actually density) sensitivity, $(dI/I)/(dp/p)$ of about .5 and velocity sensitivity 25 times lower, it is suggested that such an instrument might be useful as a barometer.

Works by Lindvall and others are referred to which indicate that perhaps the type of discharge most suitable for velocity measurements is the glow discharge. Several arguments are given to support the theory that the glow data is velocity-dependent due to the convection of ions rather than to physical deflections, convective cooling, or pressure (density) effects. Finally, a discussion is given of the deleterious effects of surface sputtering on instrument reliability, effects which make frequent calibration necessary.

A more recent (1955) paper by Fucks (Reference F-15) on "Gas Discharges Applied to Measurement" lists the advantages of discharge diagnostics tersely as follows: "negligible inertia in many cases; no repercussions on the primary process; direct measurement (by means of a calibrated electric signal)." Fucks

prefers the corona discharge probe and gives some conditions for the corona measurement of pressure independent of other flow effects.

Marlotte in Reference F-16 investigated the spark and glow discharges in hypersonic flow at a Mach number of 5.8 at densities an order of magnitude higher than those in the Hotshot range. Marlotte considers the general theoretical treatment of discharges in hypersonic flow to be virtually hopeless. But the experimental data he presents seems to be the first of its kind published for such high convective velocities (about 2000 ft/sec) and should be quite useful for comparison with any new theoretical treatment.

Sharbaugh, et al., in Reference F-17 present the results of an interesting experiment conducted to determine the effect of temperature on spark breakdown voltage. They make use of a shock tube to produce shock-heated nitrogen between electrodes carefully designed to produce a uniform electric field. They found that Paschen's law holds for nitrogen at temperatures up to 1100°K but that breakdown potential decreases by as much as 50% at 4000°K. They also found that convection at velocities up to 6000 ft/sec does not greatly affect the breakdown strength of nitrogen. In addition the authors make some interesting inferences as to ionization relaxation times in nitrogen.

Werner in Reference F-18 discusses the use of the corona anemometer for the measurement of supersonic turbulence. A series of probe designs was tested. The last of these consisted of a central pointed corona electrode with two parallel electrodes on opposite sides. Each of the side electrodes is in two segments and thus is actually two electrodes in tandem. The central electrode is considered as merely a source of ions. These ions follow trajectories determined by the combined effects of the applied electric field and the flow field. The difference between the currents to the side electrodes is indicative of the side component of velocity. The difference between the currents to the fore and aft segments of the side electrodes indicates the axial velocity component. The total current to the middle electrode is a function of both velocity and density. In order to

isolate density fluctuations from velocity fluctuations it was necessary to determine at least the first order interaction coefficients between ρ and v by calibration at the conditions of operation. Werner mentions many of the practical problems, such as unwanted sparking, which plague investigators in this field.

In Reference F-19, Mary Romig gives results of a theoretical study of flow through an rf discharge with particular emphasis on determining the electron density distribution and the effects of convection on it.

Excellent papers on the electrodeless ring discharge in still gases are given by Strauss and Schluter in References F-20 and F-21 and papers on the general high frequency discharge are given in References F-22, F-23, F-24, F-25, and F-26.

A comprehensive treatment of the glow discharge in still gases is given in the classic paper of Gordon Francis in Reference F-5. A more recent review (1960) of the glow discharge is given, along with a theoretical treatment by the authors, in Reference F-27—this theoretical development is summarized in part in another section on the present survey.

An experimental study of the glow discharge with convection (both axial and transverse) is reported by Maier in Reference F-28. In this paper, Maier gives an extensive qualitative discussion of the glow with convection and observes that though the (stable) glow as not displaced by the flow (120 ft/sec), the glow voltage was increased in a manner almost proportional to the transverse velocity. It also increased with pressure. Maier makes the interesting observation that when the glow is operating in a "discontinuous" (intermittent) fashion, as it is for certain circuit conditions (see p. 187, Ref. F-5), the entire discharge configuration moves with the velocity of the flowing gas.

Oertel in Reference F-29, discusses the measurement of the density variation and propagation velocity of detonation waves by means of the corona probe.

And, finally it should be mentioned that Werner in Reference F-18 found that the glow (corona) discharge is markedly pressure (density) sensitive, has low

velocity sensitivity (up to 300 ft/sec), is only slightly humidity sensitive and is not sensitive to ordinary temperature variations. The apparent disparity between Werner's conclusion of velocity independence and the earlier work of Maier (of which Werner was apparently unaware) showing linear dependence is not as diametric as would seem, since Werner's current from a pointed probe was on the order of micro-amperes in magnitude whereas Maier's was milli-amperes.

THEORY OF THE TOWNSEND DISCHARGE AND BREAKDOWN PROBES

It is instructive to consider the basic mechanisms involved in the Townsend discharge and the Townsend criterion for spark breakdown. These can be simply outlined as follows.

When an electric field E exists between two plate electrodes, electrons emitted at the cathode, say by photoelectric means, will travel to the anode. If the field strength is high enough, for a given gas density, these electrons will be accelerated to the point where they cause ionization by collision before reaching the anode. If at a given value of E/ρ there are α electrons liberated by the collisions of each electron in moving one unit of length, then the number dn liberated by n electrons in length dx is

$$dn = \alpha n dx \tag{F-1}$$

where n is the number of electrons crossing at x.

Integrating,

$$n = n_o e^{\alpha x} \tag{F-2}$$

If the electrode separation is d, the total number of electrons, N, reaching the anode is $n_o e^{\alpha d}$, each initial electron having caused an avalanche of $e^{\alpha d}$ electrons. Multiplying by the electron charge and drift velocity gives:

$$I = I_o e^{\alpha d} \tag{F-3}$$

For field strengths above a certain range of E/ρ, the current is greater than that given above, due to the liberation of secondary electrons. For simplicity assume the secondary electrons to be due entirely to positive ion bombardment at the cathode. Let γ represent the probability that a single ion will liberate such a secondary electron. Following Loeb, if there are n_o photoelectrons, and n'_o total electrons liberated at the cathode, then clearly

$$n'_o = n_o + \gamma (N - n'_o) \tag{F-4}$$

Solving for n'_o

$$n'_o = \frac{n_o + \gamma N}{1 + \gamma} \tag{F-5}$$

Each of these electrons causes an avalanche of $e^{\alpha d}$ electrons to reach the anode. Thus

$$N = n'_o e^{\alpha d} = \frac{(n_o + \gamma N)}{1 + \gamma} e^{\alpha d} \tag{F-6}$$

Solving for N

$$N = \frac{n_o e^{\alpha d}}{1 - \gamma(e^{\alpha d} - 1)} \tag{F-7}$$

or

$$I = \frac{I_o e^{\alpha d}}{1 - \gamma(e^{\alpha d} - 1)} \tag{F-8}$$

This is the basic equation for the Townsend discharge.

When conditions are such that the denominator is zero, then

$$\gamma(e^{\alpha d} - 1) = 1 \qquad \text{(F-9)}$$

But $(e^{\alpha d} - 1)$ is the number of ions resulting from a single primary electron and $\gamma(e^{\alpha d} - 1)$ is the number of secondary electrons. Thus under this condition each primary electron liberates one secondary electron and the discharge is self-sustaining. Depending on external circuitry, electric breakdown of one sort or another occurs. This is Townsend's criterion for breakdown. The potential between the electrodes corresponding to this condition is the breakdown potential V_s.

It is possible to show theoretically and experimentally that α/ρ and γ are functions of E/ρ (see Reference F-9). The reason for the dependence of α on density is that ionization in the gas by electrons depends on collision processes. The reason for the dependence of γ on density is that the probability that an electron liberated at the cathode will not be returned by back-diffusion is related to gas density. These functional relationships, along with Equation F-8, show that the Townsend current will vary with ρd and E/ρ. Or, considering Equation F-9, it can be seen that Townsend breakdown will also depend on ρd and E/ρ. With uniform fields $E = Vd$ and it is seen that, for a given voltage and cathode surface condition, the Townsend current varies with ρd only. Similarly the sparking potential V_s in a uniform field varies with ρd only.

This of course is Paschen's law. The Paschen curve of V_s vs ρd is similar to the curve shown in Figure F-1. At the value of ρd where V_s is a minimum, the electron mean free path is a large fraction of the electrode separation, d. For lower densities there are less collisions so that more energy per collision and thus more voltage is required for breakdown. For higher densities, collisions are so frequent that more voltage is required to provide sufficient acceleration during the shortened intervals between collisions.

Paschen's law refers to a uniform electric field, and it cannot be expected that so simple a relationship will exist for an arbitrary field configuration. In this sense the curve given in Figure F-1 for pointed electrodes is misleading. But it should be clear that with electrode geometry and electric field configuration fixed, the Townsend current and the spark breakdown potential will be sensitive to density even in non-uniform fields.

The fact need not be of concern here that the Townsend breakdown criterion must be modified somewhat especially for $\rho d \geq 10^{-3}$ in. lb/ft^3 to account for the fact that secondary electrons liberated at the cathode apparently cannot cause breakdown in the observed times of ~ 10^{-8} seconds. Even with the more recent streamer, canal, and mid-gap streamer models for the breakdown mechanism, moreover, the breakdown criterion need only be modified to state that for each avalanche caused by a primary electron at least one electron must be liberated at a propitious location by secondary processes, where the secondary processes now include photoelectric ionization in the gas (see Ref. F-30). Regardless of mechanism, the breakdown voltage, like the Townsend current, is related to the density of the gas.

THEORY OF THE GLOW DENSITY PROBE

The requirements for the cathode dark space of the DC glow discharge are analogous to those for spark breakdown. To sustain the discharge, the "cathode fall" in voltage across the dark space and the dark-space thickness must be of the same order as that at the Paschen minimum for breakdown at the same density; this alone suggests that the glow voltage must be related to density.

Specifically the glow discharge depends on density through its effect on ionic mobility* in the cathode dark space, where ions must carry most of the

*"Mobility" is the ratio of ionic drift velocity to the strength of the electric field causing the drift. In the present case, as will be seen, it varies with field strength.

current. This effect is outlined below. But first it seems advisable to review the qualitative theory of the glow discharge as it has been developed to date in the classic discharge tube.

The presentation given here will follow closely that of Francis given in Reference F-5. The geometry is as shown in Figure F-2, with parallel plate electrodes placed in opposite ends of an evacuated tube. Most of the phenomena essential to the discharge occur in the region near the cathode (see Figure F-2). The mechanism at the cathode surface is electron emission by ion and photon bombardment. The emitted electrons are accelerated by the strong electric field which is produced by the positive space charge in the cathode dark space. The accelerated electrons move away from the cathode with beam-like properties through the cathode dark space. A thin sharp glow called the first cathode layer is produced at the distance where the electrons have acquired energy corresponding to the maximum excitation probability. Farther out, the electrons attain sufficient energy to ionize. The ionization increases with distance through the cathode dark space until a point is reached where the electric field is essentially zero. At this point there remain fast electrons which have not suffered collision and slow electrons resulting from the ionizing collisions. The slow electrons, and later the fast electrons, excite the gas causing the negative glow region. Ions travel back to the cathode and produce enough electron emission to sustain the discharge.

Next comes the Faraday dark space, in which electrons are accelerated toward the anode by the field caused by the slight excess of electrons at the edge of the negative glow. When the electrons again reach the excitation energy a low energy glow is observed. This glow extends essentially to the anode and is called the positive column. At the anode there is a negative space charge which produces the anode fall in potential.

Starting at a density where the discharge does not completely cover the cathode, decreasing the density causes the cathode area covered to increase

until it is complete. Further decrease causes the negative zones to move toward the anode. First the positive column disappears into the anode. Then follow the anode glow, the Faraday dark space, and finally the negative glow. When the negative glow disappears, the discharge is "obstructed" and ceases. The effects of density on the DC V-I characteristics are illustrated by Figure F-3 which shows data obtained here in air with a probe design for which the range of densities of interest is roughly the range between the disappearance of the anode glow and that of the cathode glow—that is, where the Faraday dark space is disappearing into the anode.

It is generally agreed that the essential phenomena of the glow discharge occur at the cathode. A recent addition to the theory of these cathode phenomena (Reference F-27) includes a thorough review of the various theories promulgated over the past hundred years. In this reference is it pointed out that the main difficulty in the development of a satisfactory theory for the cathode mechanism has been the lack of knowledge on the interaction of the positive ion space charge with its own neutrals, on the location of ionization, and on the nature of the charge carriers. The authors go through an analysis (see below) whose results are of particular interest here, including a general equation for the characteristic of the (normal and abnormal) glow discharge in a monatomic gas:

$$\frac{j}{p^2} = \frac{\left(\frac{1}{3}\right)\left(\frac{5}{6\pi}\right)^{3/2}\sqrt{\frac{e}{MQ}}\,V_c^{3/2}}{\left[\frac{\gamma}{\gamma+1}\left(e^{\frac{\bar{\alpha}}{p}pd} - 1 - \frac{\bar{\alpha}}{p}pd\,e^{\frac{\bar{\alpha}}{p}pd}\right)\frac{1}{\left(\frac{\bar{\alpha}}{p}\right)^2 pd} + \frac{1}{2}pd\right](pd)^{3/2}} \qquad \text{(F-10)}$$

It appears worth while to present the treatment of the stationary abnormal glow discharge which is given in Reference F-27 to illustrate the foundations on which a convective glow theory should be constructed. The central hypothesis which is made in Reference F-27 (and one which is shown to be good) is that the only interaction between the ions and neutrals in the cathode dark space is that

of charge-transfer. Thus it is assumed that when an ion collides with a neutral, the ion takes up an electron from the neutral, forming a new ion, and that there is negligible average change in velocity of the two particles. The ion falls a free path λ under the accelerating influence of the electric field E in the dark space. It collides with a neutral, and at this point another ion begins at zero velocity to fall through the field.

It is a good assumption that the acceleration, a, is constant and thus

$$\lambda = \frac{at^2}{2} = \frac{F}{M}\frac{t^2}{2} = \frac{Ee}{M}\frac{t^2}{2} \tag{F-11}$$

The time between collisions is therefore

$$t = \left(\frac{2M\lambda}{eE}\right)^{1/2} \tag{F-12}$$

Now it is assumed that after this time the (new) ion begins again at zero velocity so that, if there is a chain of s collisions, the total length of the chain L is

$$L = s\lambda_o \tag{F-13}$$

where λ_o = the mean free path.

The time required to complete the chain is

$$T = st_{av} = s\left(\frac{2M}{eE}\right)^{1/2}(\sqrt{\lambda})_{av} \tag{F-14}$$

now

$$(\sqrt{\lambda})_{av} = \int_o^\infty \sqrt{\lambda}\, e^{-\lambda/\lambda_o}\, d(\lambda/\lambda_o) = \frac{\sqrt{\lambda_o \pi}}{2} \tag{F-15}$$

so that

$$T = s\left(\frac{M\lambda_o \pi}{2eE}\right)^{1/2} \tag{F-16}$$

The ionic drift velocity is thus given by

$$u = \frac{L}{T} = \sqrt{\frac{2eE}{\pi MQ\rho}} \tag{F-17}$$

where

$$Q = \frac{1}{\lambda_o \rho} \tag{F-18}$$

Now the charge in the dark space is simply the ratio of current density to drift velocity, and Poisson's equation gives

$$\frac{dE}{dx} = 4\pi\, j/u = \frac{4\pi j}{\sqrt{\frac{2Ee}{\pi\, MQ\rho}}} \tag{F-19}$$

which is readily integrable assuming $\frac{\partial j}{\partial x} = o$ with the result

$$E = \left(\frac{6\pi jx}{\sqrt{\frac{2e}{\pi MQ\rho}}}\right)^{2/3} \tag{F-20}$$

This can again be integrated from x = o (the edge of the cathode glow), to x = d (the negative electrode). The integral of the electric field over the dark space gives V_c, the cathode fall in voltage, which is the major part of the glow voltage. The result is:

$$\frac{j}{\rho^2} = \frac{1}{\sqrt{18}}\left(\frac{5}{3\pi}\right)^{3/2} \sqrt{\frac{e}{MQ}}\, \frac{\left(V_c\right)^{3/2}}{\left(\rho d\right)^{5/2}} \tag{F-21}$$

This is the abnormal glow discharge. Reference F-27 also presents the more involved Equation F-10 above, for the abnormal and normal glow where ionization in the dark space by electron avalanche must be taken into account. It is pointed out in Reference F-27 that the above Equation F-21, does not contain the various coefficients for electron emission from the cathode surface and thus indicates that the abnormal glow is insensitive to the state of the cathode surface. This agrees with the tentative observation in the feasibility tests of no fundamental difference in the response of a platinum probe from that of a copper probe in the abnormal regime. For diagnostic applications this is of course an important consideration.

It is also to be noted from Equation F-21 that the abnormal glow characteristic shows a square-root dependence on gas density. This indicates a density sensitivity $(dI/I)/(d\rho/\rho)$ of .5 which agrees both with the experimental result obtained here and with that of Werner.

FEASIBILITY TESTS FOR DENSITY MEASUREMENT

In order to get some feeling for the practical problems involved in discharge diagnostics, it was decided to conduct feasibility tests for the measurement of free-stream static density. These tests were limited to the use of equipment readily available at the time. No attempt was made to obtain refined results since this would have required the use of techniques too elaborate at this stage. Several ideas were considered.

The first of these was to use the spark breakdown potential. It has been indicated in Reference F-1 that if corrections are made for the boundary layer on plate electrodes, then V_s is related to ρd by the Paschen curve for the same electrode geometry in still air. The measurement of V_s, then should indicate the free-stream density (see Appendix E). To test the feasibility of this idea a simple probe was constructed to measure V_s for various densities in the Hotshot range. The

first spark probe was pointed (see Figure F-4) as it probably would be in actual use in order to eliminate boundary layer problems and to localize the measurement. A diagram of the crude circuit used is given in Figure F-5.

Several practical problems were immediately discovered. The major one was that the spark did not strike through the shortest distance but preferred to strike between the electrode roots. To prevent this the electrodes were insulated (except at the points) with epoxy resin.

Figure F-1 shows a curve of V_s vs. ρd obtained with the insulated probe for air at densities from 10^{-4} to 2×10^{-2} atmospheres. The similarity to the classical Paschen curve is apparent. But since the electric field is not uniform, this curve applies only to the particular electrode geometry for which it was obtained; the abscissa of Figure F-1 is given as ρd rather than ρ merely for comparison purposes.

It was found that even when the terminal voltage was raised as slowly as the power supply permitted, breakdown occurred at significantly scattered values ($\pm$ 5%). The reasons for this non-repeatibility probably lay in the ripple in the rectifier voltage and changing electrode surface conditions, and it could undoubtedly be reduced. (According to Loeb, Reference F-10, p. 493, V_s for air has never been measured to better than $\pm$ 0.5%.) One practical consideration which was clear is that the increase of the terminal voltage until breakdown occurs is not a satisfactory technique for the Hotshot, where the time available is of the order of milli-seconds. A good voltage-pulse generator will be required.

The subject of breakdown repeatability is a complex one—for a comprehensive review, see Loebs' article, Reference F-10. In general it has been found that the extent to which the breakdown voltage can be exceeded for a given interval of time depends upon the interval and upon what particular breakdown mechanism is active, among other things. Fisher has indicated that for $\rho d \leq 8 \times 10^{-4}$ in-lb/ft^3 the Townsend mechanism seems to predominate, in which case the time lags would be longer. Fisher gives time lags of $\sim 10^{-7}$ sec for an overvoltage of 2 1/2% and $\sim 10^{-4}$ sec for an overvoltage of 0.02% (see Reference F-10). It seems clear that

good repeatibility should be possible in the 20 milliseconds of run time available in a Hotshot tunnel. In Reference F-17 it was found convenient during the exploratory stages to use an 18 μ-second ramp-shaped voltage-pulse in order to reduce the amount of hunting required to determine the breakdown voltage.

Another possibility for obtaining spark breakdown during a short time interval would be to use a probe geometry which would offer a range of possible sparking conditions for a given field configuration. The location or length of the spark produced by such a geometry might then be used to indicate gas density. An example of this would be a number of probes at various potentials grouped around a central grounded probe. Determination of the firing sequence of the sparks could give V_s. But it is probable that no arrangement could be devised which would eliminate interaction between the probes, and the firing of one would trigger others at lower potentials. Another example would be an electrode with a continuous range of local surface curvature, thus providing a range of local variations in E. Here again the spark location could vary with density.

Still another example of this approach which was tested for feasibility consisted of two electrodes set at an angle with respect to one another. In this way E and d varied along the length of the electrode, presumably providing a continuous range of possible sparking conditions. Figure F-6 shows the device tested. The density range was from 10^{-4} to 2×10^{-2} atmospheres, the gap width varied from 1/2" to 3" and the voltage ranged up to 1200 volts.

Briefly, it was found that spark length and location was not repeatable but seemed quite random. Worse, in many instances there seemed to be multiple sparks. Thus it appears that this probe geometry offers a multiple set of E and d combinations with equal spark probabilities or that the initial breakdown triggers other sparks. Interestingly enough, despite the random location and length of the spark, the plot of breakdown voltage vs. density gave a smooth Paschen-shaped curve. This gives evidence that the random spark location and length is due more to a triggering mechanism than to any peculiarities of the geometry or electrode surface conditions.

Tests of probes based on the Townsend discharge were not conducted due to the lack of a suitably sensitive ammeter ($\sim 10^{-13} - 10^{-7}$ amperes). Detailed information is given in Reference F-9 on the experimental difficulties in measuring Townsend discharge characteristics and on techniques for obviating them. This information, along with the detailed presentation of the underlying physical mechanisms also given, should provide a very useful base for the practical application of the Townsend discharge to experimental gas dynamics.

In connection with an experiment conducted for other purposes it was noted in passing that the radio frequency discharge shows considerable sensitivity to gas density. The use of an electrodeless ring discharge would be attractive for diagnostics since it eliminates electrode surface effects. No quantitative measurements of the effects of density on the electrodeless ring discharge were made, however. It seems likely that some difficulty would be involved in designing a probe to give sufficiently localized measurements.

The simplicity of the equipment required for the glow discharge allowed a more extensive investigation of its possible use for the measurement of ρ. Figure F-7 shows the schematic of the circuit employed. Batteries were used to allow isolation of the power circuit from ground because it was found that in the evacuated test section of the Hotshot tunnel a glow discharge to the grounded metal walls would otherwise occur. The ideal power supply for DC gaseous discharge work is in most cases the constant current source, since discharge voltage is a single-valued function of current. Thus the external circuit should ideally be equivalent to a high-voltage battery in series with a high resistance. The resistance is often referred to as ballast. The variable resistor shown in Figure F-7 serves as ballast resistor. The potentiometer is for voltage control. The switch shown is connected such that the glow current can, if necessary, be measured without having the voltmeter in parallel with the high-impedance glow.

Figure F-8 shows the same circuit with the oscilloscope connections used for obtaining voltage-current characteristics. Figure F-9 shows some of the probe

configurations tested. These ranged from a bona-fide large-surfaced glow probe to a pointed-electrode corona probe. Differences among the probes were due chiefly to differences in cathode geometry. The cathodes with larger areas had larger ranges of "normal" discharge current of course, since abnormal glow begins only when the cathode is covered with the glow, and in general they also gave more stable and repeatable results. Figure F-10 shows the experimental setup. Figure F-3 gives typical data obtained with the corona probe for densities in the Hotshot range using the oscilloscope connected as shown in Figure F-8.

Many practical problems were encountered in the work on the glow probe. One of the most dogging of these was what appeared to be a tendency for the glow to spread from the desired areas. Since only DC instruments were being used initially, the occurrence of this phenomenon seemed quite random. Thus under some conditions the insulated portions of the probe would glow, no matter what the insulation: epoxy, glass, corona dope, or rubber; and this was found to occur on the insulated portions of either or both electrodes depending somewhat on the cleanliness of the conducting electrode surface. Very little effect was noted of diffusion barriers, although completely enclosing both electrode faces together in plastic tubing was effective. It was felt that the discharge could not be corona: there was no evidence of insulation breakdown which would allow DC conduction, the characteristic tufts did not appear along the cathode, and no glow at all occurred when there were no exposed conducting surfaces (and thus no current in the probe circuit).

It is now felt that the observations made of the glow appearing on insulated conductors point conclusively to a high-frequency glow appearing with, and caused by, the intermittent discharge—observed with the oscilloscope—which occurred at particular combinations of external-circuit and glow parameters (see below). This phenomenon can undoubtedly be eliminated for a given range of pressures and probe geometry by the proper changes in external circuitry.

Much of the data was found to follow an equation of the following form, as given for example in Reference F-5:

$$V_c = k_1 + k_2 \frac{\sqrt{I}}{\rho}$$

where k_1, k_2 = constants

This indicates a density sensitivity $(dI/I)/(d\rho/\rho)$ of 0.5. This agrees with that found by Werner (Reference F-14) who also found a velocity sensitivity 25 times lower.

In order to test the response time of the glow discharge, the cathode-ray oscilloscope was set up (Figure F-8) to measure glow current and voltage. Two attempts were made to measure the time of response to rapid fluctuations in density. The first attempt to do this was by use of the shock wave from a spark discharge between a pair of electrodes located across the chamber from the glow electrode. The spark produced appeared quite cylindrical and caused a sharp noise even under vacuum. Unfortunately it also produced excessive electromagnetic noise which was picked up by the glow circuitry, completely masking the glow pressure-response. Another method for producing a rapid pressure fluctuation was the puncturing of a cellophane diaphragm separating a small volume of atmospheric air from the evacuated chamber. Figure F-11 illustrates the results obtained. It can be seen that the chamber pressure stabilizes at a higher value within about four milliseconds. The probe appears to pick up much faster pressure variations resulting from the reflections of the shock wave configuration. This would be in agreement with the results in References F-14 and F-31 indicating that the glow would pick up pressure fluctuations of frequencies in the megacycle and 200-cycle regimes respectively. It appears that the time response of the glow probe is quite adequate.

Some interesting observations were made with the oscilloscope, of saw-tooth fluctuations in glow current. Oscillations of the type observed are well known, having been first noted by Gassiot in 1863 (see Reference F-5, p. 187). Their

occurrence and the frequency of intermittence depend on the EMF, resistance, and capacitance of the external circuit as well as the breakdown voltage, extinction voltage, and effective capacitance of the glow which in turn depend on the gas properties and the frequency itself. The oscillations are readily understood in terms of the charging and discharging of the effective parallel capacitance (including electrode and space-charge capacitance) through the negative characteristic of the subnormal glow, but other explanations have been proposed. In any case the feature of the glow which is essential to the oscillations is that the extinction voltage is lower than the breakdown voltage. Here of course it is the dynamic rather than the static glow characteristic which governs. Considerable analytical and experimental work has been done relating the frequency to the discharge and circuit parameters. For a full discussion, equations, and references, see Reference F-5. The intermittant response was observed at higher and lower pressures but not at intermediate pressures. In the range where the saw-tooth occurred, the frequency varied with density, and correlated with the visual appearances of the discharge at the anode and cathode. For a given external circuit, upon lowering the pressure to the point where the glow begins, a hissing sound is generated and the oscilloscope shows saw-tooth oscillations in current at frequencies around 10 KCPS. The occurrence of the saw-tooth coincides with the appearance of an apparently steady orange light in the shape of a cone with its apex at the anode. Lowering the pressure gradually, increases the frequency of the saw-tooth until it and the cone suddenly disappear. Then the pressure goes through a range where the current is steady, until a point is reached where further lowering brings back the saw-tooth fluctuation, this time at high frequency, along with a diffuse reddish cone at the anode. Lowering the pressure further, decreases the oscillation frequency until the glow collapses.

It seems probable that the anode cone mentioned above was caused by one or more of the breakdown threshold mechanisms (Reference F-10, p. 506) in which an electron in a concentrated field region near the anode initiates an avalanche, from

which the electrons quickly diffuse leaving a positive space charge and enhanced field at the anode, and from which ionizing photons are emitted. With a highly stressed anode, breakdown thus occurs at the anode first and there is a range of voltage between breakdown at the anode and breakdown in the gap. When the glow is in intermittent operation this corona burst occurs at the anode each cycle and is visible. In continuous operation the breakdown mechanisms are no longer in operation and the anode cone does not appear. The fact that the anode cone and oscillations were observed over a lower range of densities (below that corresponding to the minimum in the Paschen curve) and a higher range of densities (above the Paschen minimum) was due to the particular combination used of voltage-current characteristic for the external circuit with the discharge characteristics at the various pressures. The fact that at low densities the frequency increased with density was because below the Paschen-minimum density, increasing the density decreases the breakdown voltage to which the circuit capacitance must be charged each cycle. This also explains the observed decrease in frequency with increasing density above the Paschen minimum since here breakdown voltage increases with density.

In concluding the outline of the feasibility tests, it should be emphasized that no consideration has been given in these tests of the effect on discharge characteristics of the chemical composition of the gas. It has been shown that in the glow discharge, for example, the effects of minute concentrations of some gases can have an overwhelming effect on the glow characteristic—see Reference F-5, p. 181. (In fact the electric discharge is so sensitive to gas composition that it suggests itself for possible use in chemical analysis of the flow.) The effect of density or velocity changes can be overshadowed by the effect of changes in the gas composition. This is a particularly serious problem in view of the flow contamination common to Hotshot facilities. With known composition, as was the case for the literature cited above, the important unknowns reduce to two: velocity and density.

Two approaches to the solution of the problem presented by the effects of chemical contamination are, first, to seed the gas with an element of low enough ionization potential or whatever to override the effects of any additional contaminants, thus providing effectively known chemical composition, or, second, to use some independent means of determining the chemical composition of the flow.

RECOMMENDATIONS FOR FURTHER WORK

1. The Townsend discharge probe should be studied experimentally to isolate density and velocity effects. The absence of a velocity effect might be inferred from the results in References F-1 and F-17, which show spark breakdown voltage to be independent of velocity. On the other hand Fucks found a velocity sensitivity of .5 to 1.0.

2. The variable-geometry spark discharge probe should be studied theoretically to determine its possibilities. Of particular importance is the question of providing a single-valued geometry which produces repeatable single-spark breakdown data.

3. The electrodeless ring discharge should be investigated experimentally as a possible in-flight spectroscopic source and to determine its sensitivity to flow parameters. This device offers an opportunity for reducing or eliminating electrode effects.

4. A glow discharge theory should be developed which includes the effects of convection. The work of Badareu and Popescu provides a good basis for this extension of theory. One approach would be to make some assumption as to the average effect of convection on the motion of the ions and from this obtain a relation for the charge distribution in the dark space. This along with Poisson's equation could be used to obtain the desired characteristic equation. Any equation would of course require experimental verification; the data of Reference 16 provides a possible experimental check of the theory.

5. Calibration tests should be made to measure the effect of velocity and electromagnetic noise on the corona probe and to explore the effects of chemical composition. These tests could be conducted for example with three experimental set ups:

a. Vacuum Contamination Chamber. This setup allows variation of gas density, chemical composition (and with it ionization potential, etc.), probe geometry, and electric circuitry.

b. Shock Tube. This setup allows isolation of the effects of velocity, density, and chemical composition, as well as providing data on time response.

c. Hotshot Tunnel. Although the variation of parameters in this facility is much more complex and, unlike the shock tube, not calculable from theory, it should be possible nevertheless to obtain valuable data by comparison of runs made with different gases, charge densities, power inputs, etc., placing weighted reliance on other measurements made during these runs such as composition, pressures, velocity, etc.

6. The use of rail electrodes for the direct measurement of velocity by observation of the motion of an intermittent glow discharge should be investigated experimentally. Maier's work (Reference F-28) indicates that the intermittent glow travels at free-stream velocity. The frequency of the intermittent discharge would be sensitive to density. It is thus conceivable that and intermittent-glow probe would provide data on velocity, density and mass flux.

REFERENCES

F-1. Marlotte and Demetriades, "Electrical Discharges in Hypersonic Flows," Physics of Fluids, Vol. 3, No. 6, Nov., 1960.

F-2. Cobine, J. D., Gaseous Conductors, Dover Publications, Inc., New York, 1941.

F-3. Darrow, K. K., Electrical Phenomena in Gases, William and Wilkins Co., 1932.

F-4. Fowler, R. G., "Radiation from Low Pressure Discharges," Handbuch der Physik, Vol. XXII, p. 209, 1956.

F-5. Francis, Gordon, The Glow Discharge at Low Pressure," Handbuch der Physik, Vol. XXII, p. 53, 1956.

F-6. Engel, A. von, Ionized Gases, Clarendon, Oxford, 1955.

F-7. Handbuch der Physik, Vol. XXII, Springer-Velag, Berlin, 1956.

F-8. Finkelnburg, W., and Maecker, H., Electric Arcs and Thermal Plasma, translation ARL 62-302, OAR, USAF, Wright Field, Ohio, Jan. 1962.

F-9. Loeb, L. B., Basic Processes of Gaseous Electronics, University of California Press, Berkeley, 1955.

F-10. Loeb, L. B., "Electrical Breakdown of Gases with Steady or Direct Current Impulse Potentials," Handbuch der Physik, Vol. XXII, p. 445, 1956.

F-11. Maxfield, F. A., and Benedict, R. R., Theory of Gaseous Conduction and Electronics, McGraw-Hill, New York, 1941.

F-12. High Speed Aerodynamics and Jet Propulsion, Vol. IX, "Physical Measurements in Gas Dynamics and Combustion," Princeton University Press, Princeton, N. J., 1954.

F-13. Fucks, W., "Investigation of the Operating Properties of the Leakage Current Anemometer," translation from Deutsche Luftfahrtforschung, 1944, NACA Tech. Mem. 1178, 1947.

F-14. Werner, F. D., An Investigation of the Possible Use of the Glow Discharge in Transverse Air Streams, Ph. D. Thesis, California Institute of Technology, 1949.

F-15. Fucks, W., "Gas Discharges Applied to Measurement," Appl. Sci. Res., B, Vol. 5, No. 1-4, p. 167, 1955.

F-16. Marlotte, G. L., An Experimental Investigation of the Effect of a Transverse Hypersonic Flow Velocity upon a Low-Density DC Electrical Discharge in Air, Galcit Hypersonic Research Report No. 66, California Institute of Technology, June 15, 1962.

F-17. Sharbaugh, A. H., Watson, P. K., White, P. R., Lee, T. H., and Greenwood, A., "An Investigation of the Breakdown Strength of Nitrogen at High Temperatures with use of a Shock Tube," Paper 61-136, Power Apparatus and Systems, AIEE, June, 1961.

F-18. Werner, F. D., "An Investigation of the Possible use of the Glow Discharge as a Means for Measuring Air Flow Characteristics," Rev. Sci. Inst., Vol. 21, No. 1, Jan. 1950.

F-19. Romig, Mary, "Steady State Solutions of the Radiofrequency Discharge with Flow," Physics of Fluids, Vol. 3, No. 1, Jan. 1960.

F-20. Strauss, H. J., "Untersuchungen uber den Existenzbereich der electrodenlosen Ringentladung," Ann. Phys., 7 Folge, Band 1, 1958.

F-21. Schluter, H., "Untersuchungen an einer Hochfrequenzapparatur mit statischem Magnetfield," Z. Naturforsch, Vol. 15a, No. 3, p. 281, Mar. 1960.

F-22. Salmon, Jean, "Theorie de la Decharge Haute Frequence dans les Gaz aux Faibles Pressions. Etude Experimentale des Sources D'ions du Type Haute Frequence," Ann. Phys.(Paris), Vol. 2, No. 11, p. 827, 1957.

F-23. Chenot, M., "Production de Courant Continu per une Decharge en Haute Frequence II," Journal de Physique et le Raduim, Vol. 18, p. 395, June, 1957.

F-24. Salmon, Jean, "Theorie de la Decharge H. F. aux Faibles Pressions," Appl. Sci. Res., B, Vol. 5, No. 1-4, p. 131, 1955.

F-25. Brasefield, C. G., "High Frequency Discharges in Mercury, Helium, and Neon," Phys. Rev., Vol. 37, p. 82, Jan. 1931.

F-26. Brown, S. C., "Breakdown in Gases: Alternating and High-Frequency Fields," Handbuch der Physik, Vol. XXII, p. 531, 1956.

F-27. Badareu, Eugen, and Popescu, Iovitzu, "Some Problems Regarding the Phenomena Occurring at the Cathode of the Glow Discharge," Rev. de Physique (Bucarest), Vol. 5, No. 1, p. 41, 1960.

F-28. Maier, Eugen, "Die Glimmentladung im Gasstrom hoher Geschwindigkeit," Z. Phys., Vol. 93, No. 1-2, p. 65, 1934.

F-29. Oertel, von H., "Knallwellenoszillographie mittels Koronasonde," Zeitschrift fur angewandte Physik, Vol. 4, No. 5, p. 177, 1952.

F-30. Jones, F. L., "Ionization Growth and Breakdown," Handbuch der Physik, Vol. XXII, p. 1, 1956.

F-31. Lindvall, F. C., "A Glow Discharge Anemometer," Electrical Engineering, p. 1068, July, 1934.

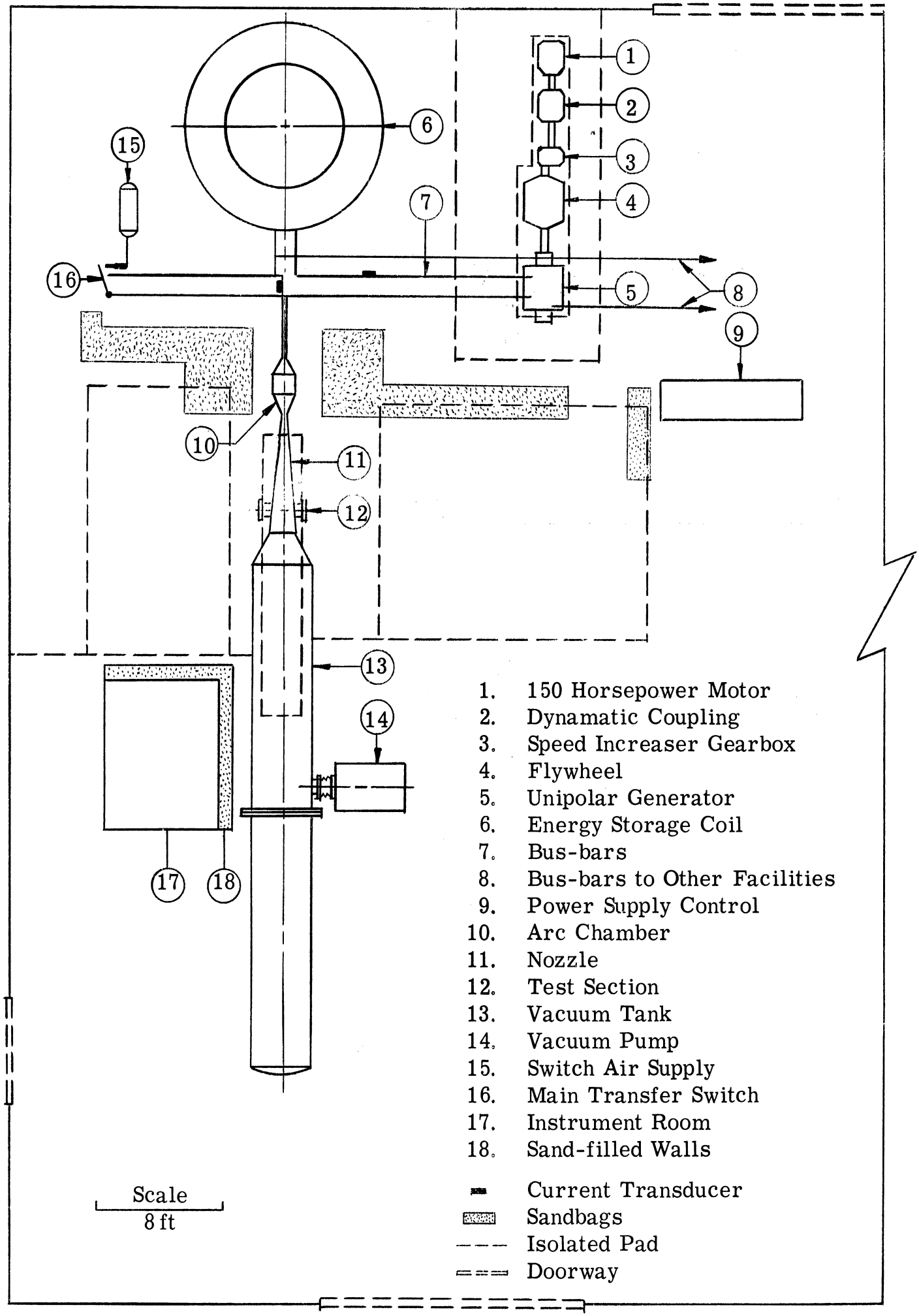

Figure 1. Laboratory Layout

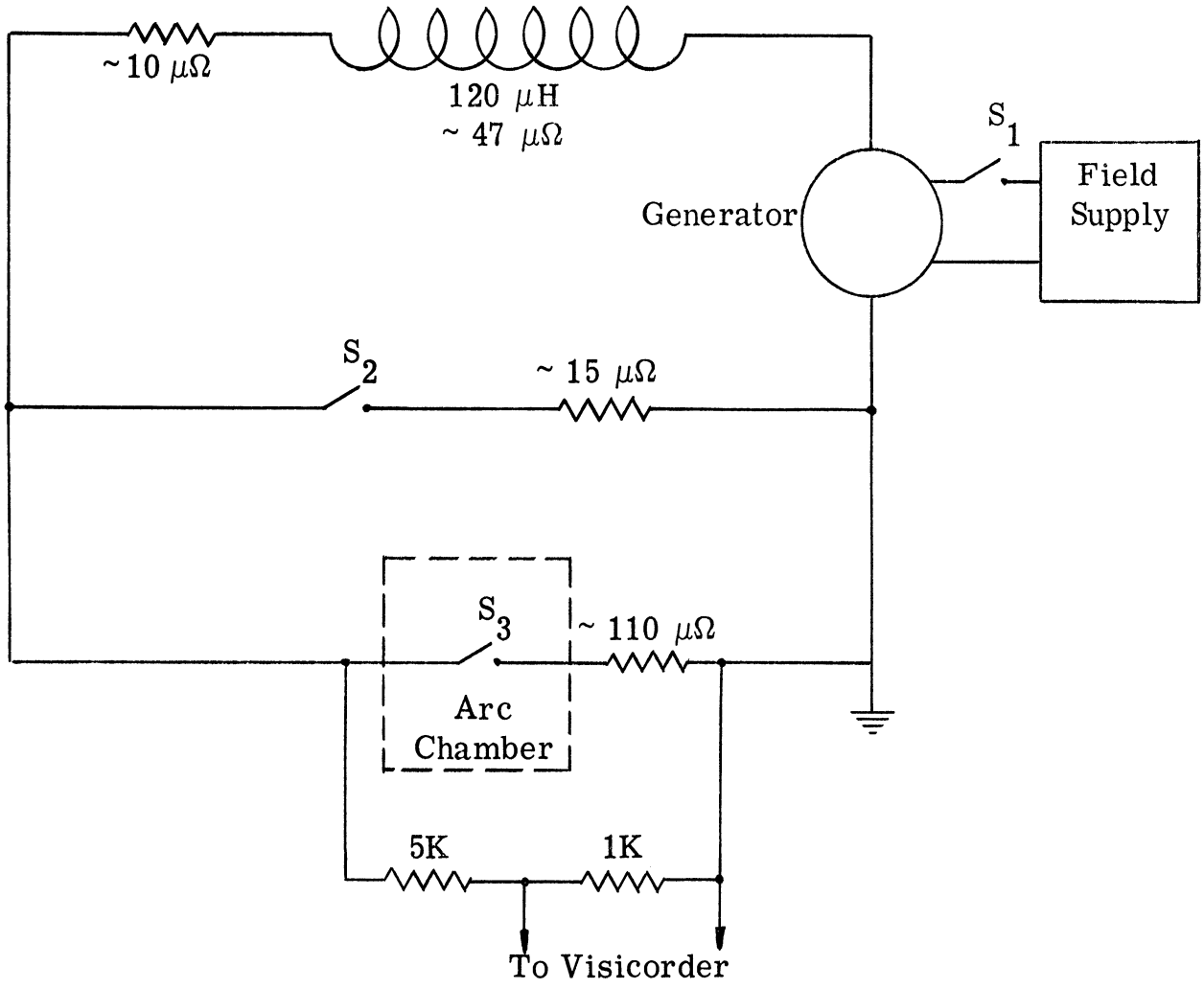

Figure 2. Energy Supply Schematic

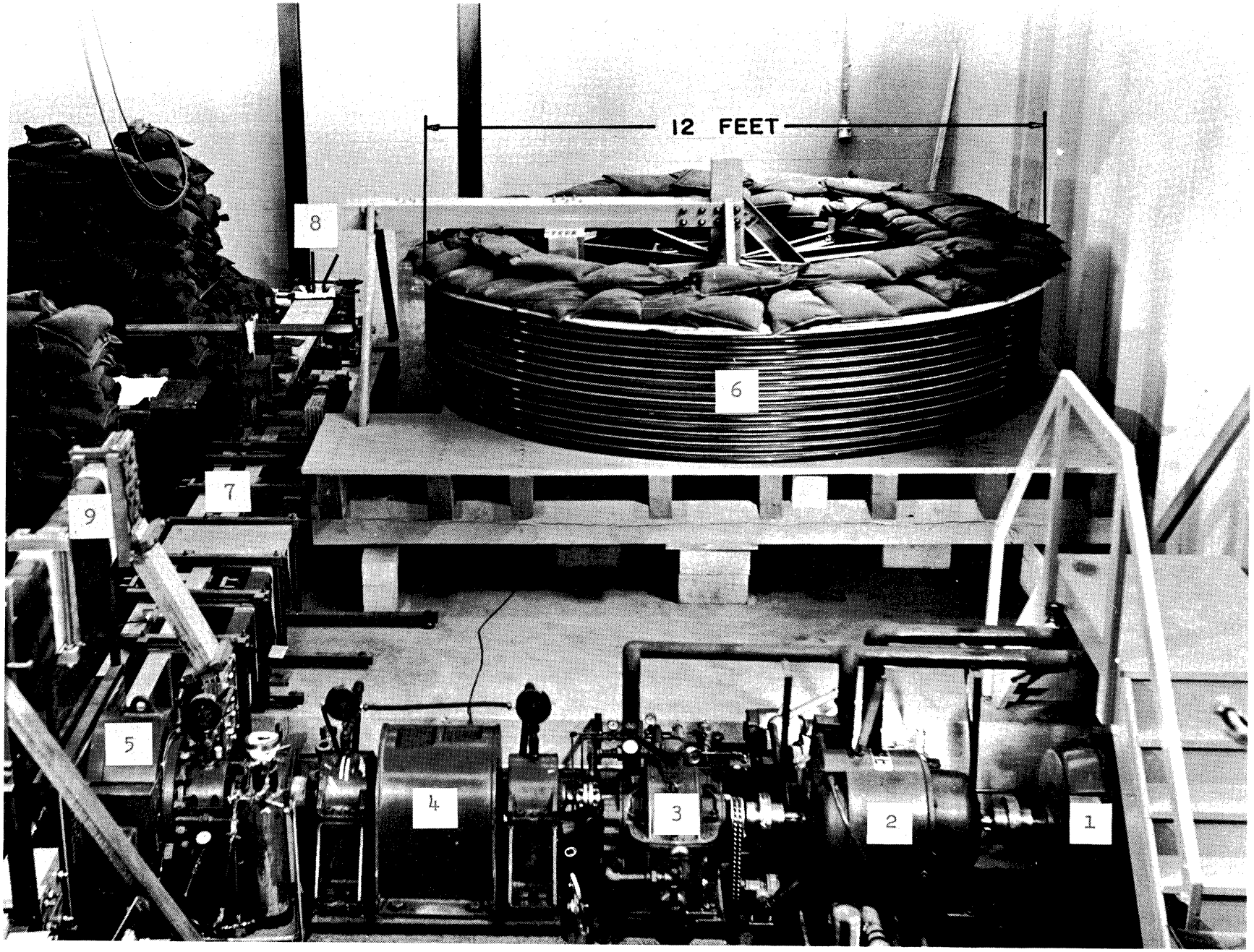
12 FEET
1
2
3
4
5
6
7
8
9

Figure 3. Photograph of Power Supply and Coil Circuit

(See facing page.)

Legend for Figure 3

1. 150 Horsepower Motor
2. Dynamatic Eddy-Current Coupling
3. Speed Increaser Gearbox
4. Flywheel
5. Unipolar Generator
6. Energy Storage Coil
7. Buss-bars
8. External Electrodes
9. Buss-bars to Other Facilities

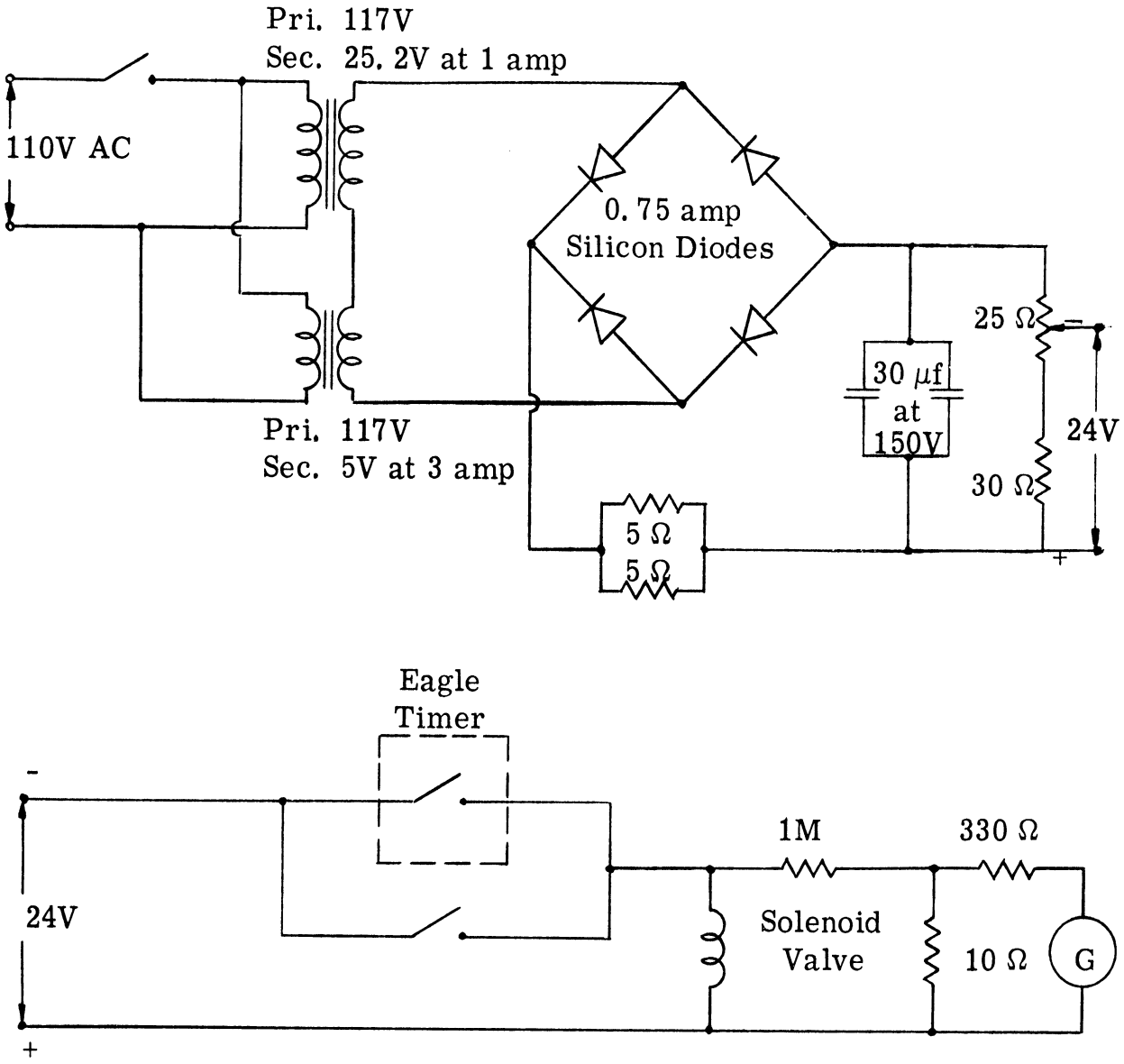

Figure 4. 24 Volt Power Supply for Main Transfer Switch Solenoid

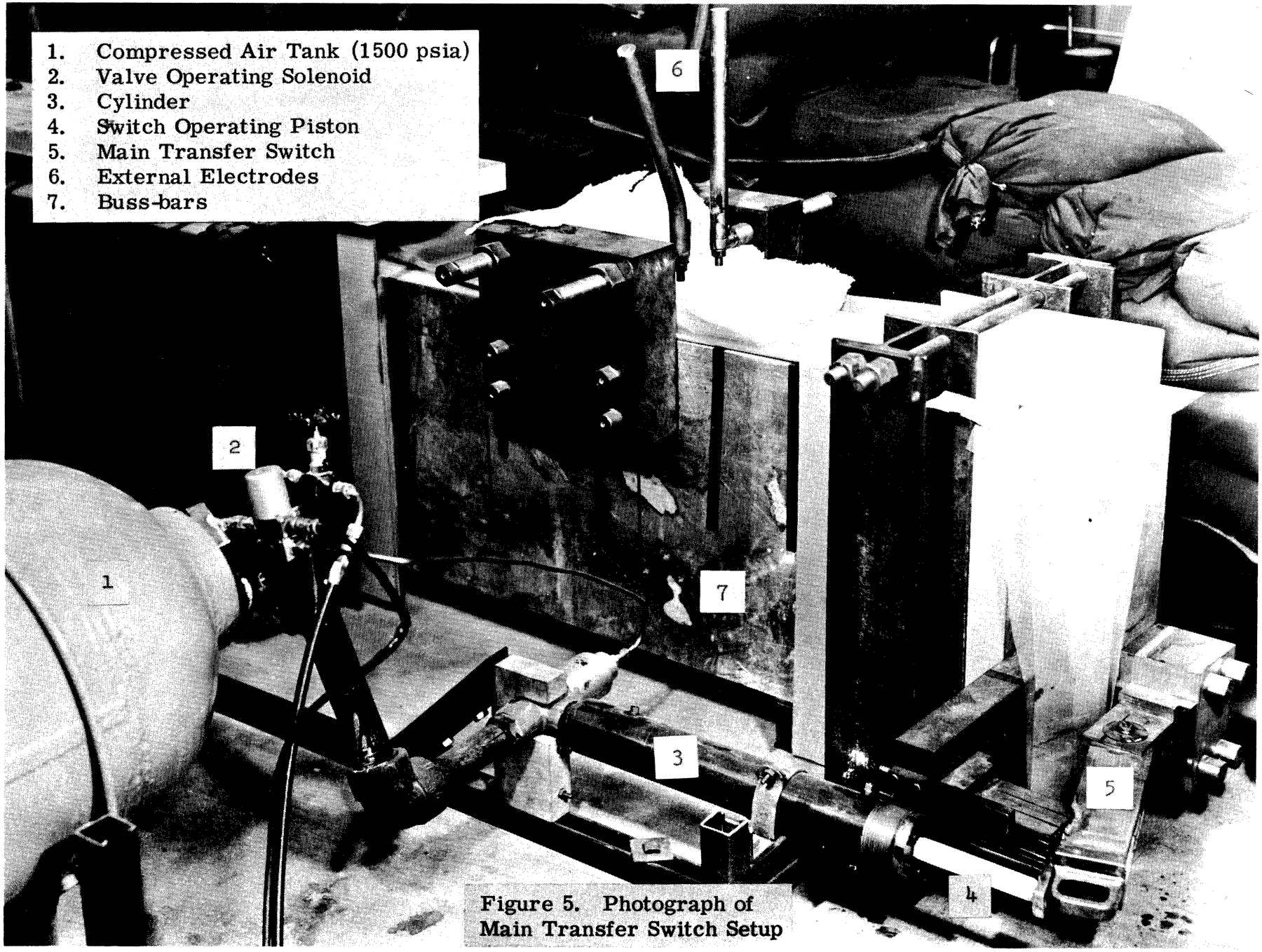

Figure 5. Photograph of Main Transfer Switch Setup

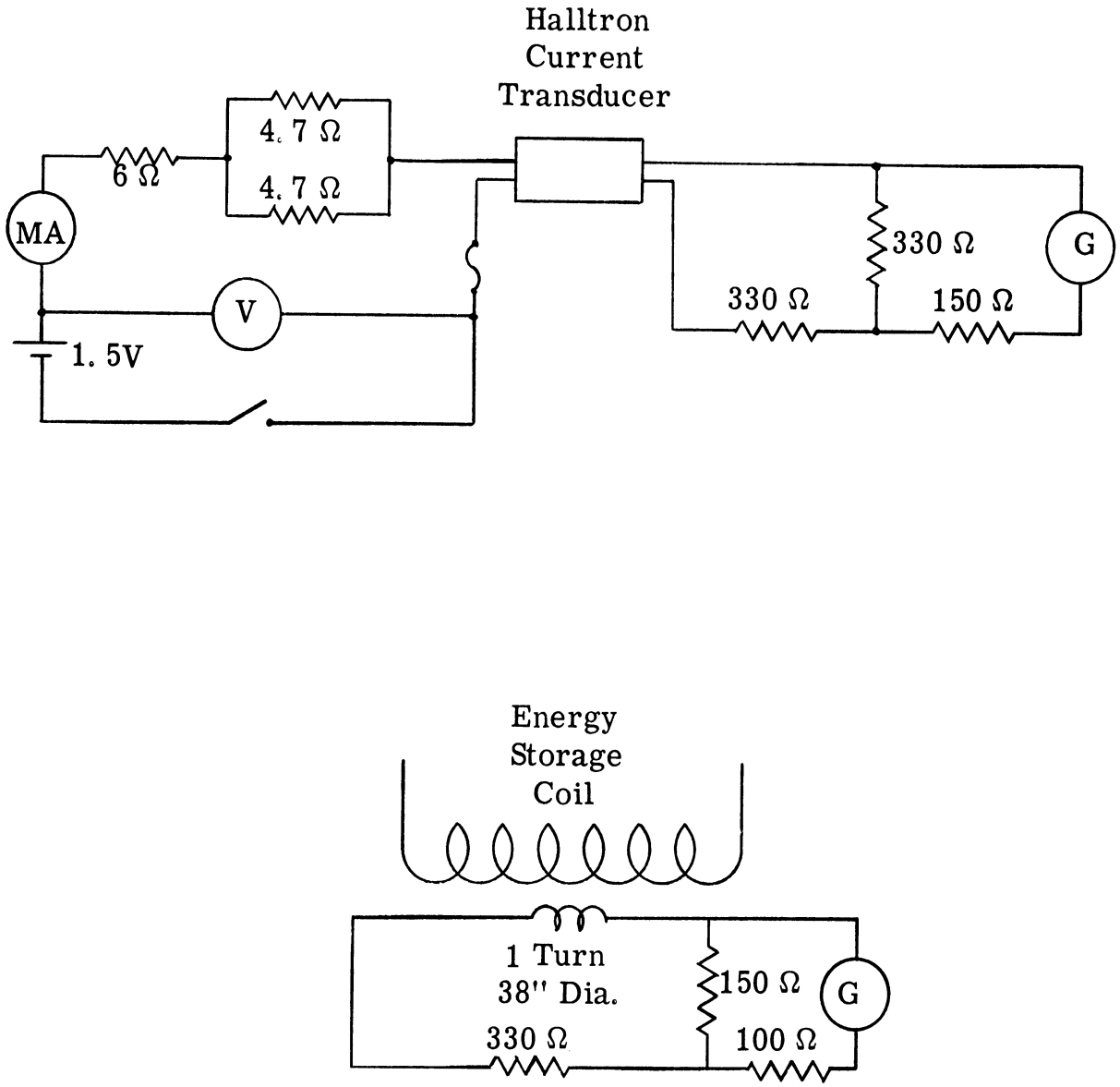

Figure 6. Halltron Current Transducer Circuit and Arc Voltage Indicator Circuit

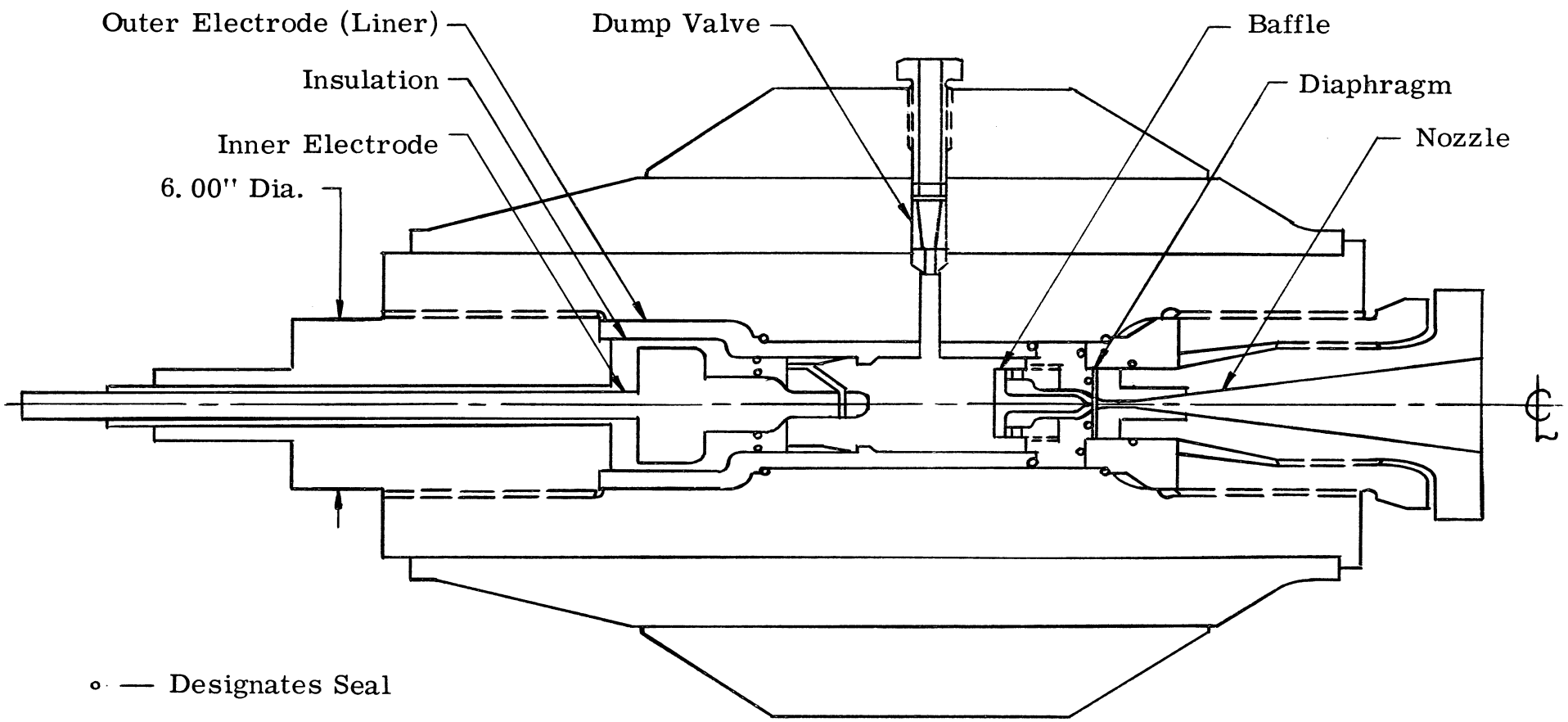

Figure 7. Sketch of the Arc Chamber Assembly

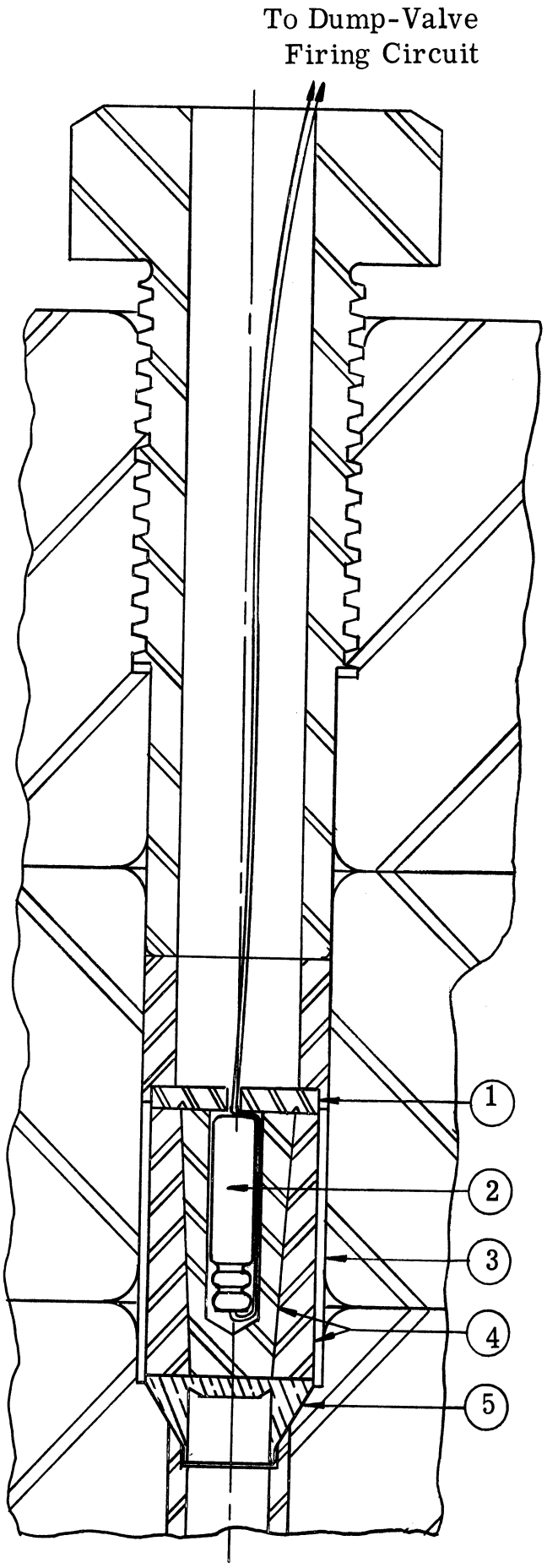

1. Upper Diaphragm (4340 R_c 30 Steel)
2. No. 6 Electric Blasting Cap
3. 1/16 in. Paper Wrapping
4. Dump Valve Assembly (4340 R_c 30 Steel)
5. Lower Diaphragm (Exposed to Chamber Gas)

Figure 8. Dump Valve Configuration

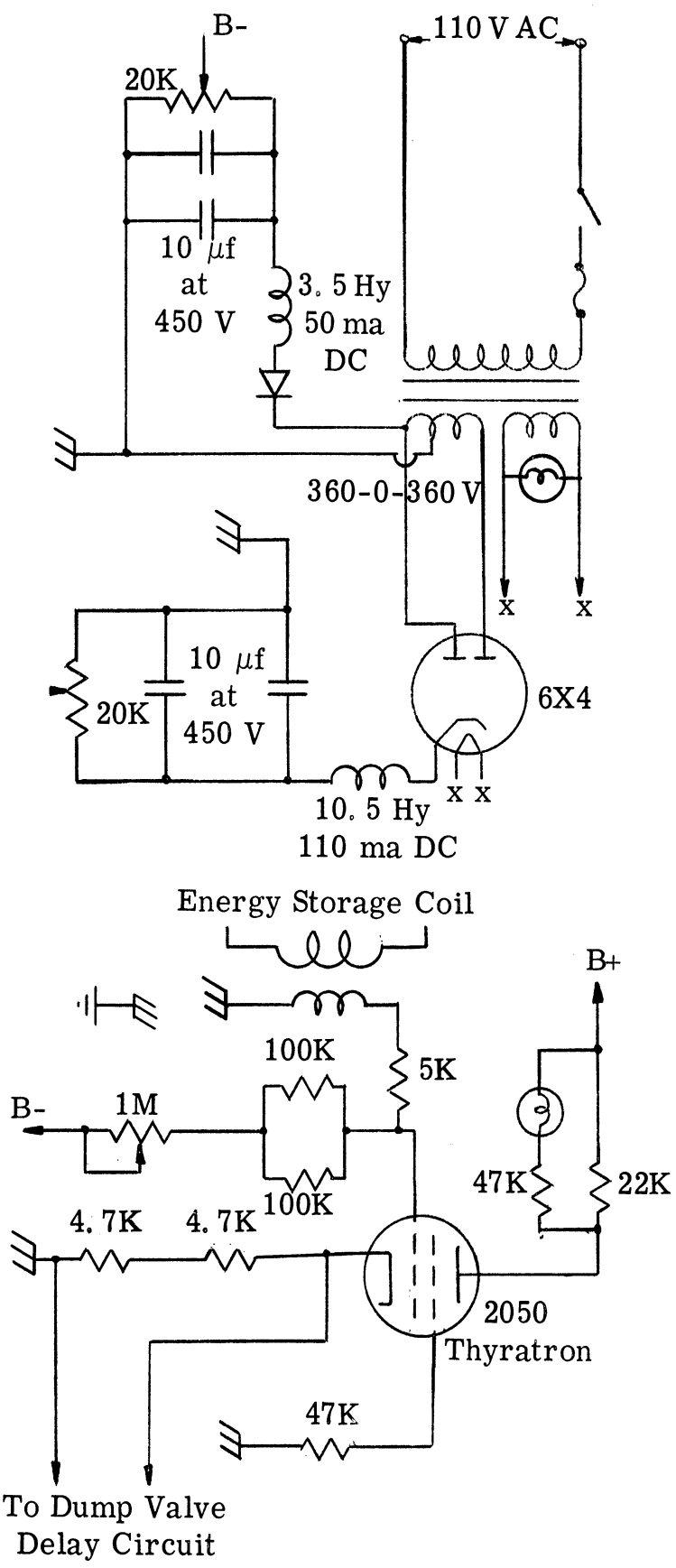

Figure 9. Dump Valve Triggering Circuit

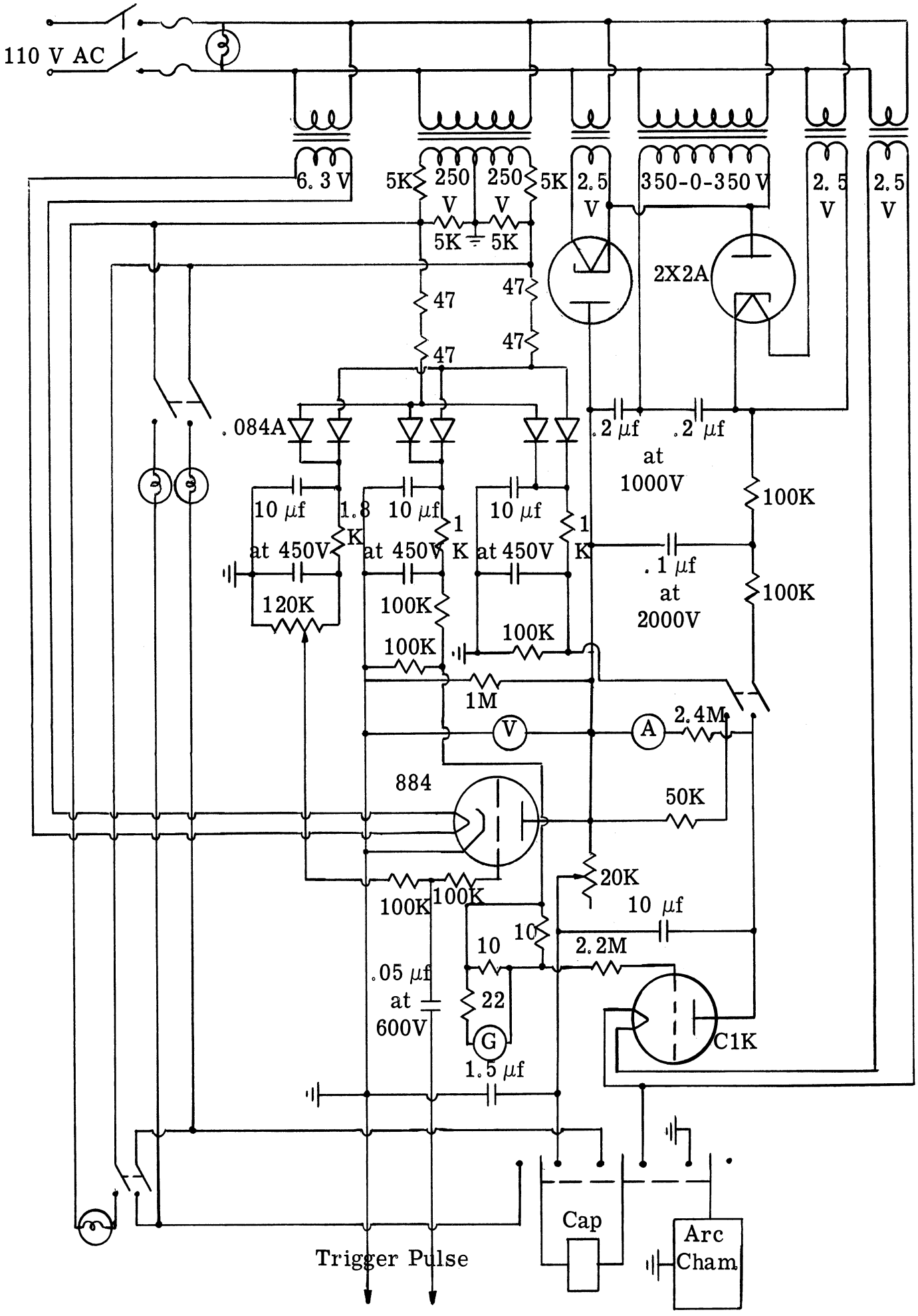

Figure 10. Dump Valve Delay Circuit

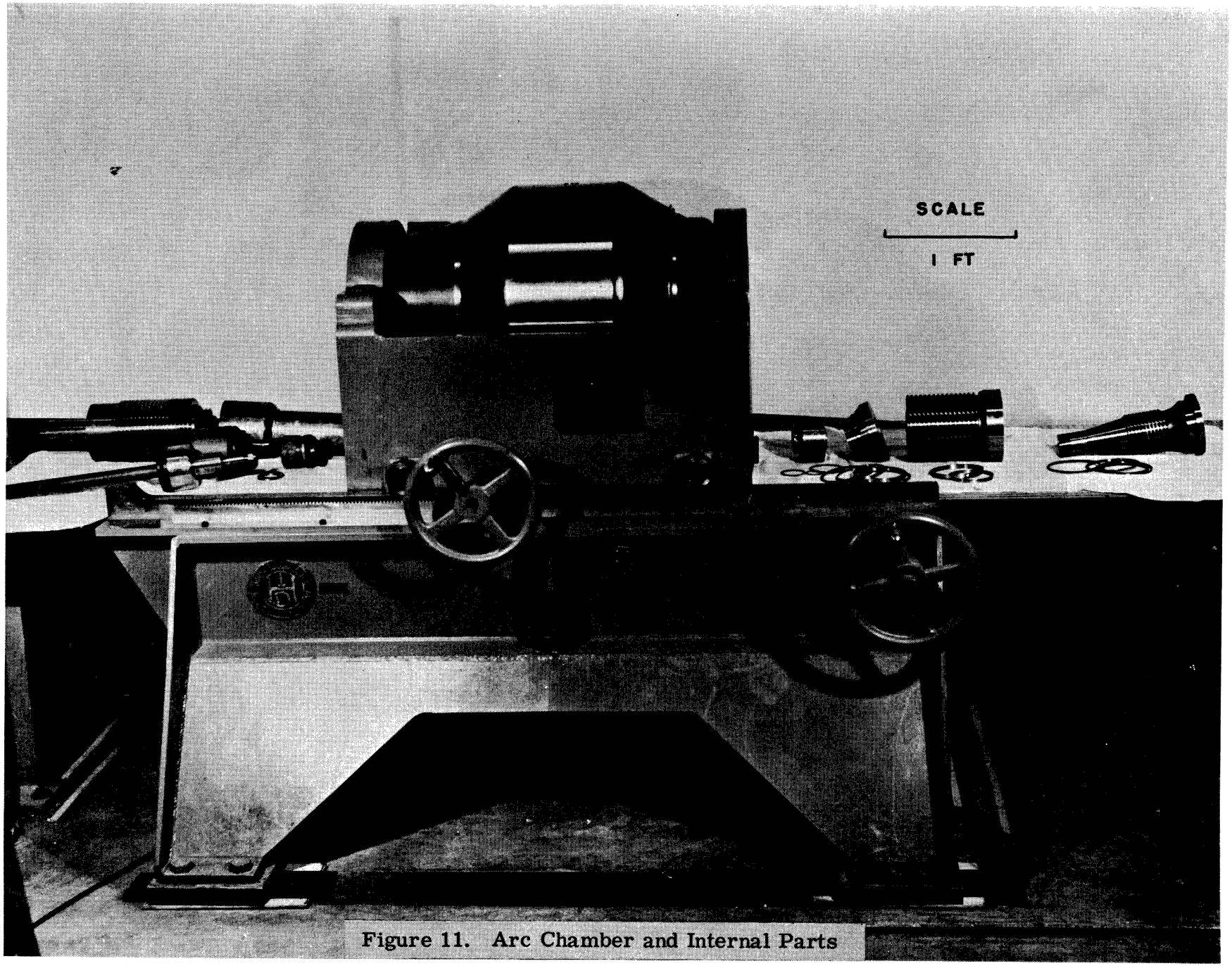

Figure 11. Arc Chamber and Internal Parts

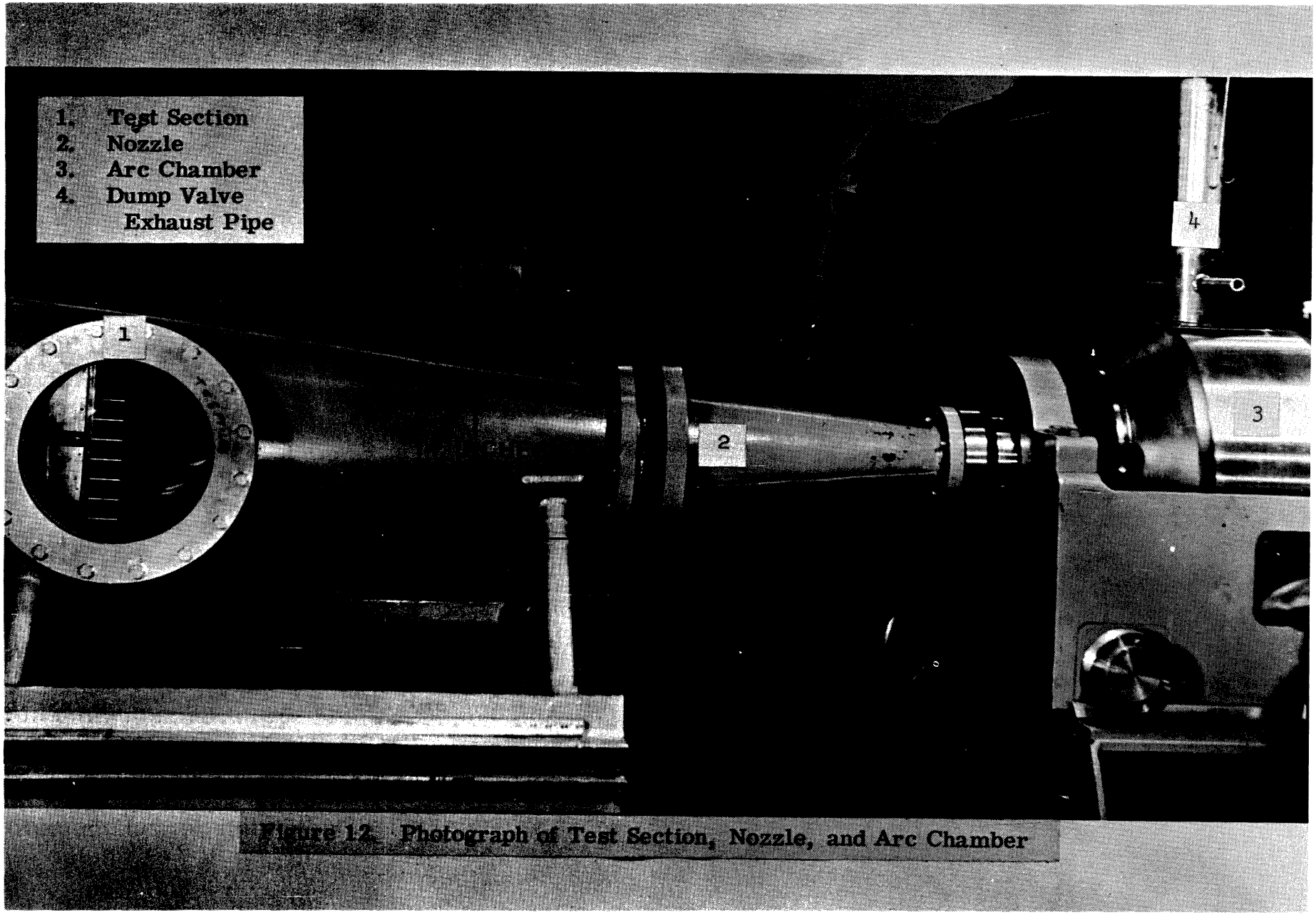

Figure 12. Photograph of Test Section, Nozzle, and Arc Chamber

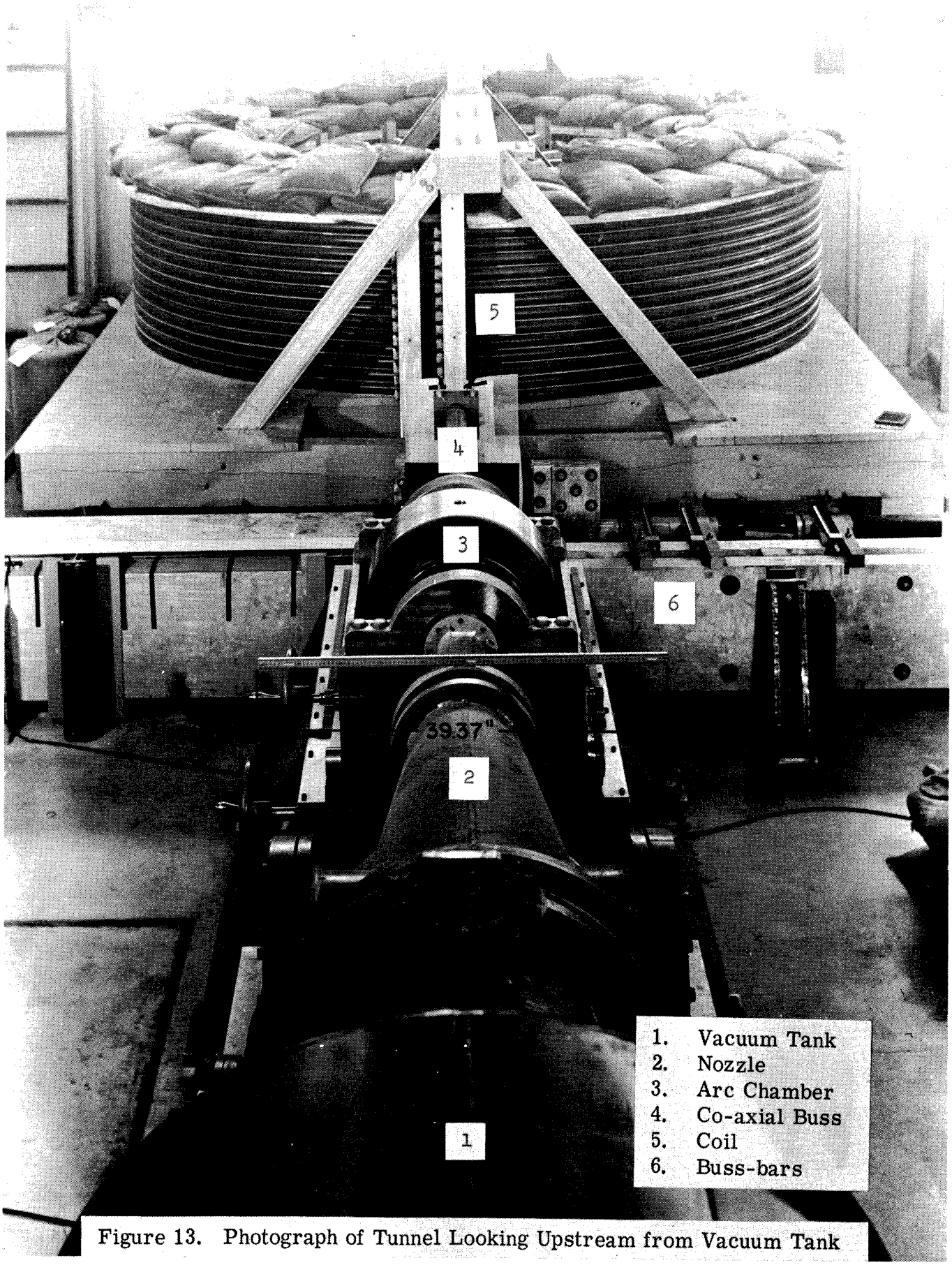

Figure 13. Photograph of Tunnel Looking Upstream from Vacuum Tank

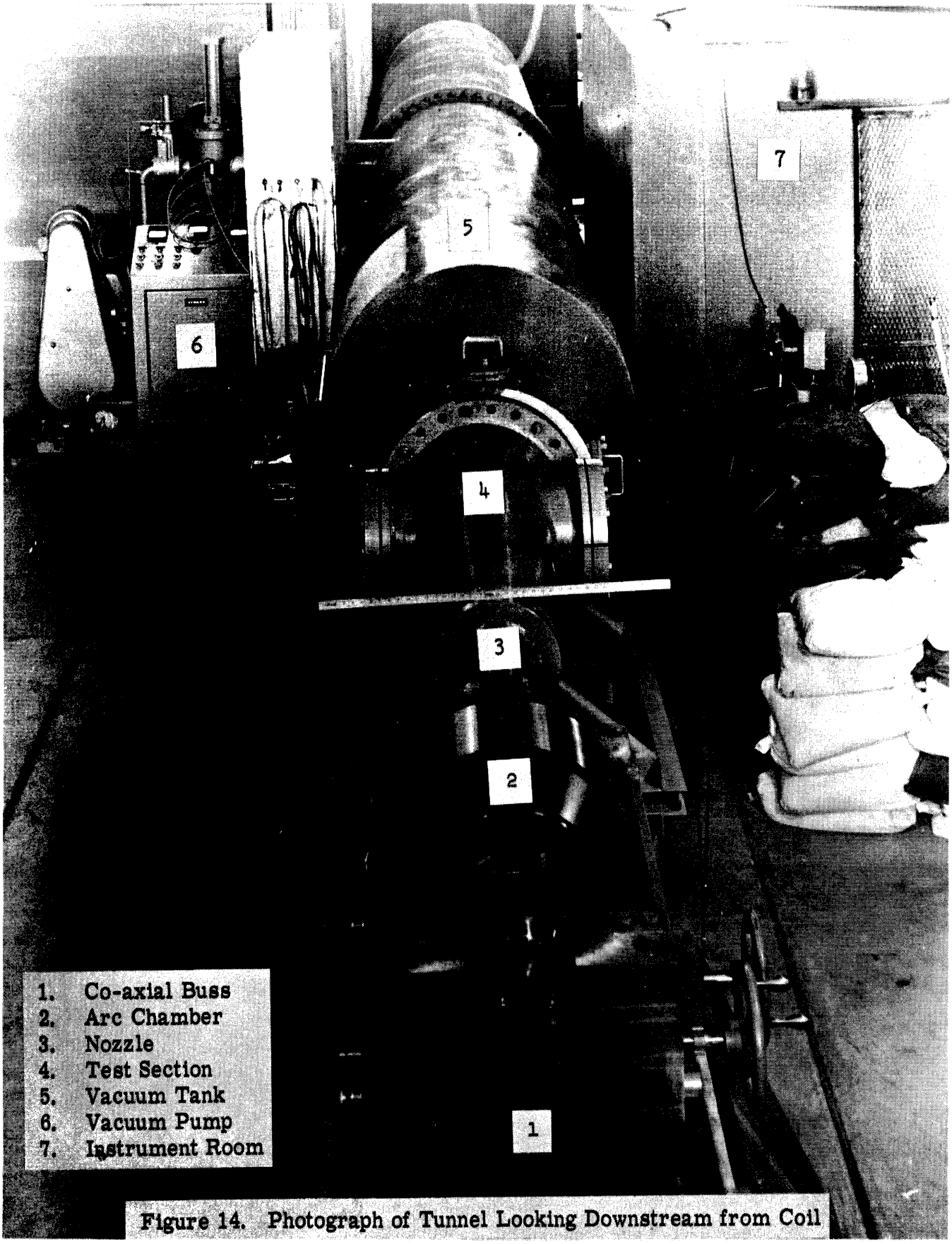

Figure 14. Photograph of Tunnel Looking Downstream from Coil

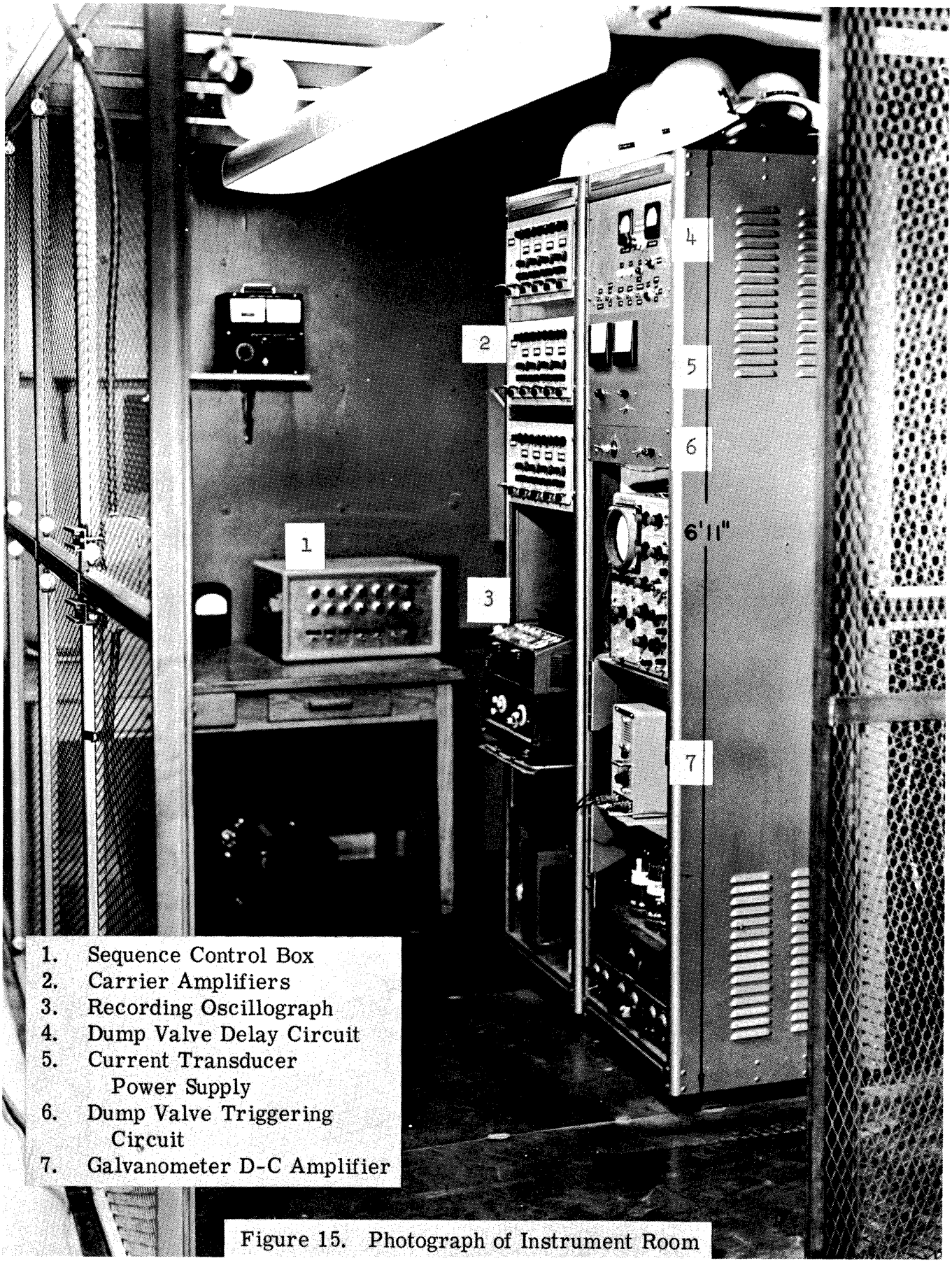

1. Sequence Control Box
2. Carrier Amplifiers
3. Recording Oscillograph
4. Dump Valve Delay Circuit
5. Current Transducer Power Supply
6. Dump Valve Triggering Circuit
7. Galvanometer D-C Amplifier

Figure 15. Photograph of Instrument Room

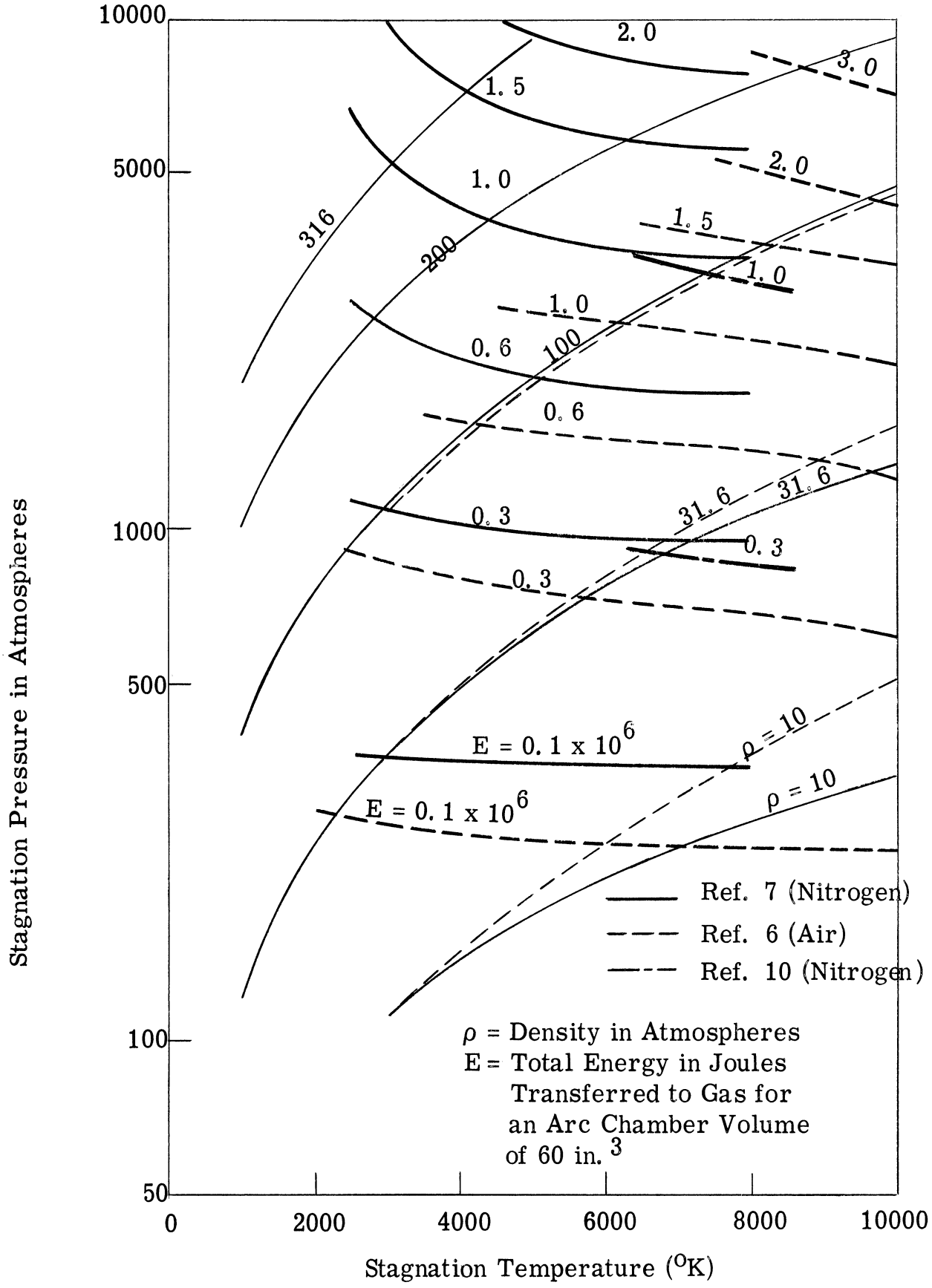

Figure 16. Arc Chamber Stagnation Conditions

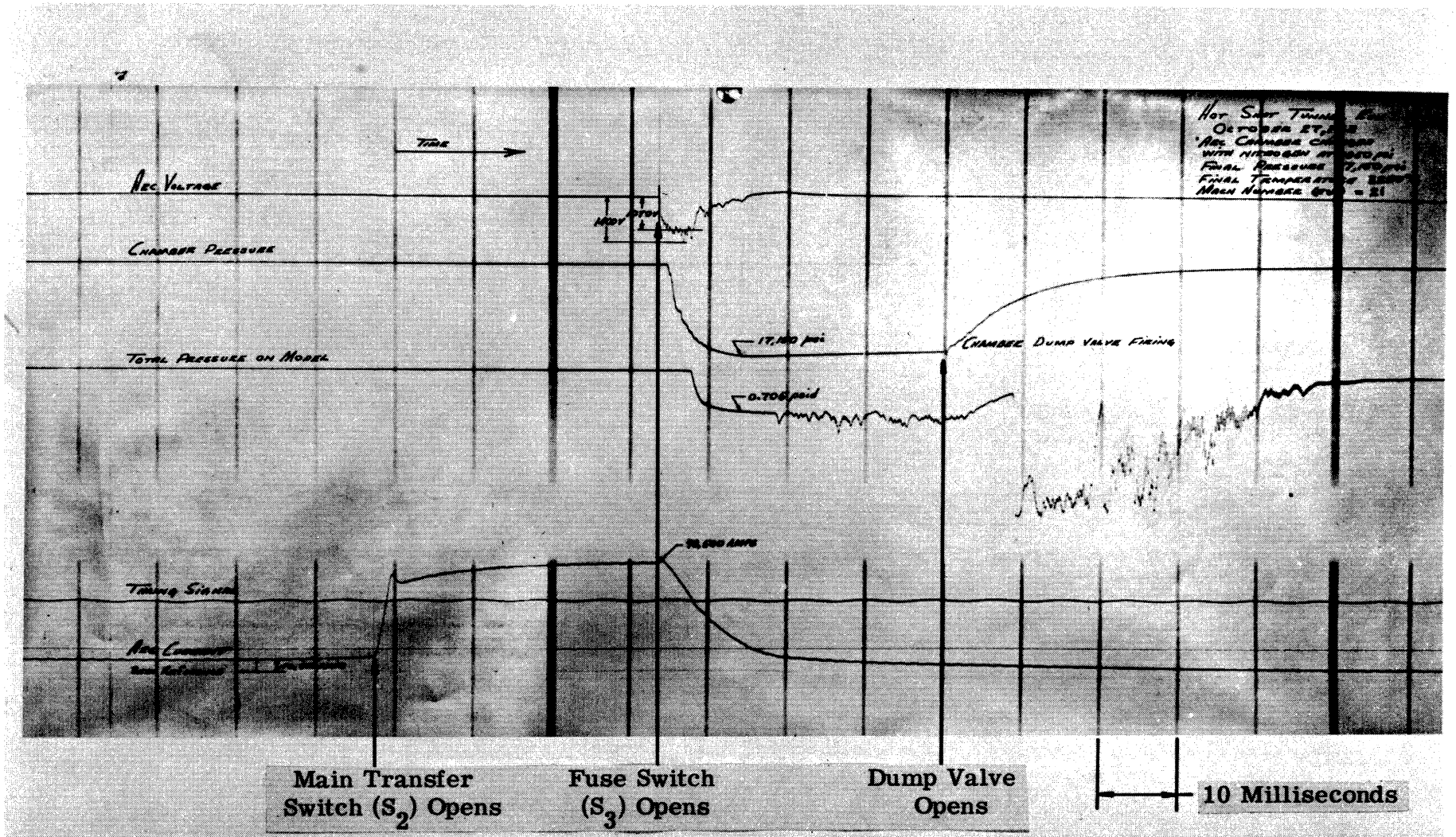

Figure 17. Oscillograph Trace of Typical Tunnel Run

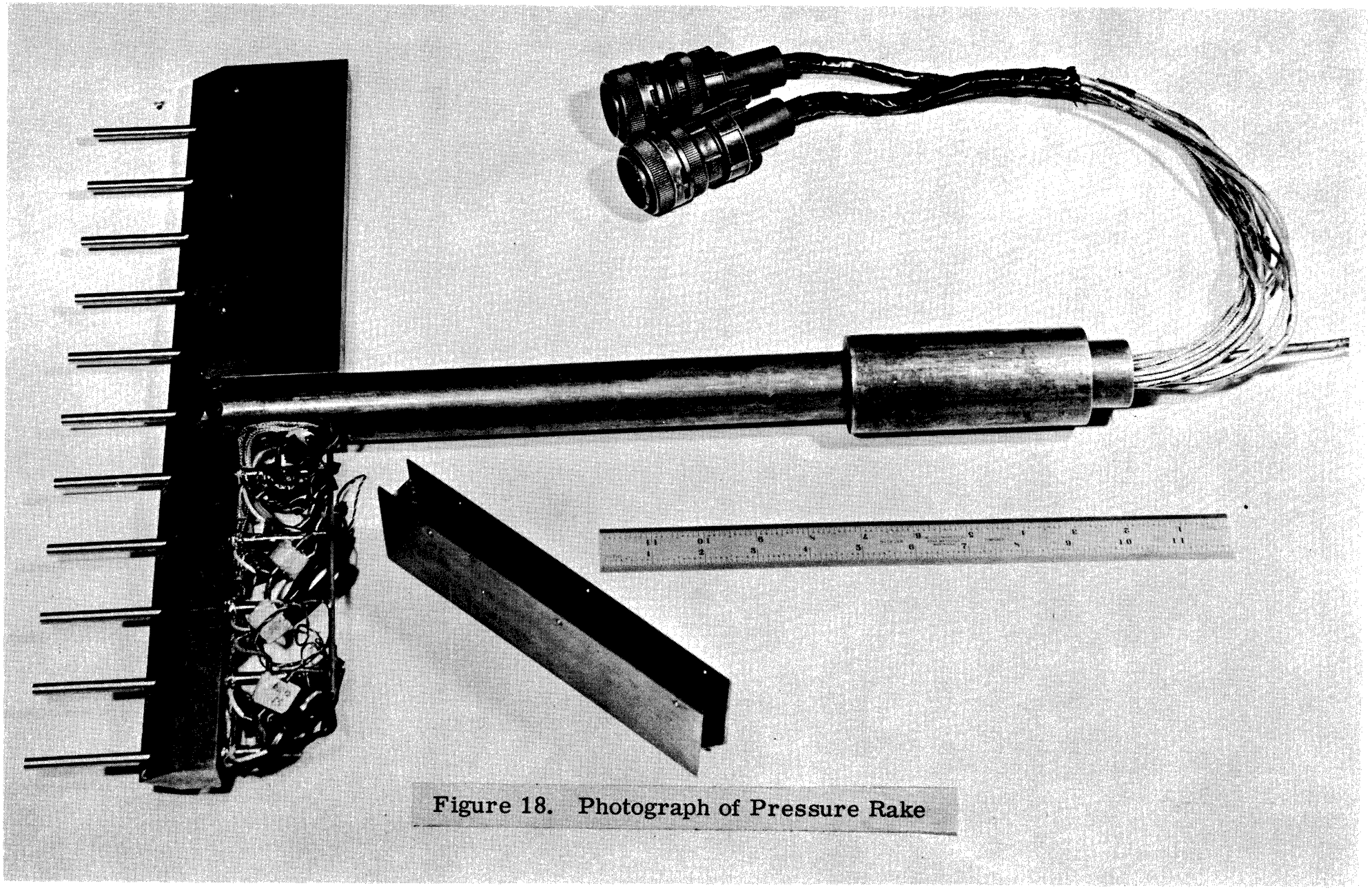

Figure 18. Photograph of Pressure Rake

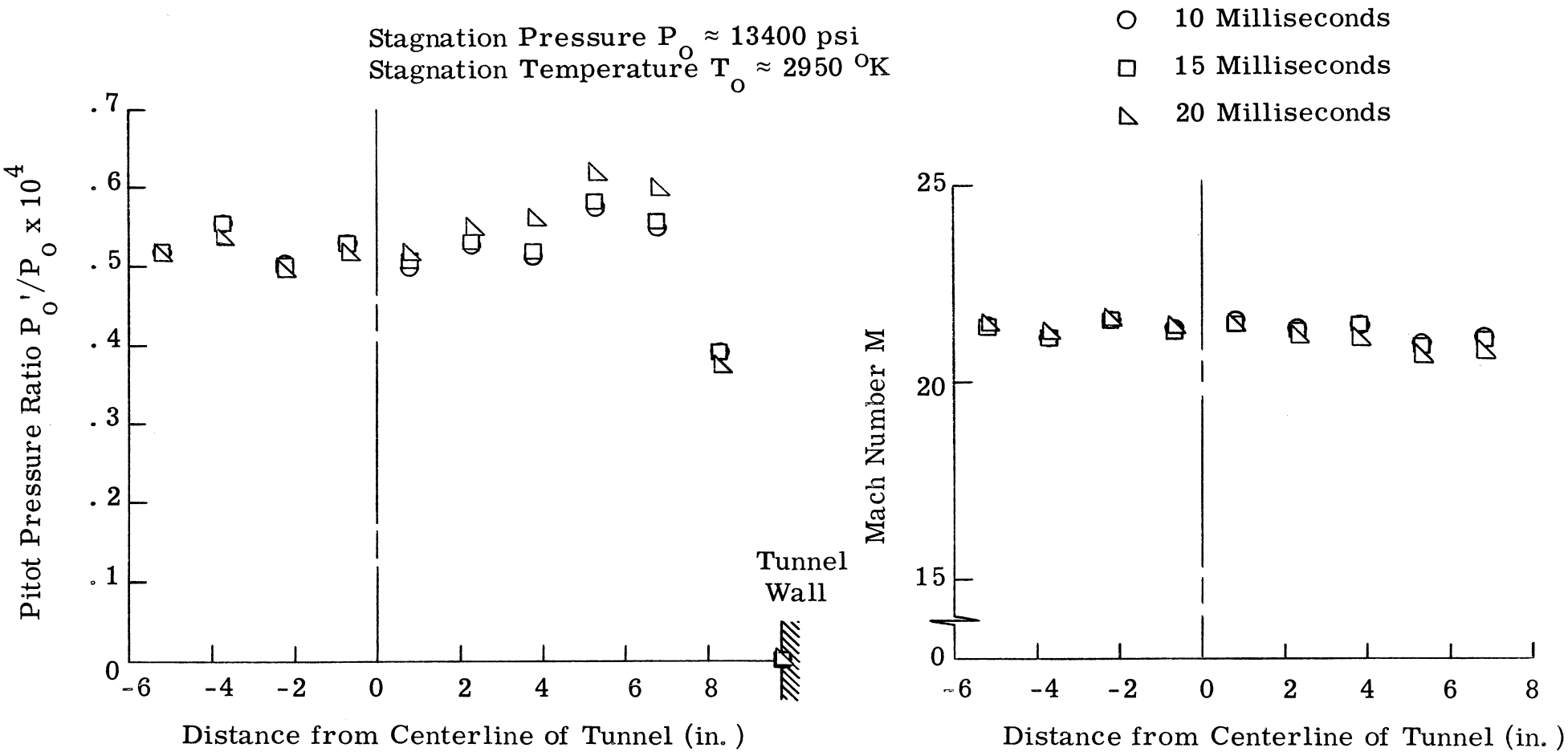

Figure 19. Pitot Pressure Ratio and Mach Number Profiles for a Typical Run with Pressure Rake Vertical and Offset

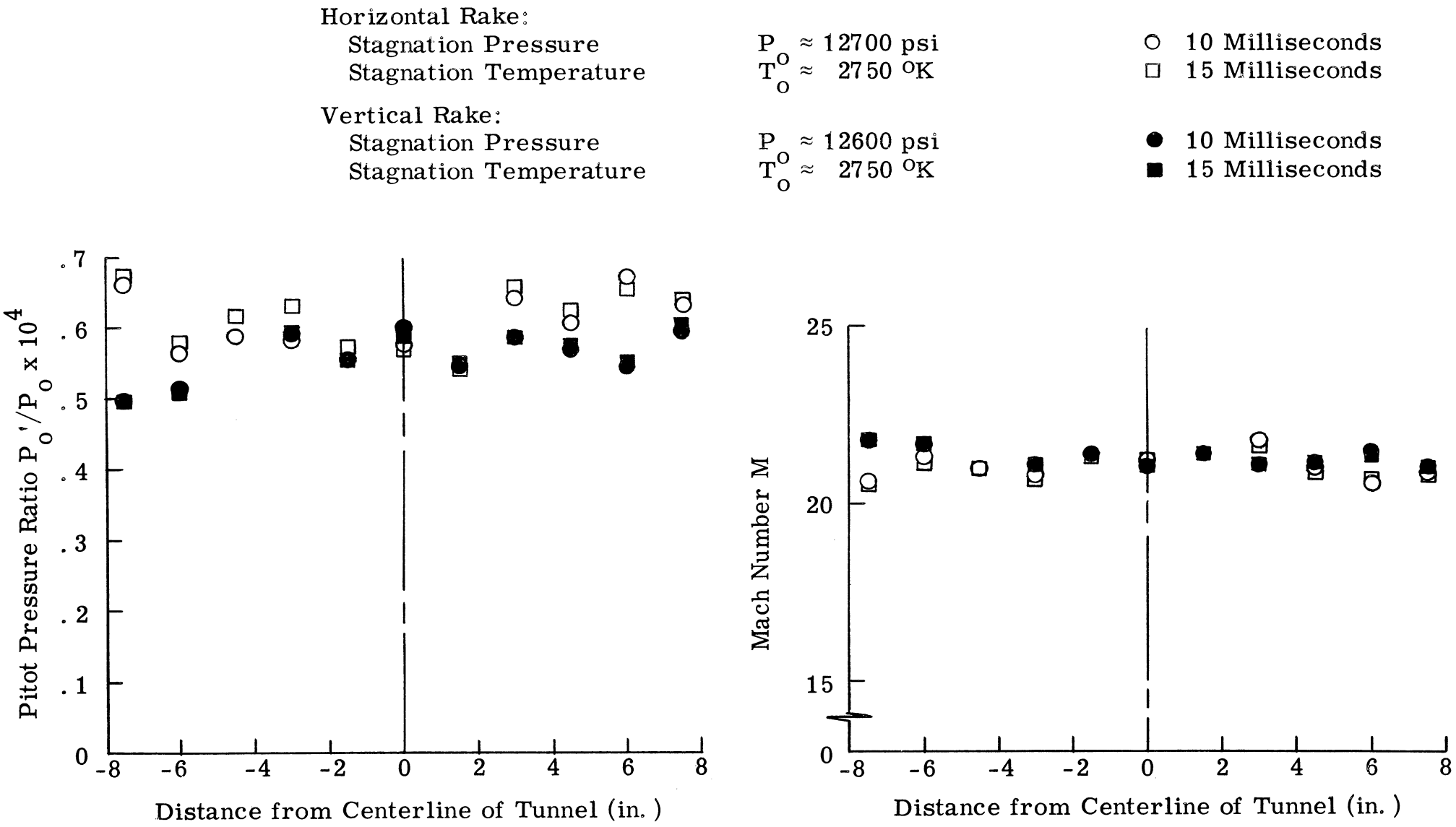

Figure 20. Pitot Pressure Ratio and Mach Number Profiles for Typical Runs with Horizontal Pressure Rake and with Vertical Pressure Rake

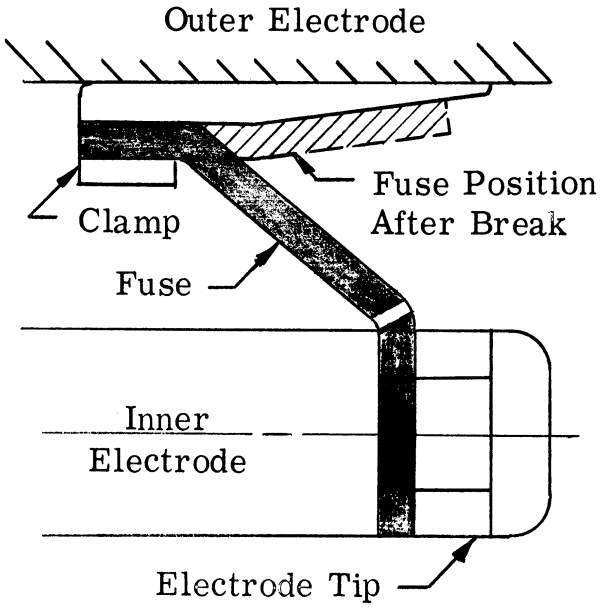

Figure A-1. Fuse Configuration

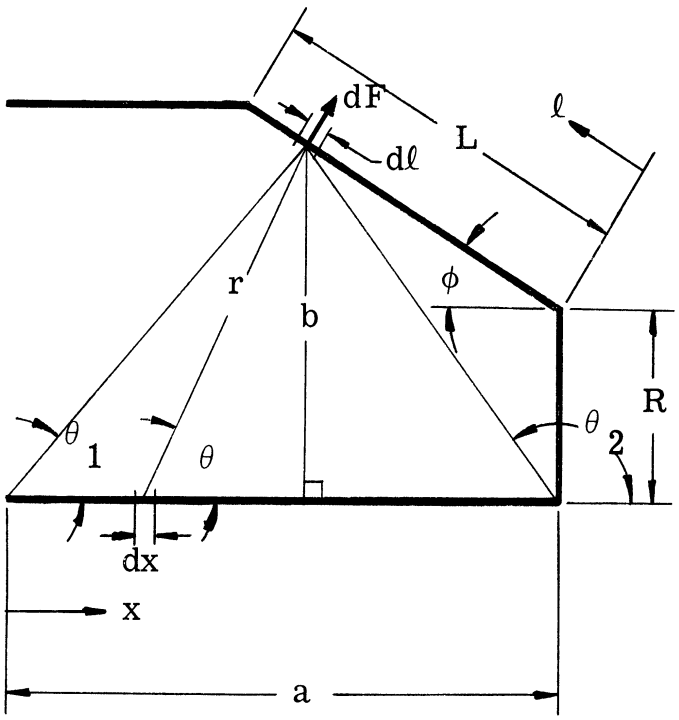

Figure A-2. Fuse Schematic and Nomenclature

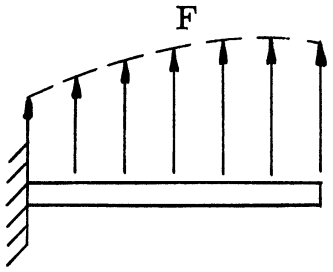

Figure A-3. Actual Force Distribution on Fuse

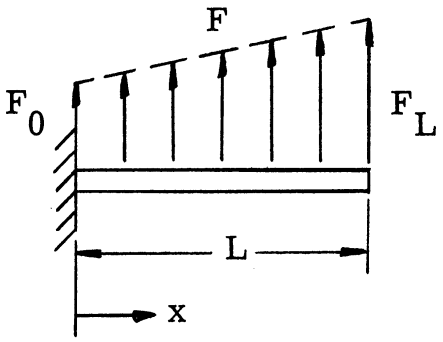

Figure A-4. Linearized Force Distribution on Fuse

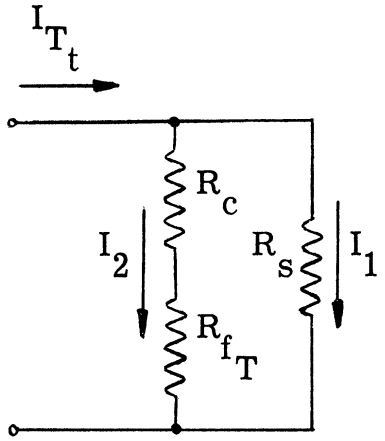

Figure A-5. Main Bus Bar Current Circuit Schematic Prior to Main Switch Opening

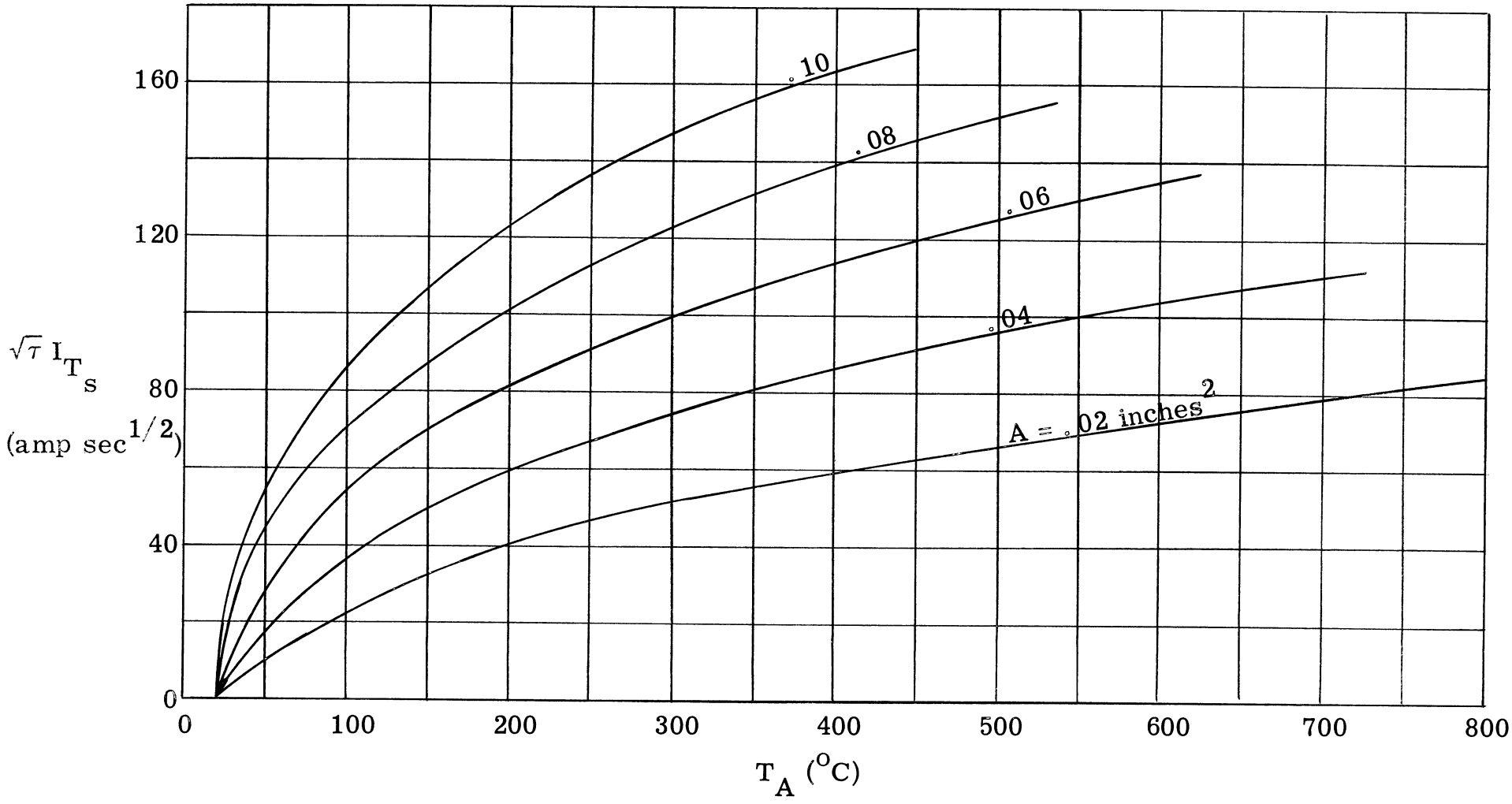

Figure A-6. Fuse Heating Prior to Main Switch Opening

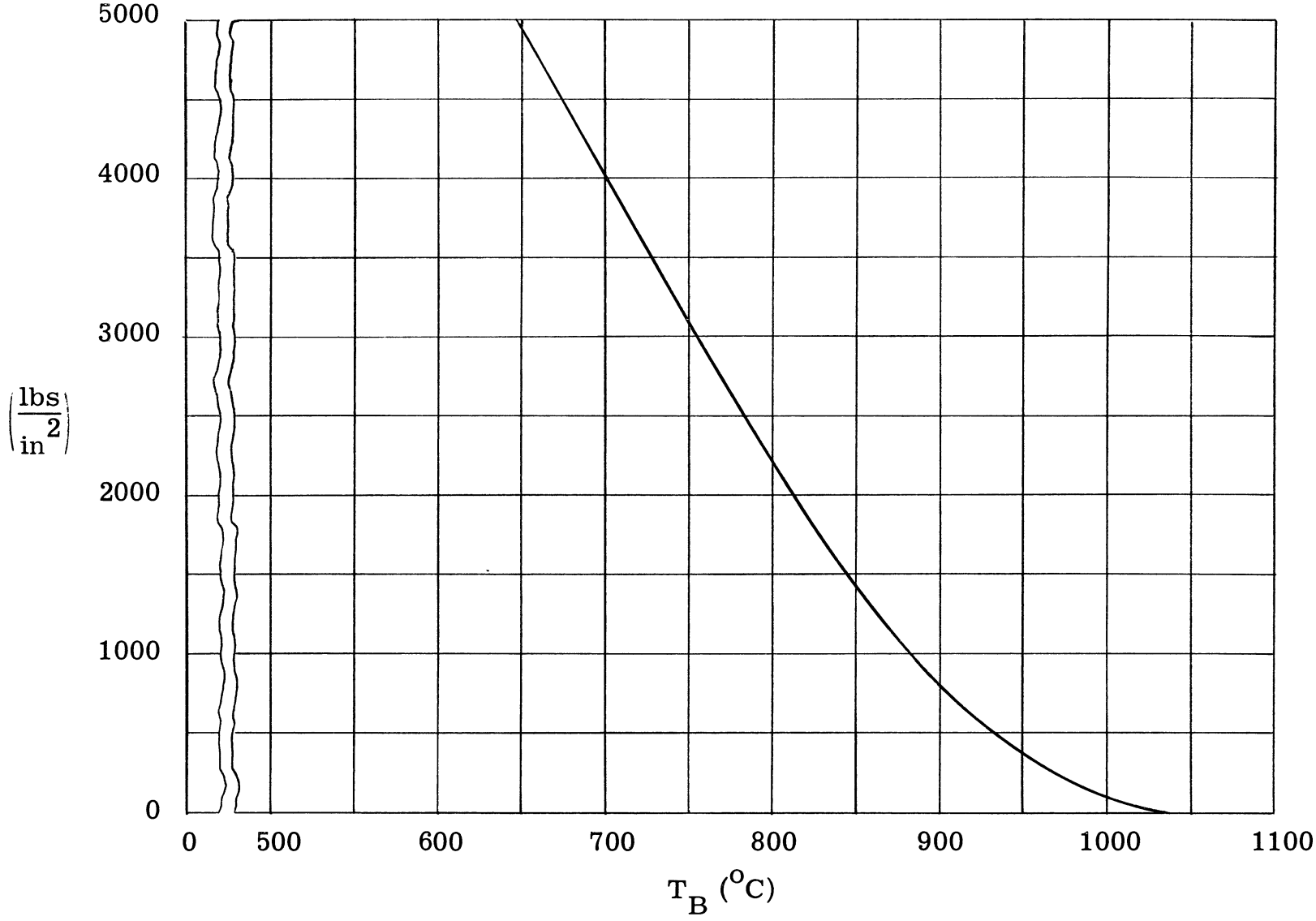

Figure A-7. Tensile Strength of Copper versus Temperature

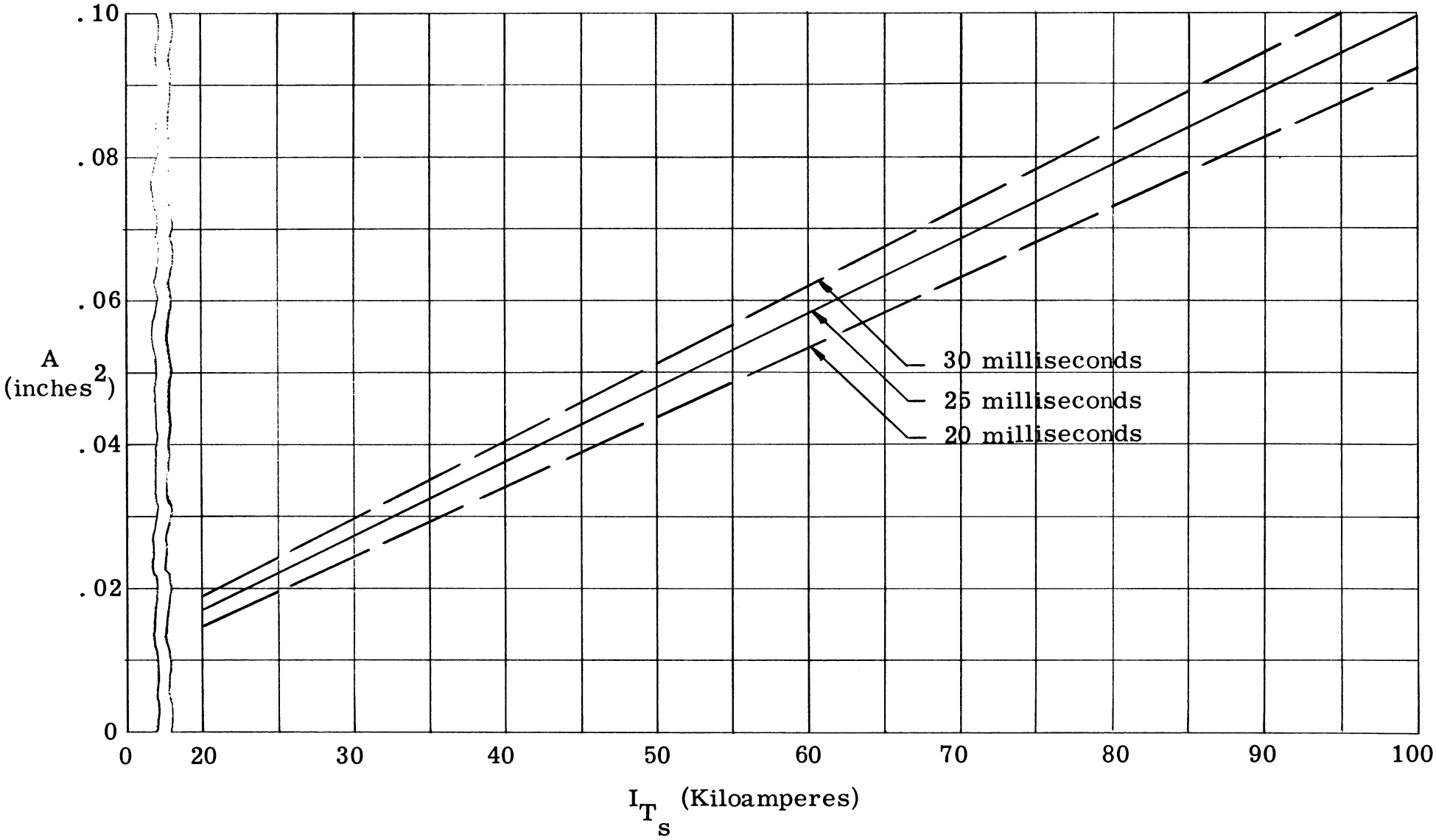

Figure A-8. Cross-Sectional Area versus Run Current for Three Values of Fuse Breakage Time (τ = 1. 5 seconds)

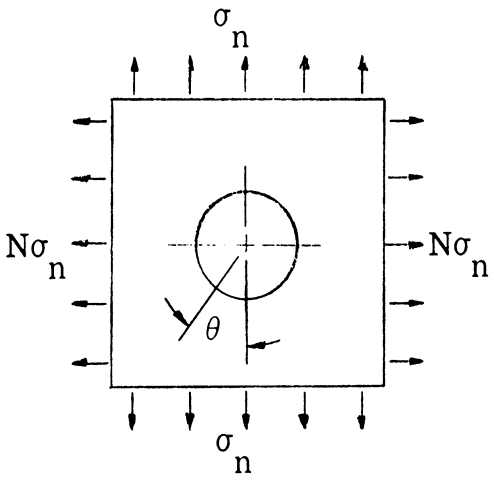

Figure B-1. Initial Uniform Stresses Applied to an Infinite Flat Plate with a Hole.

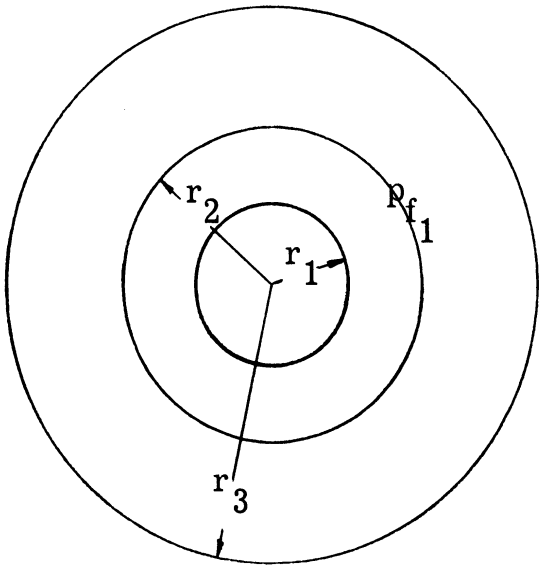

Figure B-2. Nomenclature for Two-Shell Analysis.

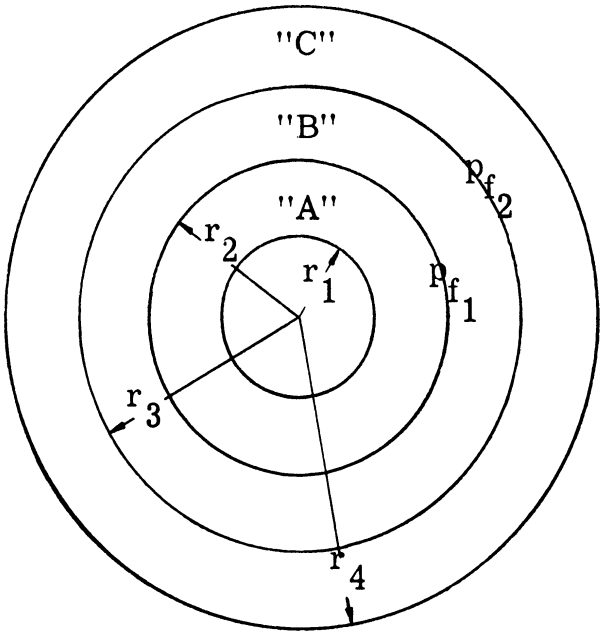

Figure B-3. Nomenclature for Three-Shell Analysis.

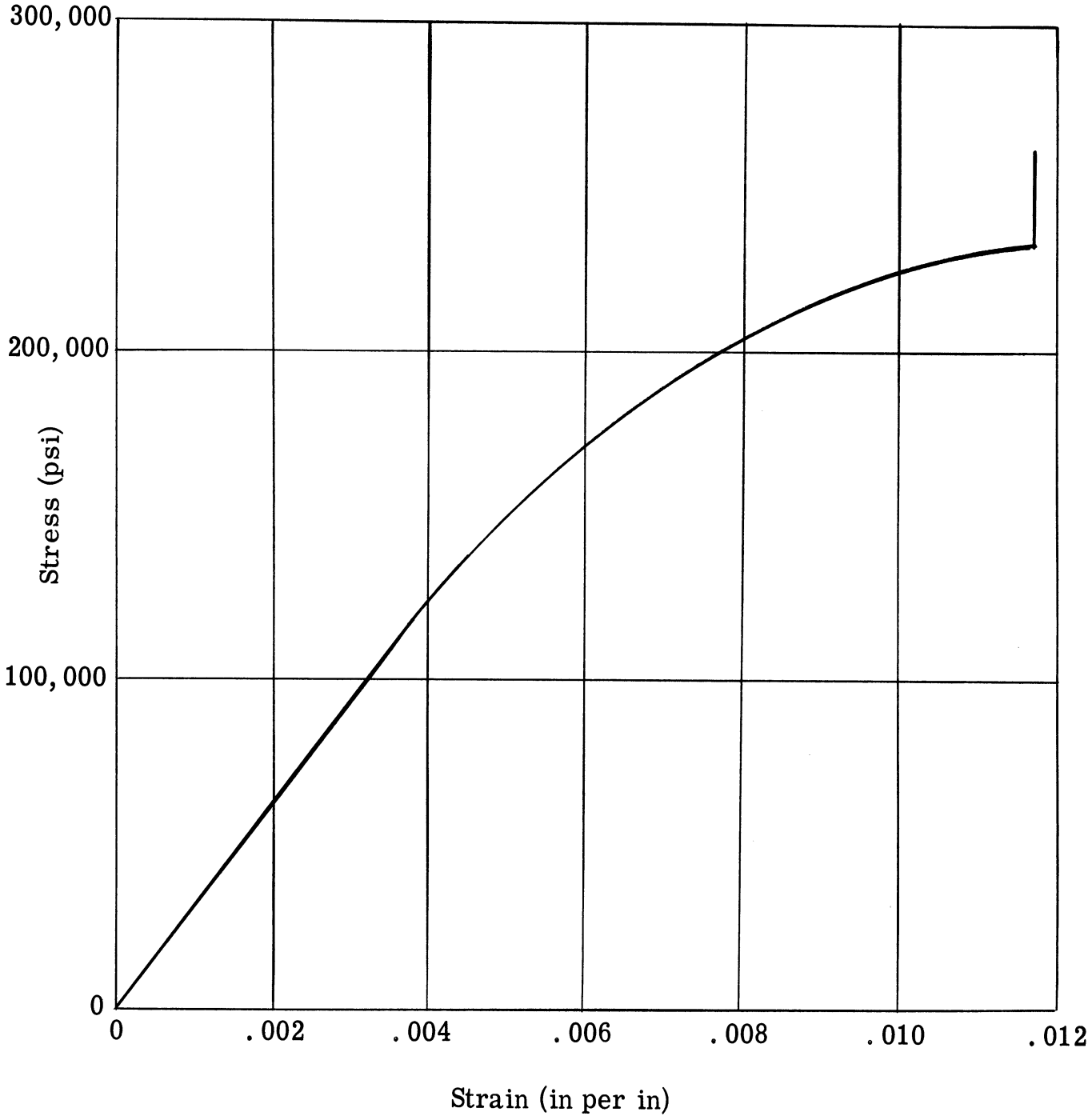

Figure B-4. Typical Stress—Strain Curve for Potomac "A" Steel

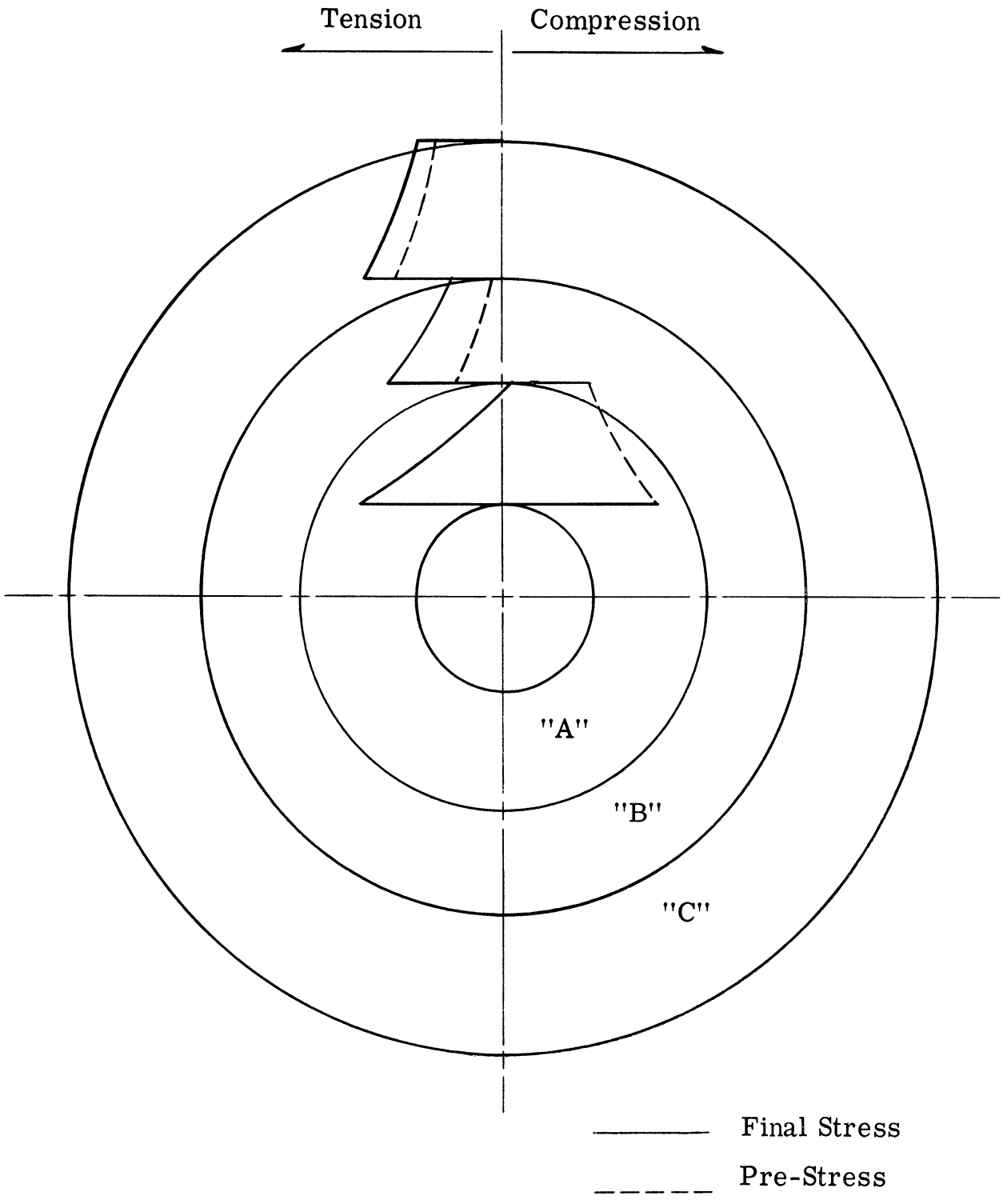

Figure B-5. Stress Distribution Including Effect of Side Holes (with operating pressure of 80,000 psi).

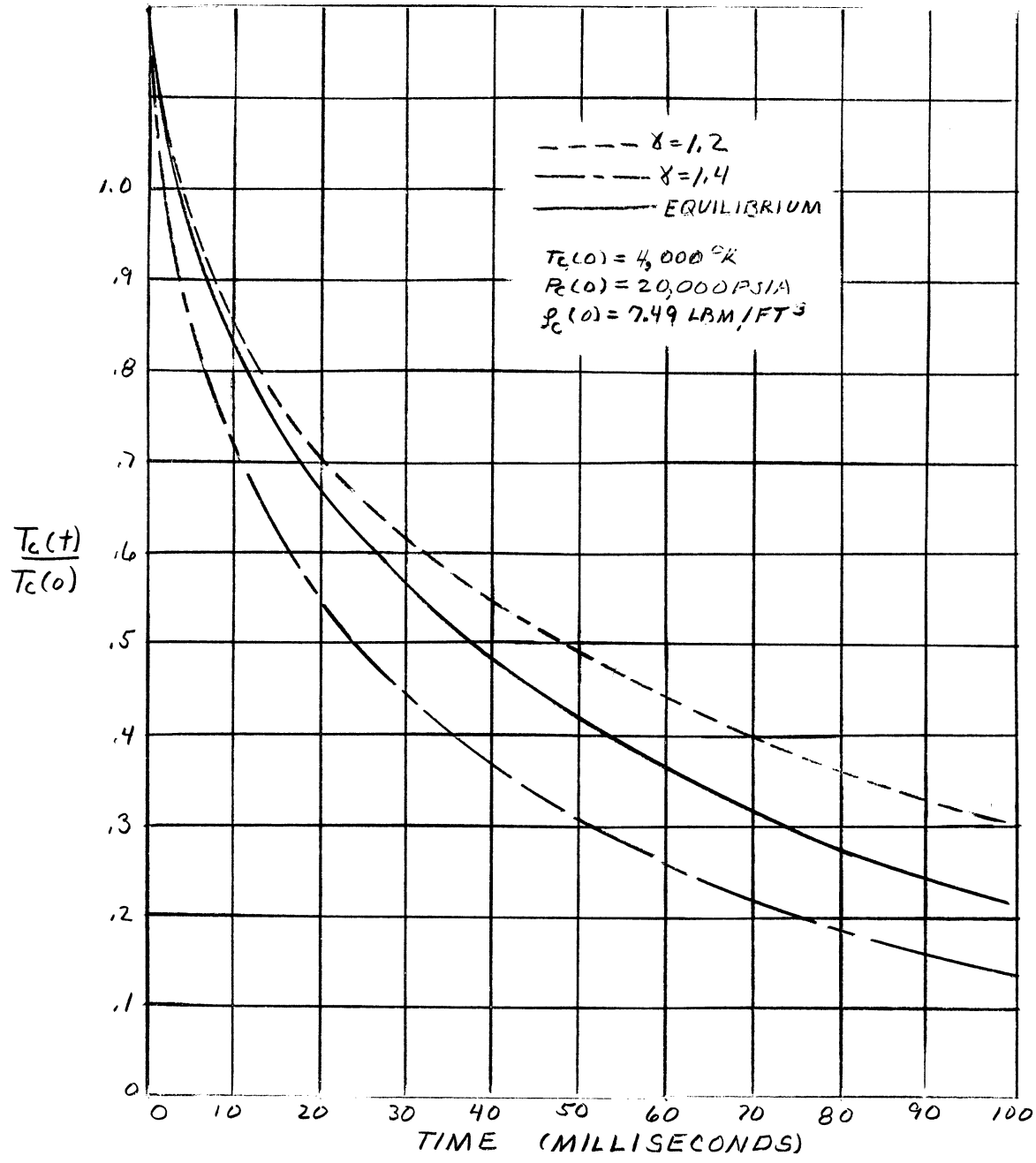

TEMPERATURE VARIATION DURING BLOWDOWD THROUGH DUMP PORT

FIG. C-1

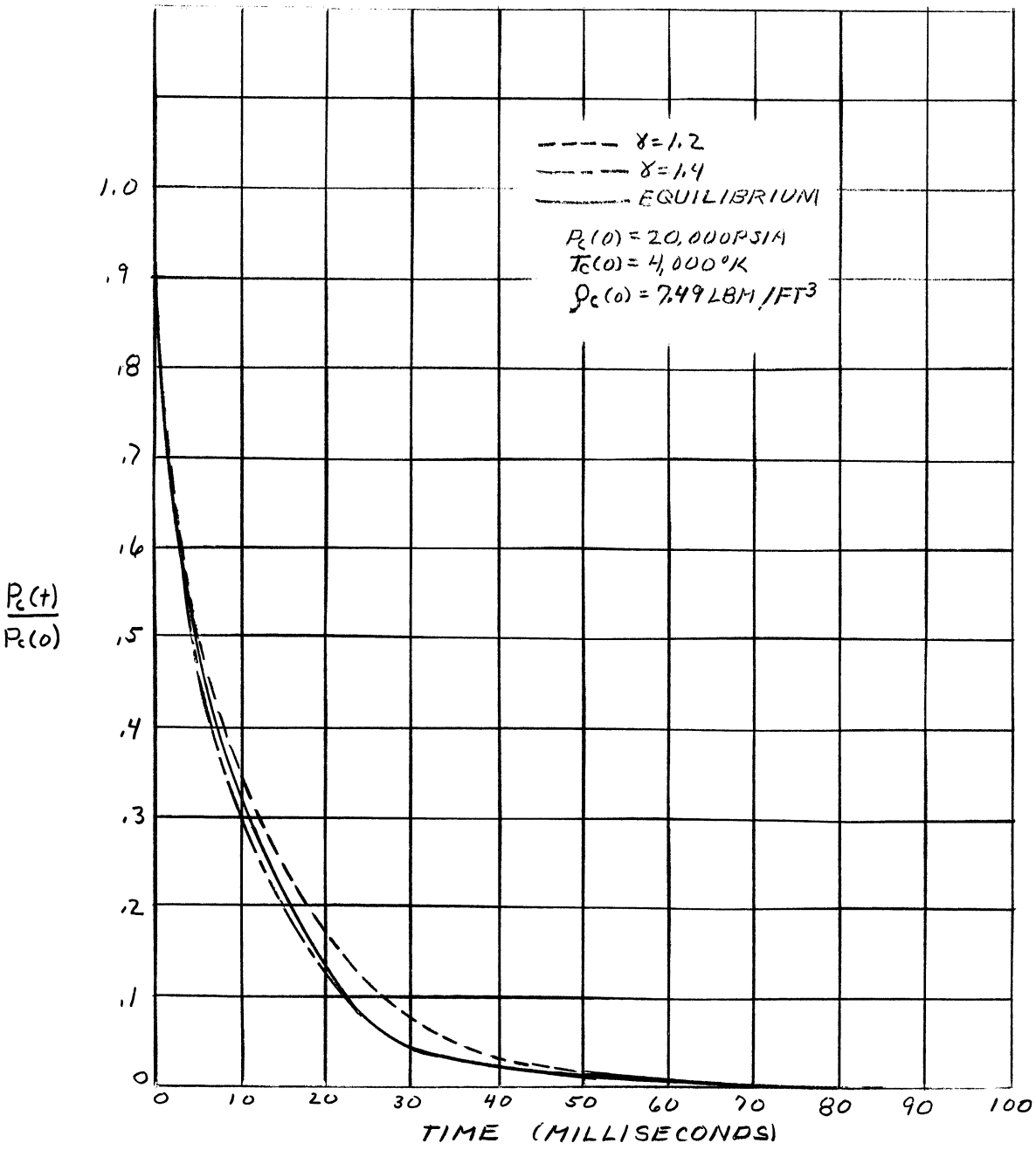

PRESSURE VARIATION DURING BLOWDOWN THROUGH DUMP PORT

FIG. C-2

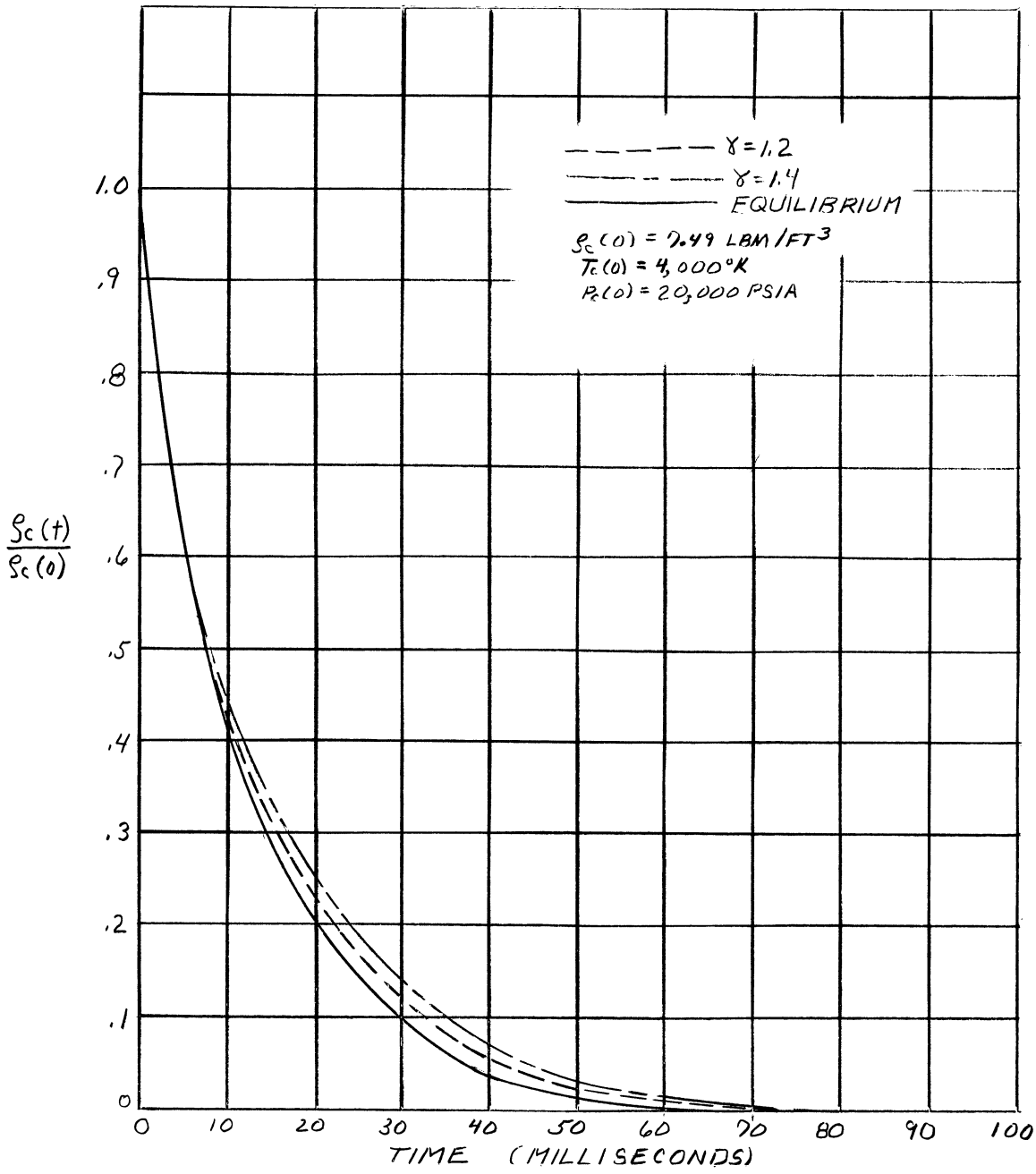

DENSITY VARIATION DURING BLOWDOWN THROUGH DUMP PORT

FIG. C-3

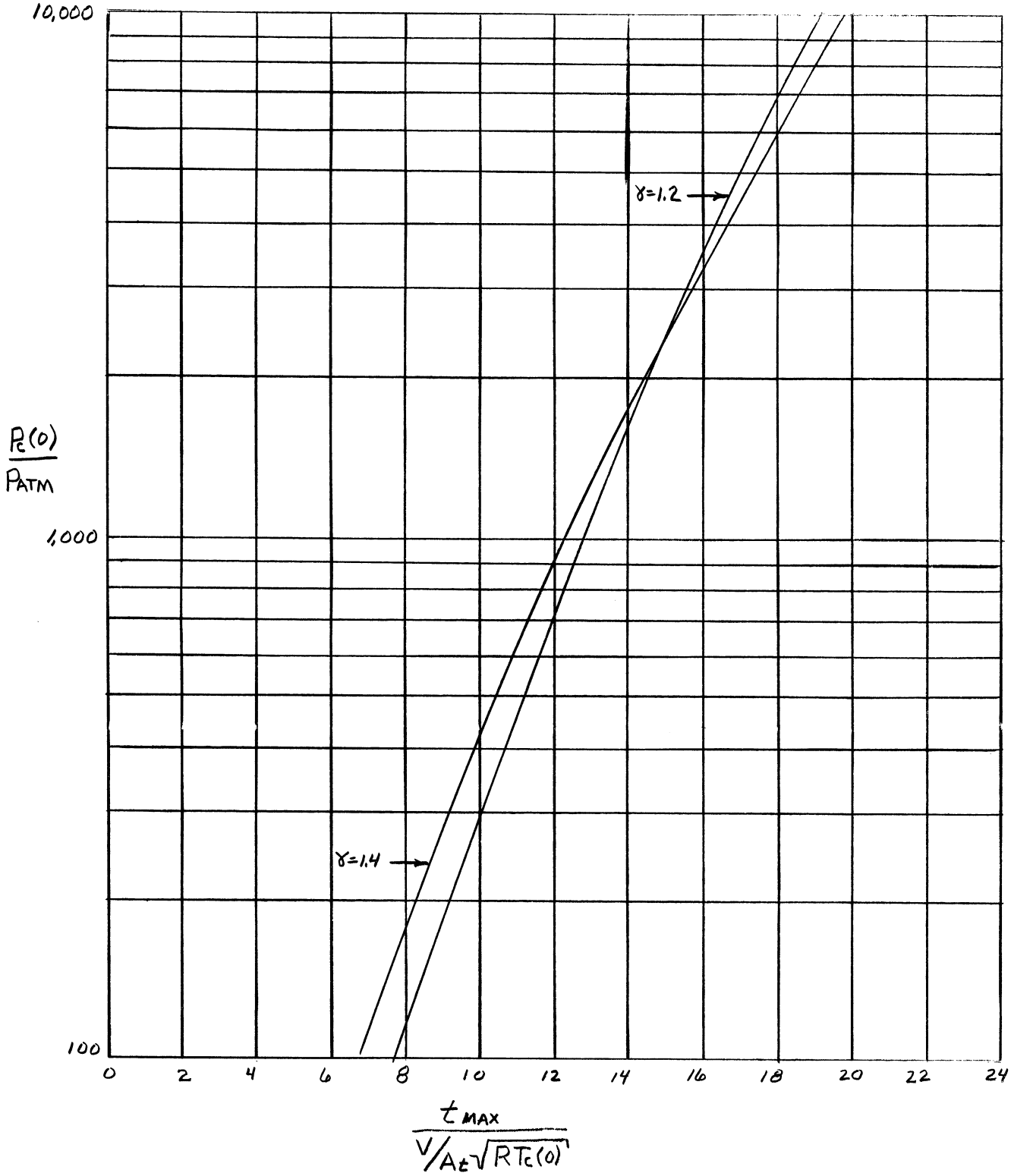

NON-DIMENSIONAL BLOWDOWN TIME VS. INITIAL PRESSURE RATIO

FIG. C-4

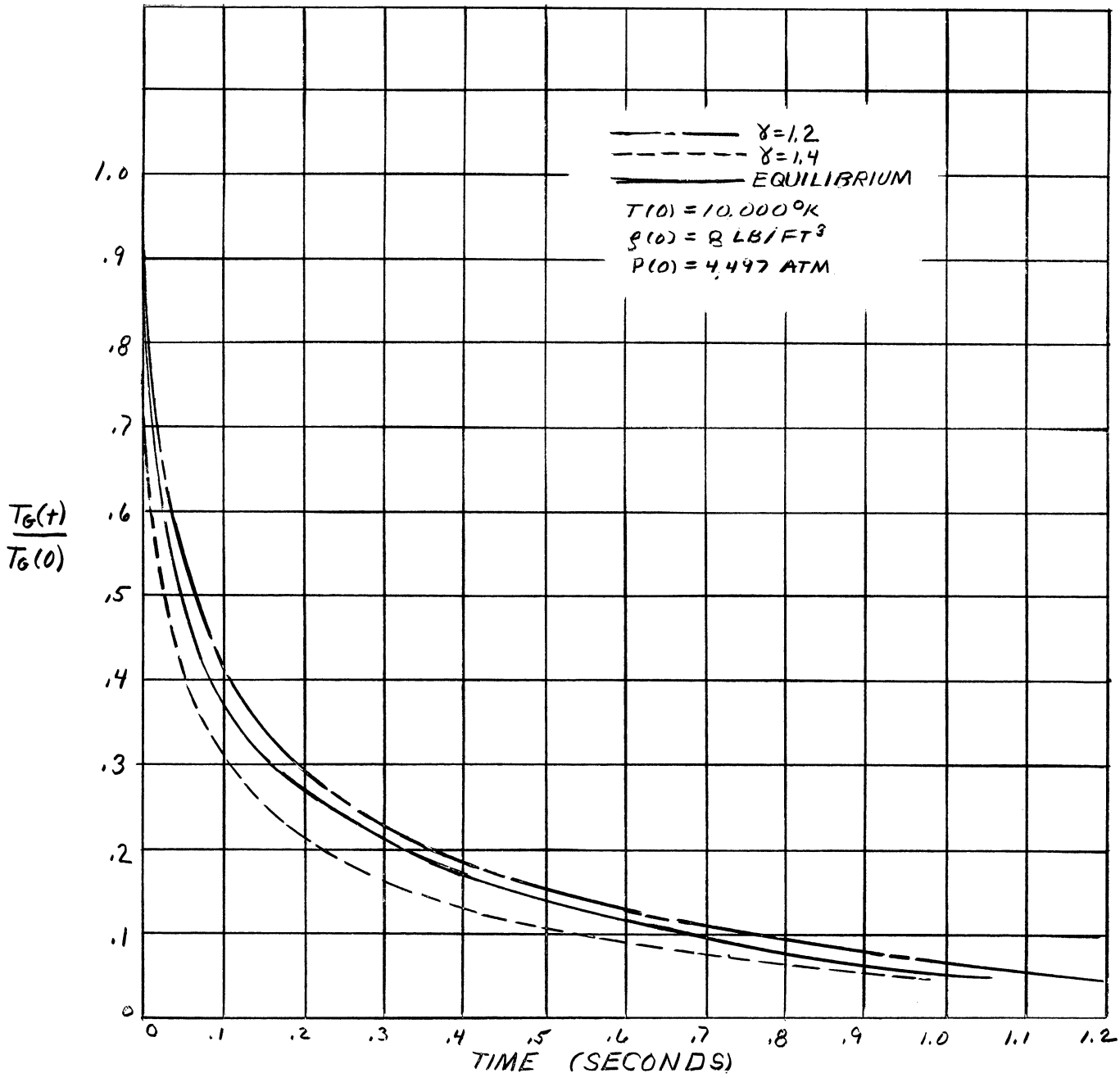

TEMPERATURE VARIATION DURING BLOWDOWN THROUGH TUNNEL

FIG. C-5

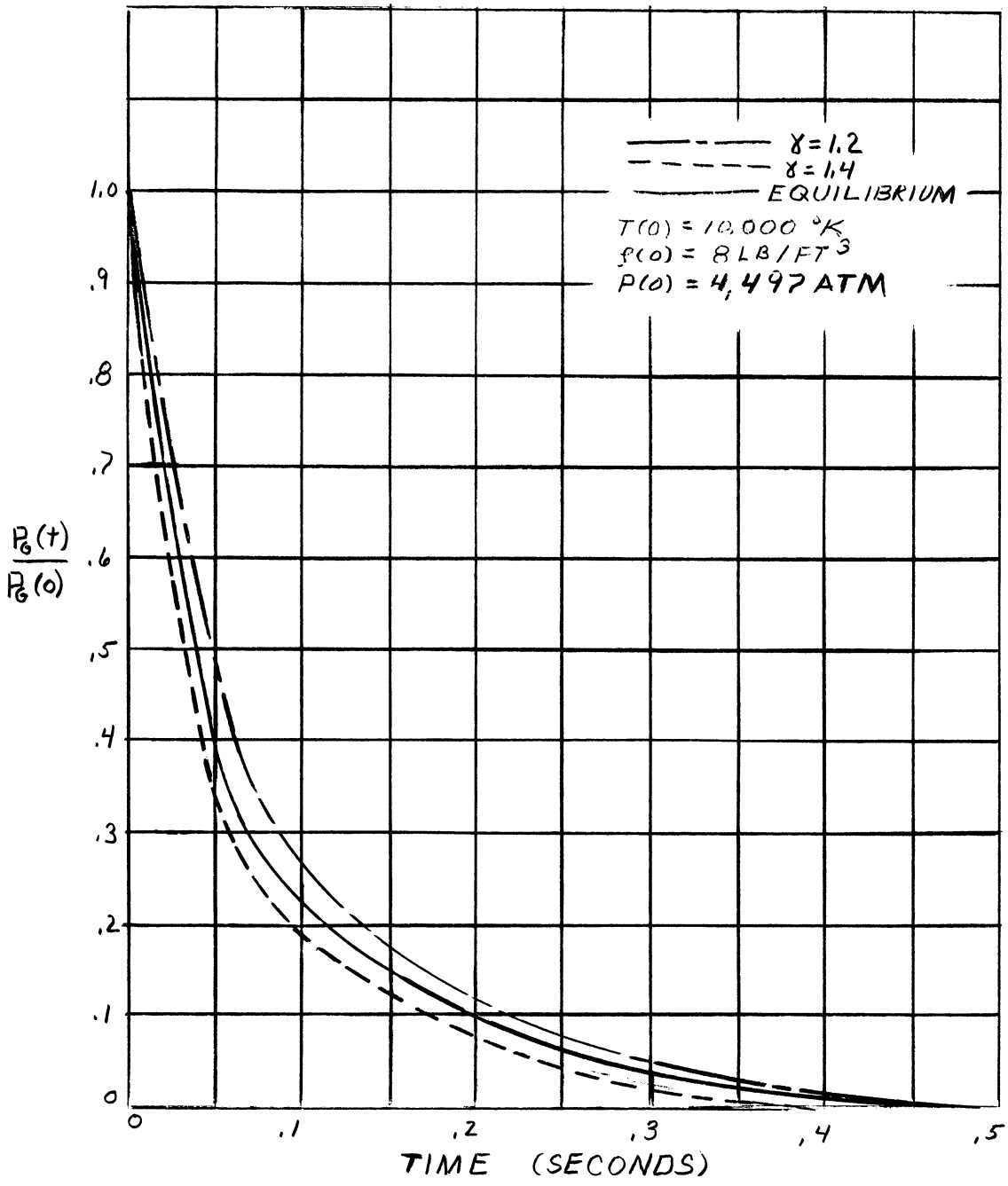

PRESSURE VARIATION DURING BLOWDOWN THROUGH TUNNEL

FIG. C-6

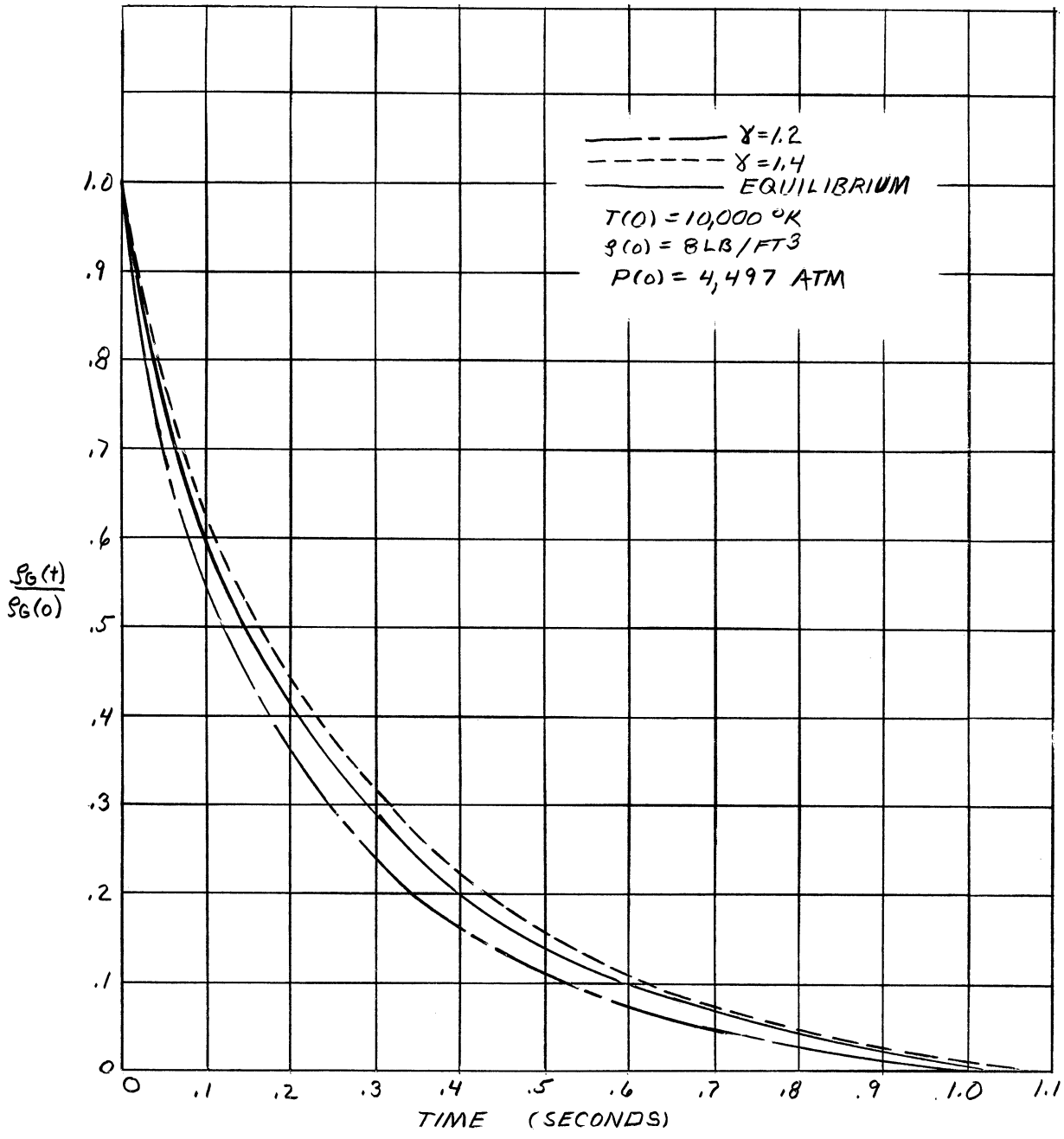

DENSITY VARIATION DURING BLOWDOWN THROUGH TUNNEL

FIG. C-7

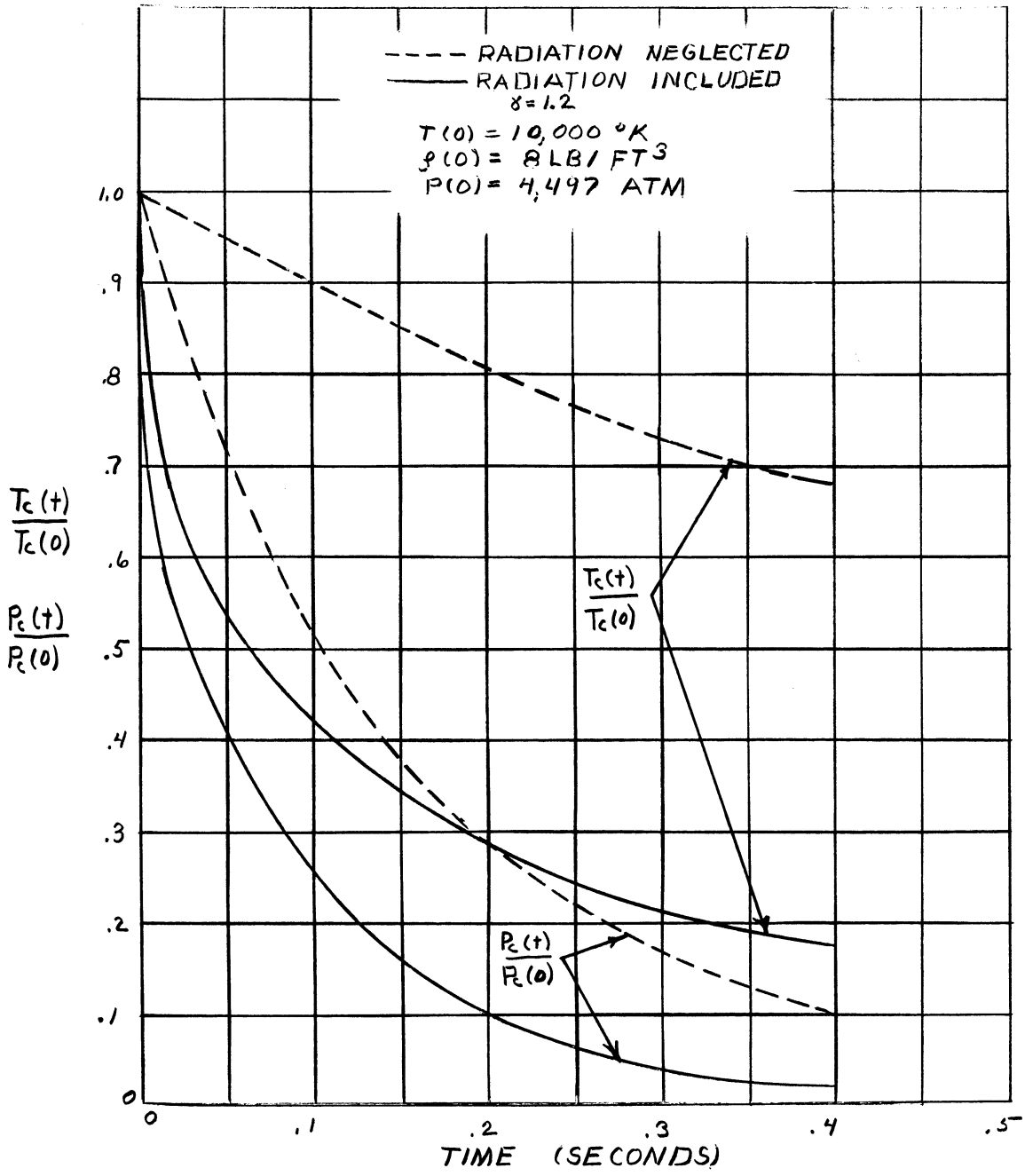

EFFECT OF RADIATION ON TEMPERATURE AND PRESSURE VARIATIONS

FIG. C-8

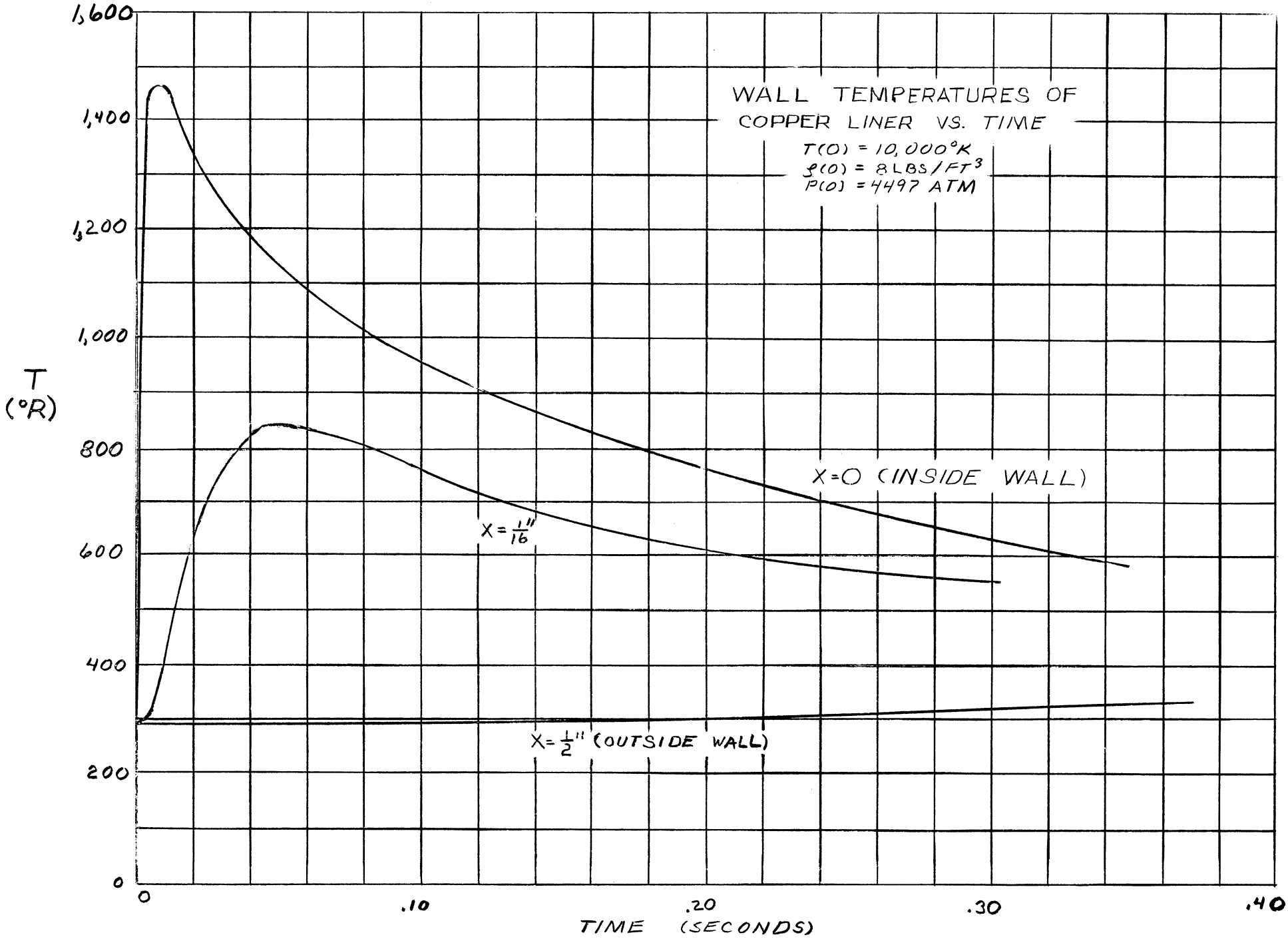
WALL TEMPERATURES OF
COPPER LINER VS. TIME
T(0) = 10,000°K
ρ(0) = 8 LBS/FT³
P(0) = 4497 ATM
X=0 (INSIDE WALL)
X = 1/16"
X = 1/2" (OUTSIDE WALL)
T (°R)
1,600
1,400
1,200
1,000
800
600
400
200
0
0
.10
.20
.30
.40
TIME (SECONDS)

FIG. C-9

COMPARISONS OF CYLINDER AND SLAB SOLUTIONS FOR INNER SURFACE TEMPERATURE OF DUMP PORT INSERT

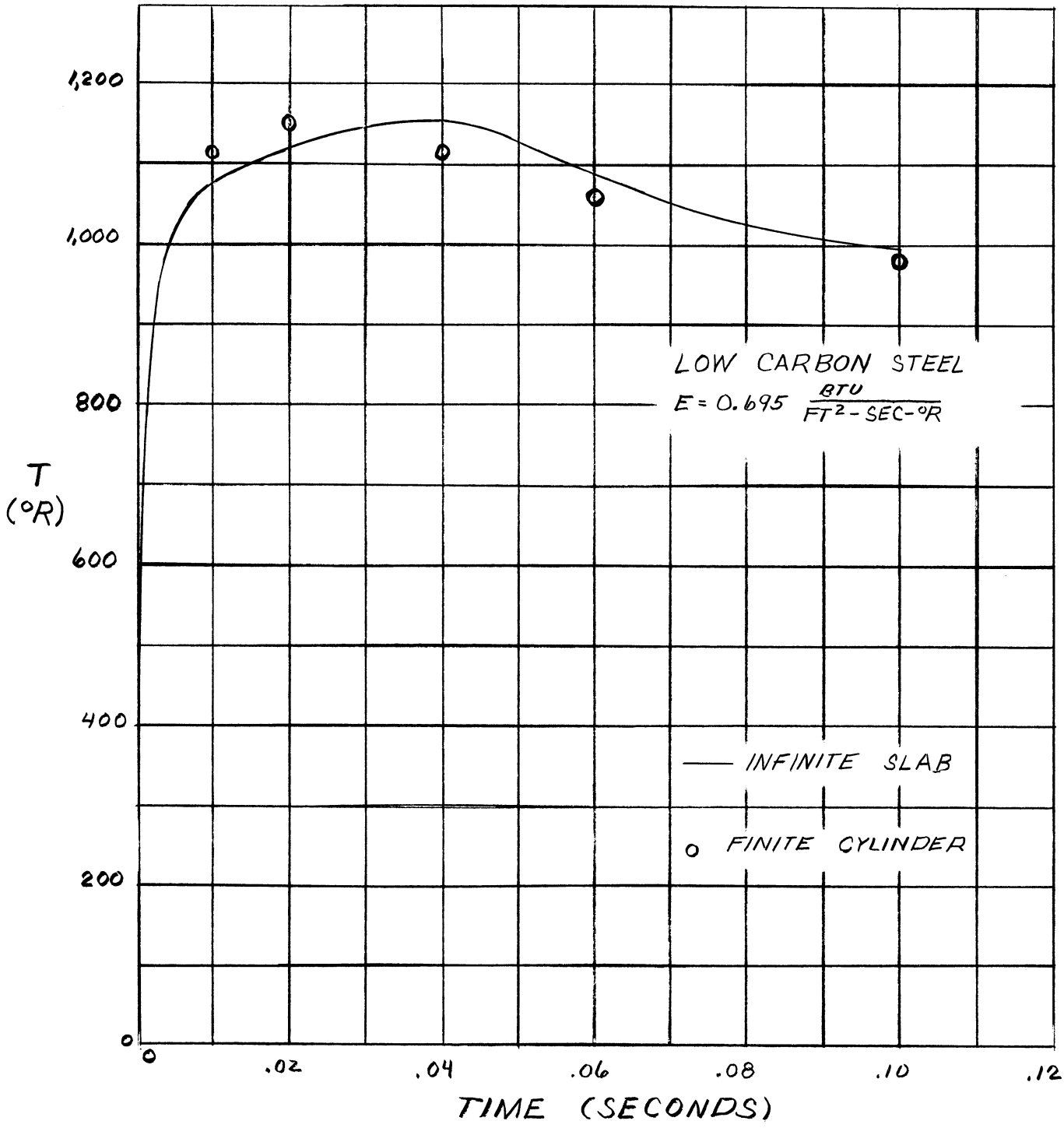

FIG. C-10

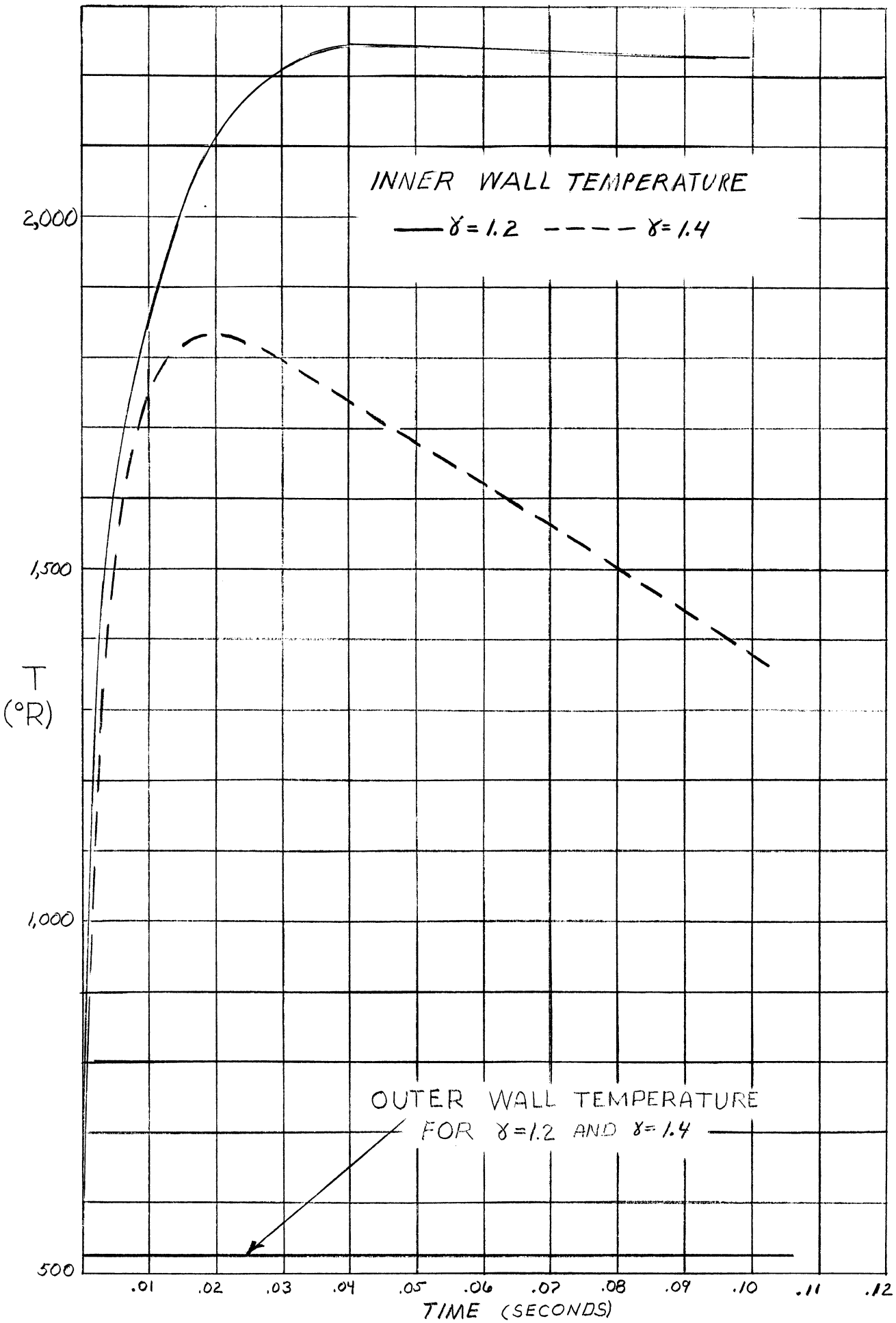

FIG. C-11 WALL TEMPERATURE OF STAINLESS STEEL INSERT

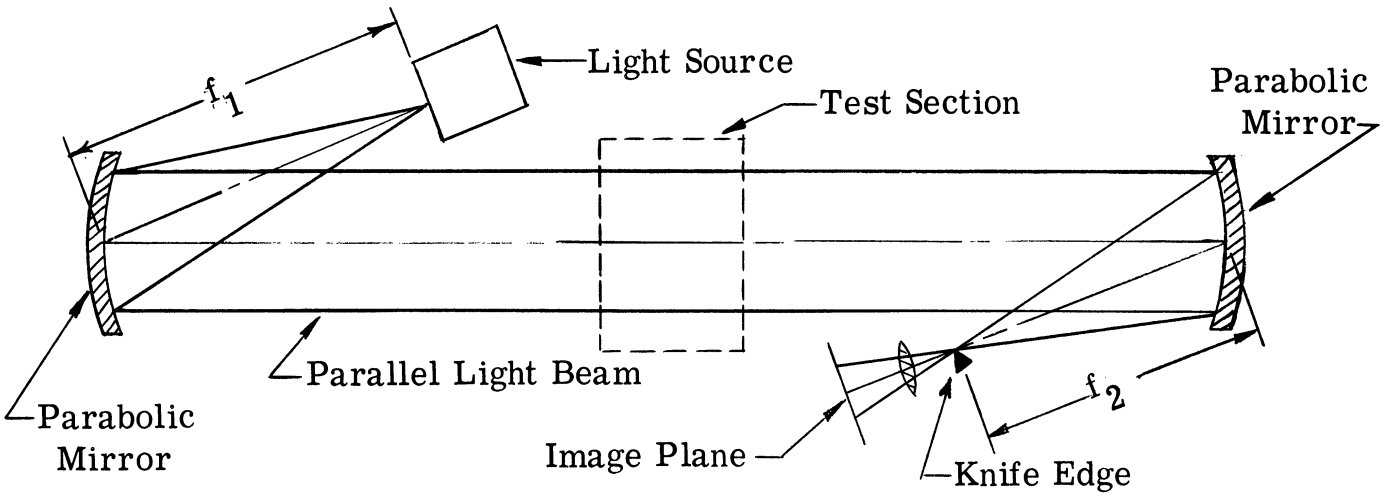

Single-Pass System

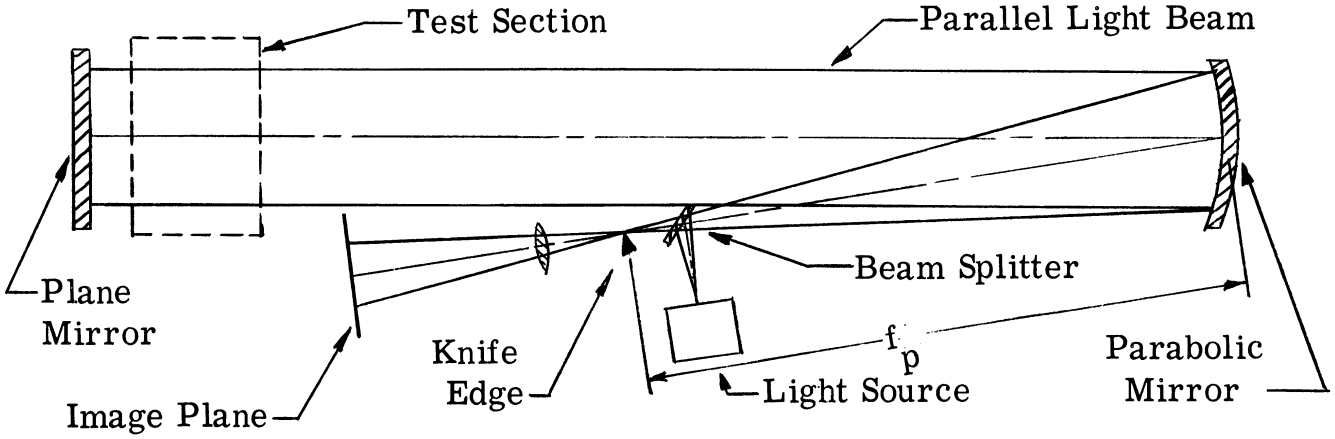

Double-Pass Parallel System

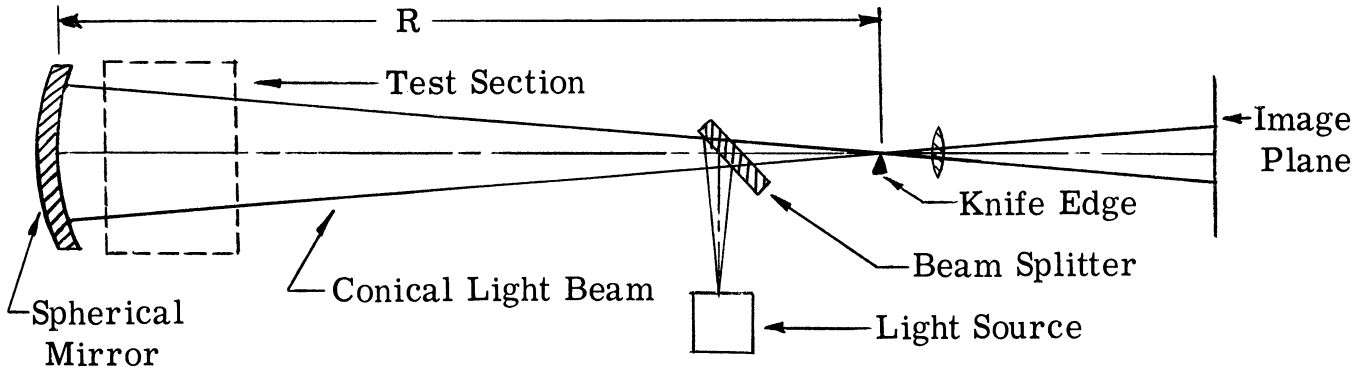

Double-Pass Non-Parallel System

Figure D-1. Types of Schlieren Systems

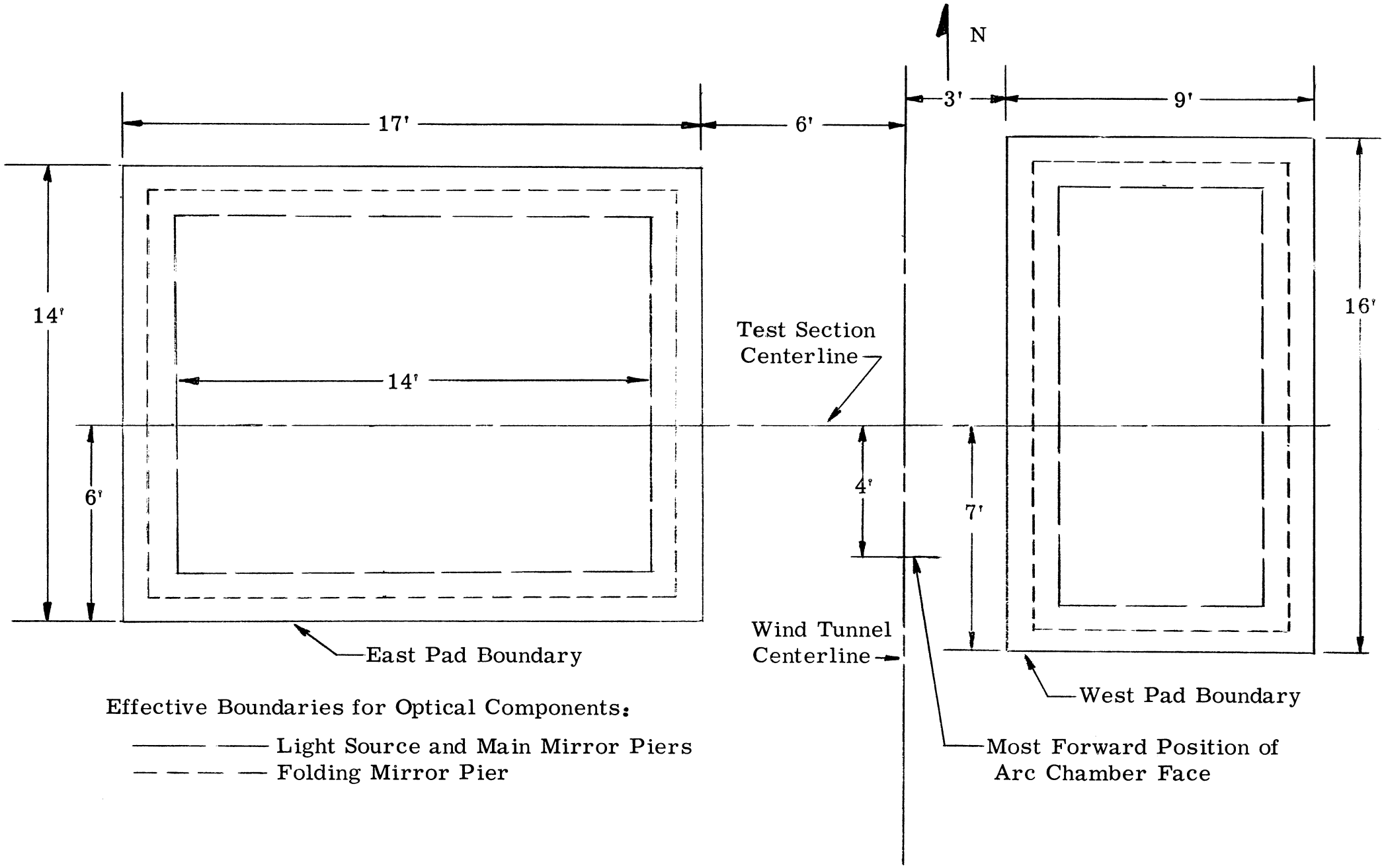

Figure D-2. Hypersonic Wind Tunnel Schlieren Pad Layout

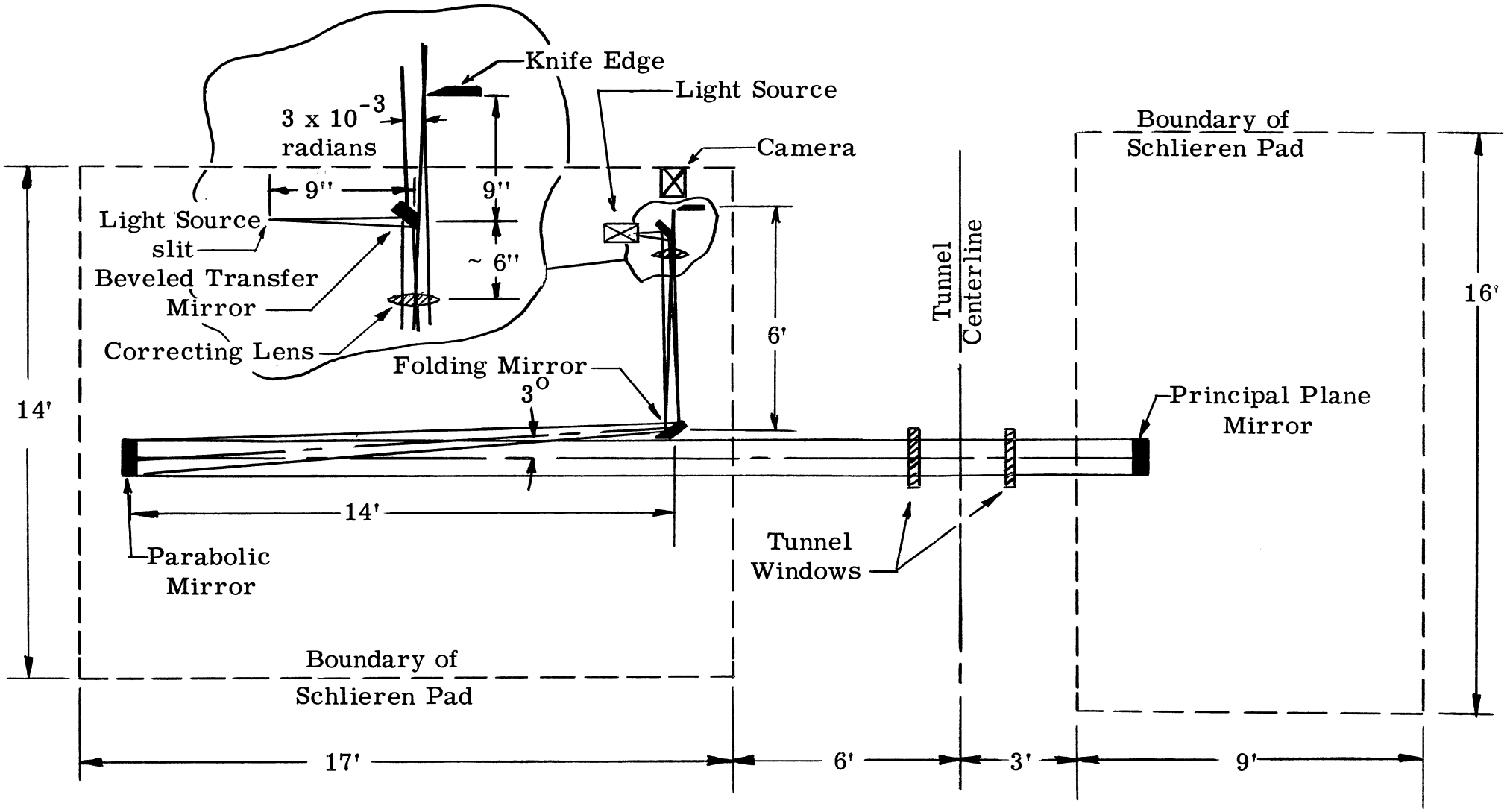

Figure D-3. Layout of High Sensitivity Schlieren System

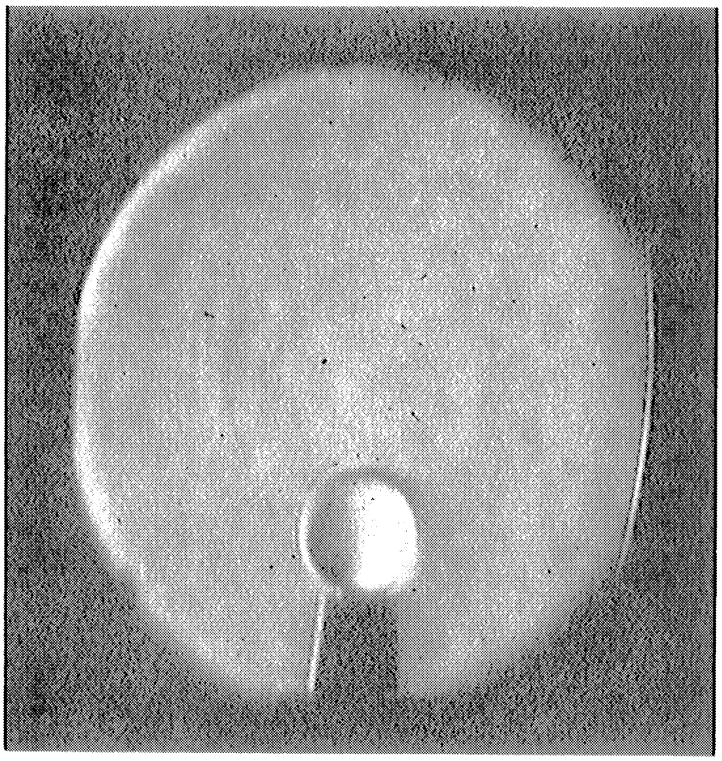

4a

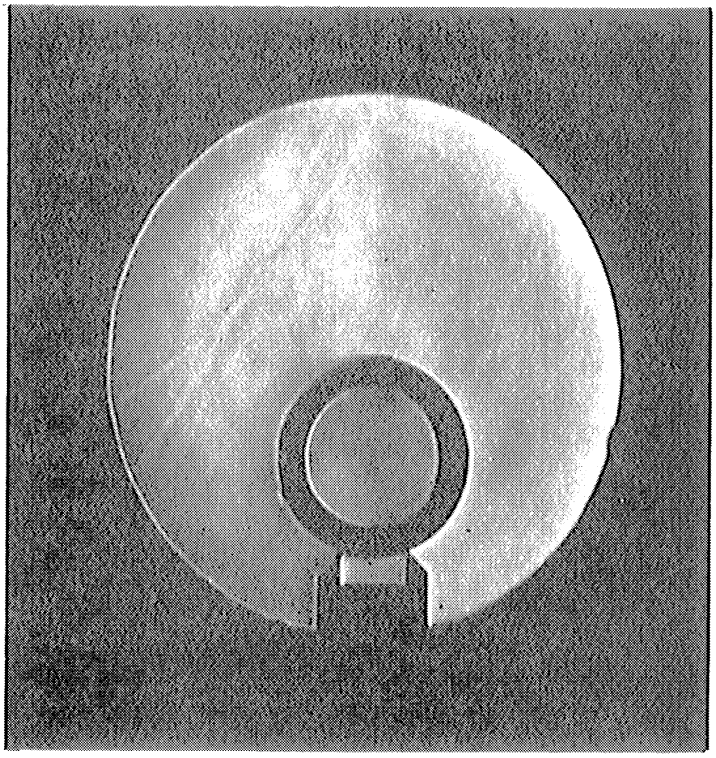

4b

Figure D-4. Schlieren System Evaluation Photographs (4a Without Windows, 4b With Windows)*

*40 sec exposure, 1.0×10^{-6} radian sensitivity, 2 sec wedge.

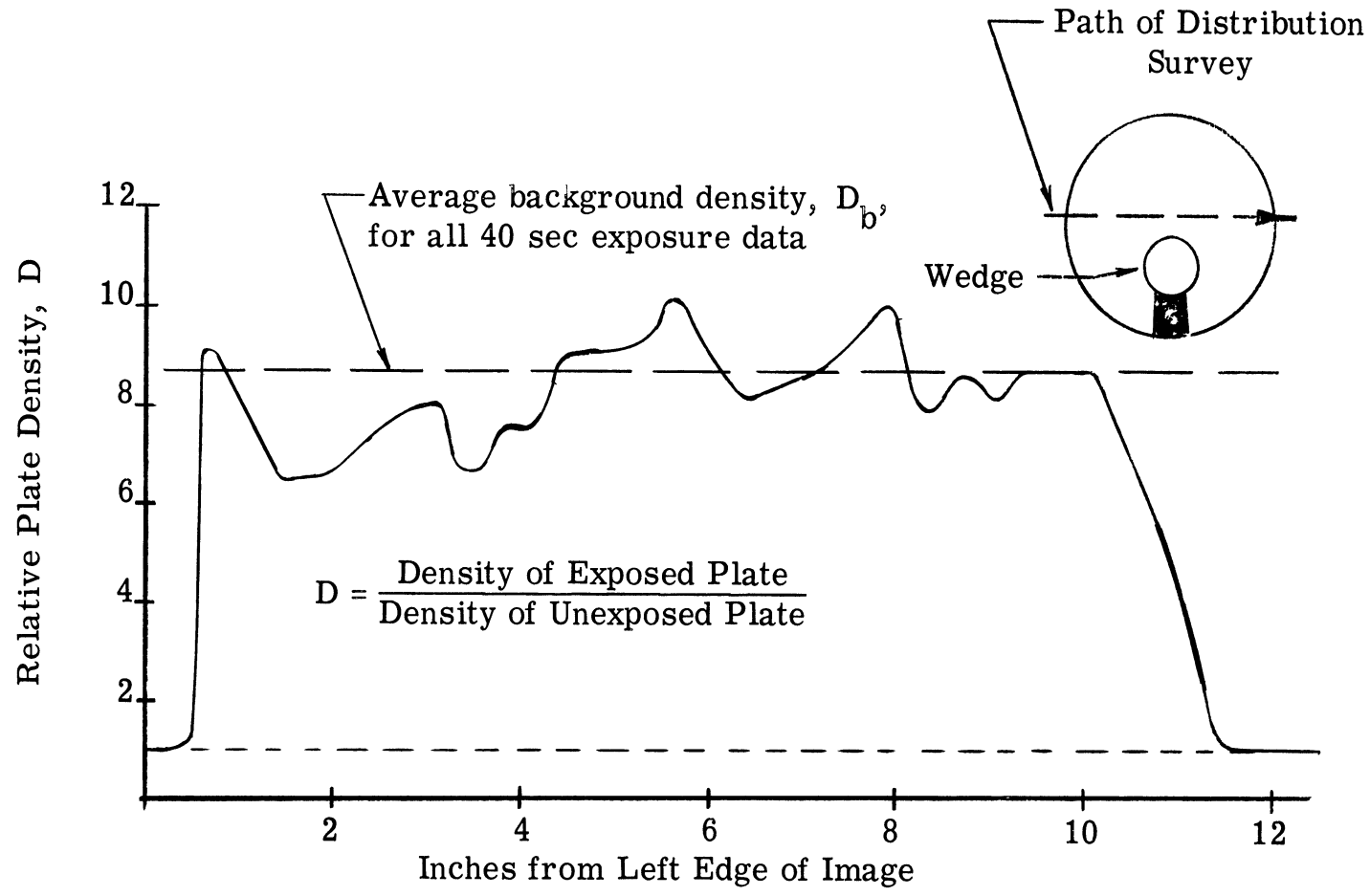

5a

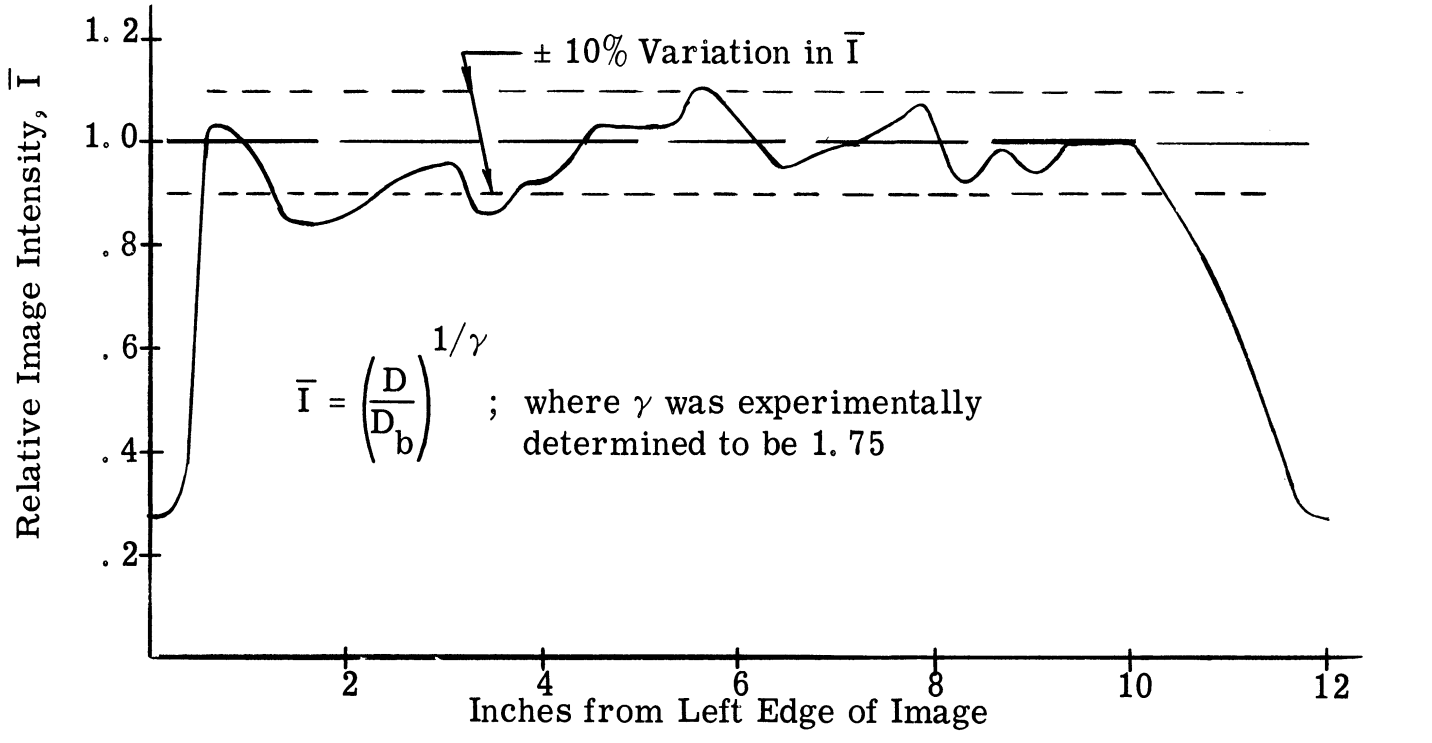

5b

Figure D-5. Typical Schlieren Evaluation Data
(5a. Relative Plate Density Distribution,
5b. Relative Image Illumination Intensity
Distribution)*

*40 sec exposure, 1.0×10^{-6} radian sensitivity.

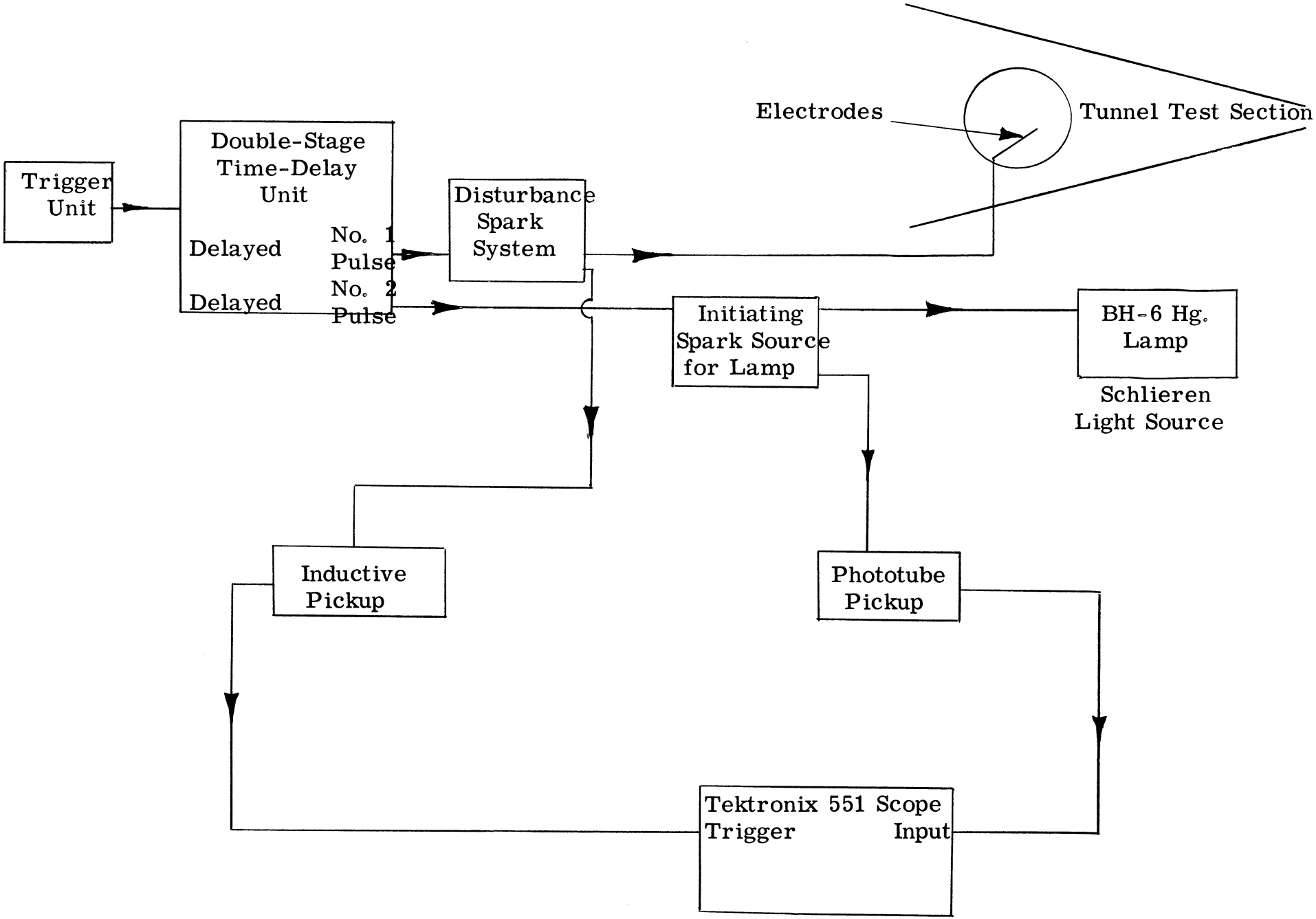

Figure E-1. Block Diagram for Sparks and Time Delay Measurement

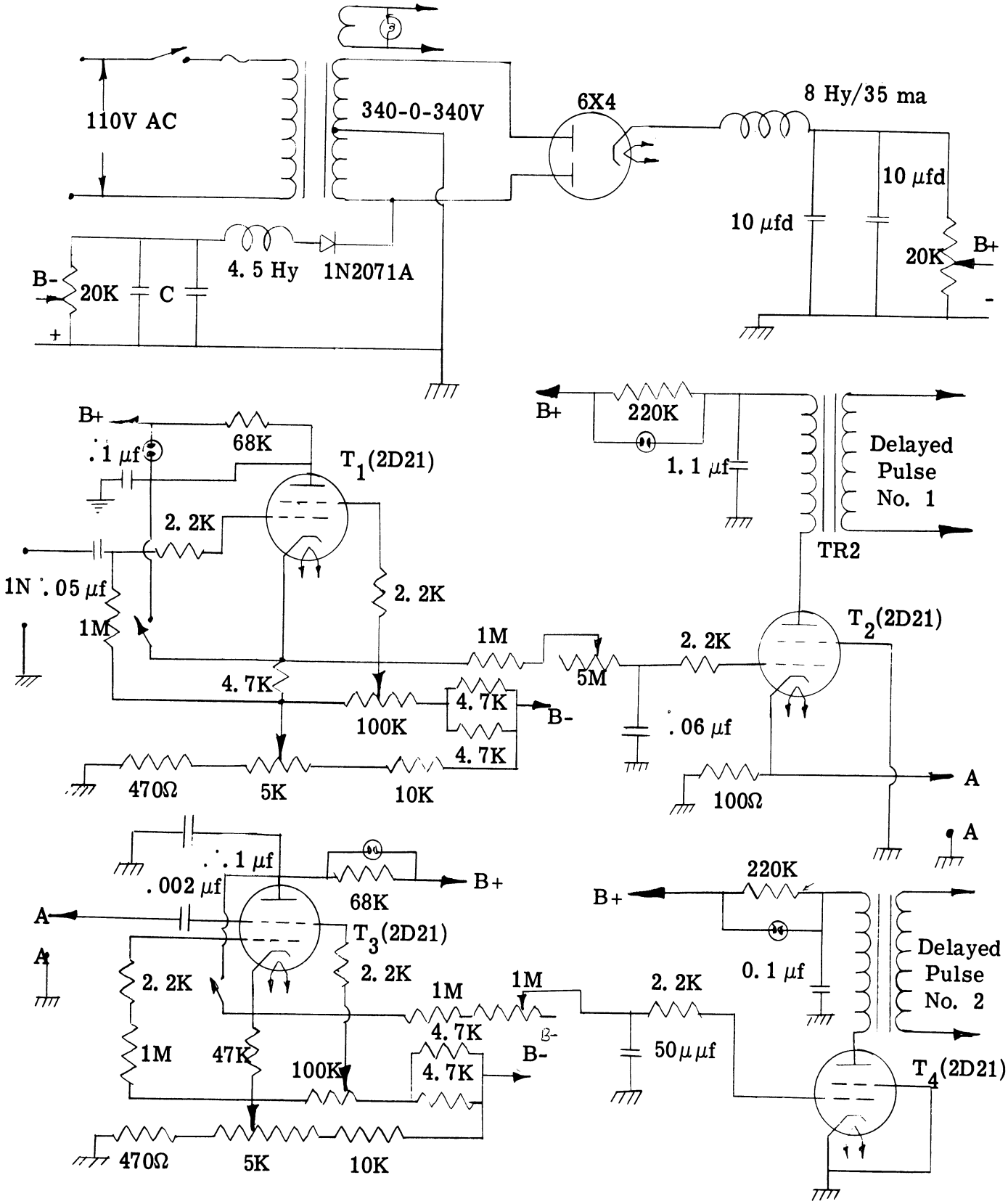

Figure E-2. Double Stage Time-Delay Circuit

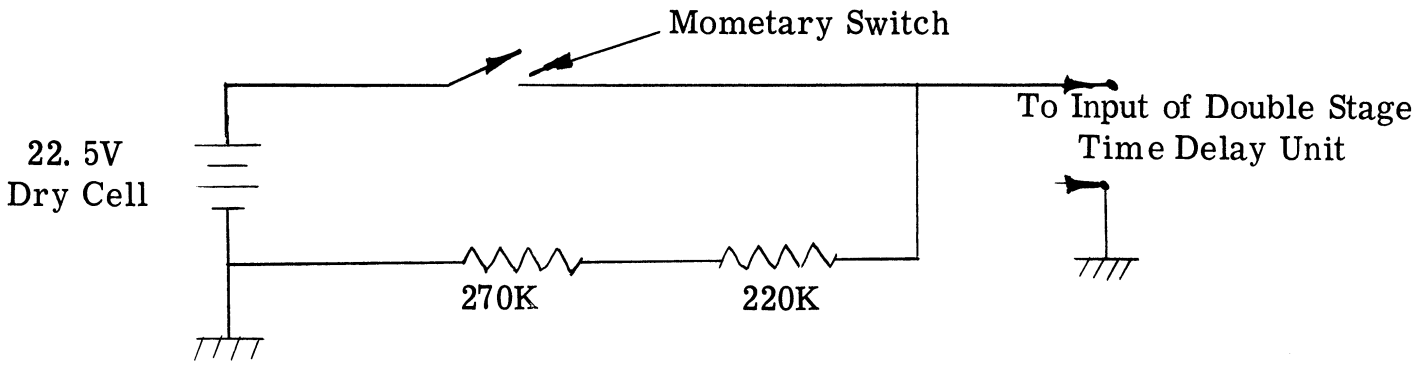

Figure E-3. Trigger Unit

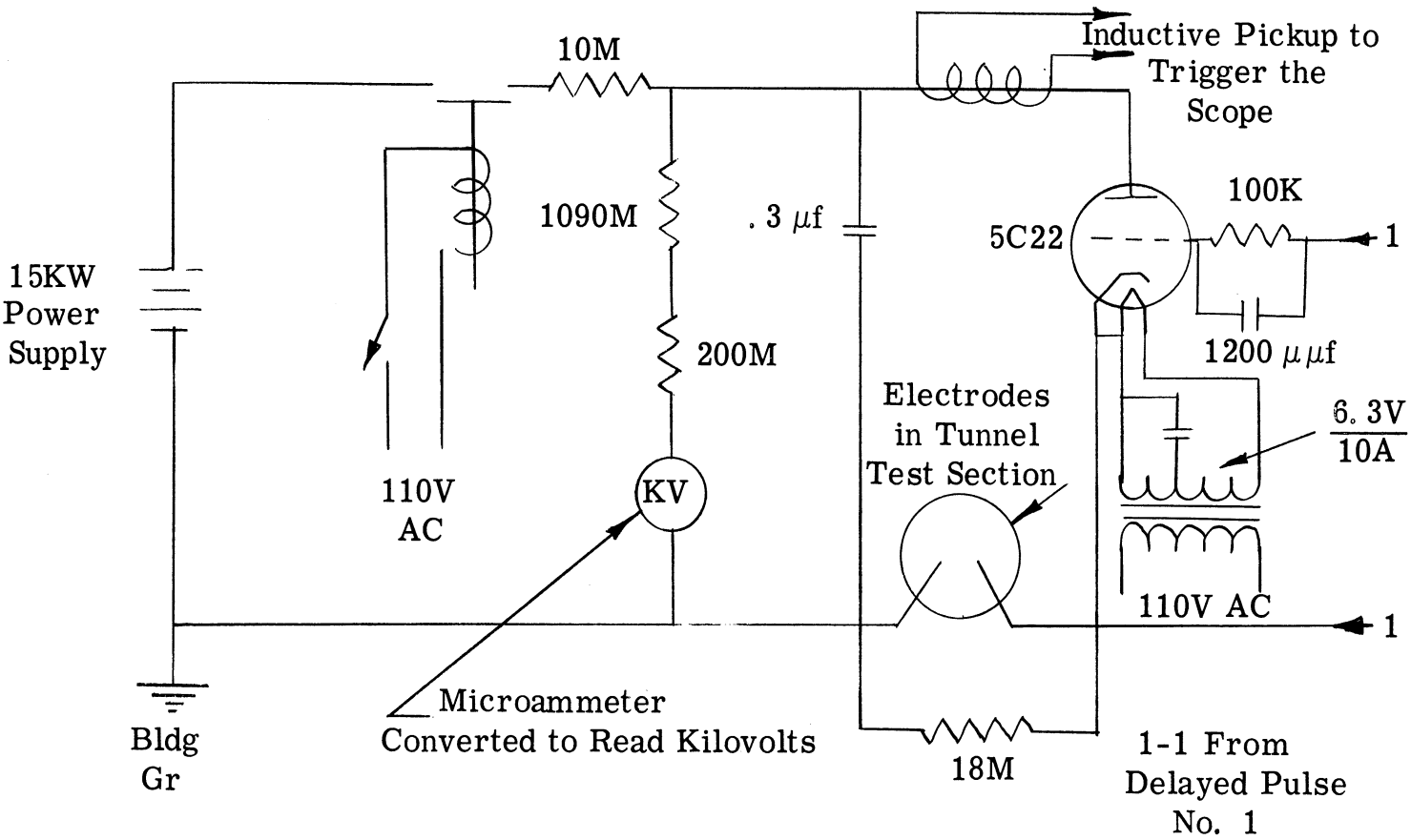

Figure E-4. Disturbance Spark System

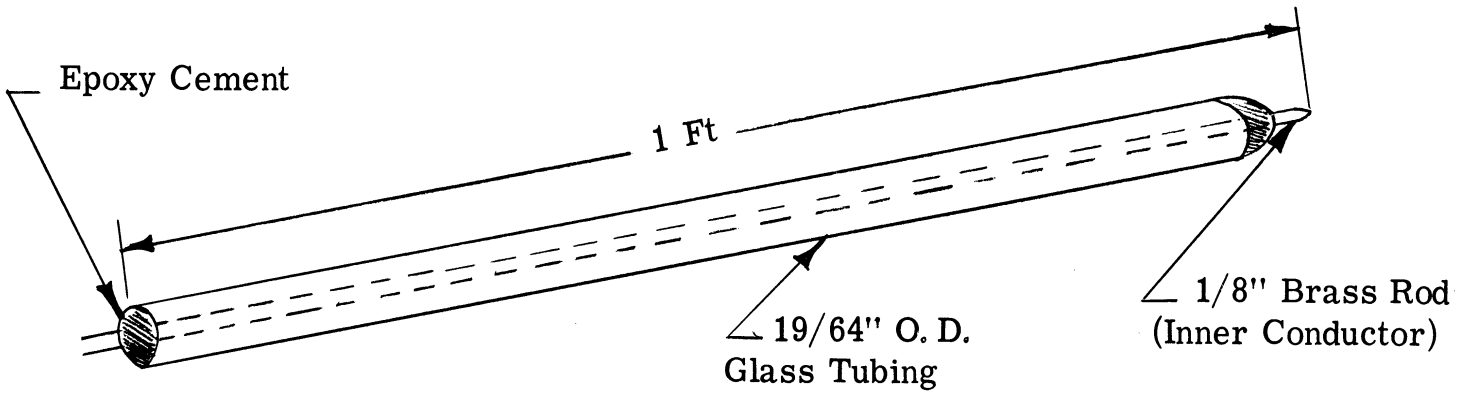

Figure E-5. Electrode Design

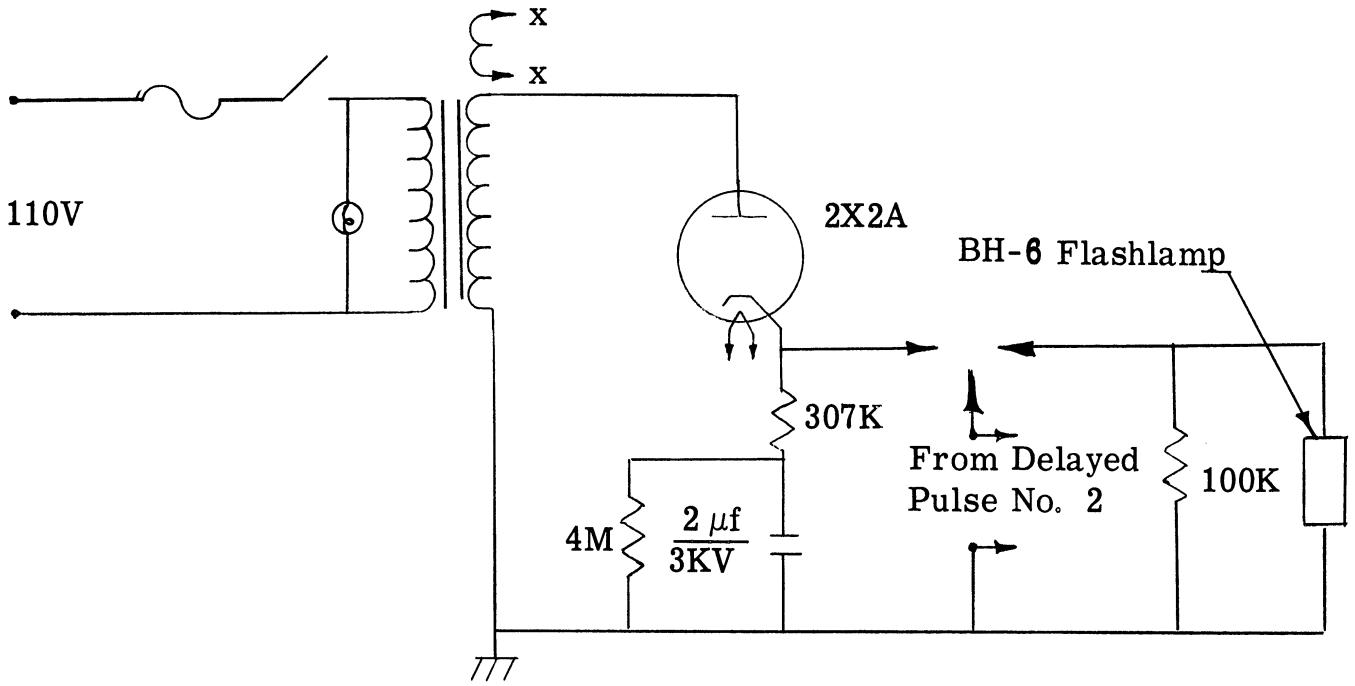

Figure E-6. Initiating Spark Source for BH-6 Mercury Lamp

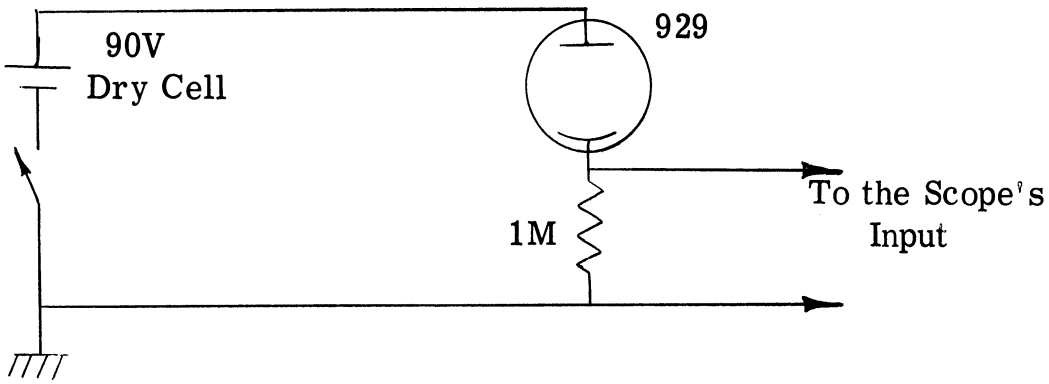

Figure E-7. Phototube Circuit

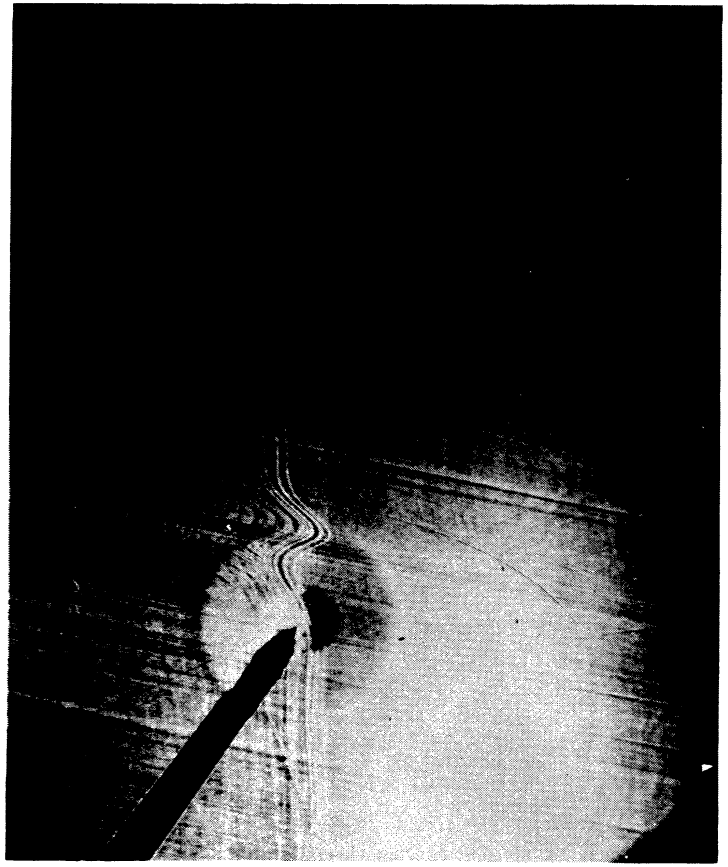

Figure E-8. Spherical Wave

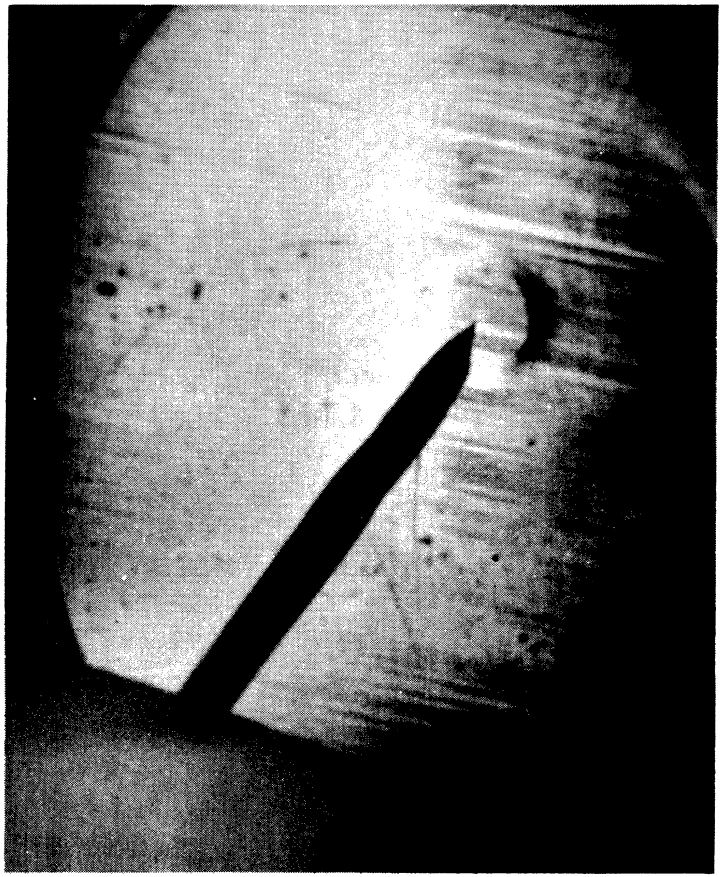

Figure E-9. Axial View of Cylindrical Wave

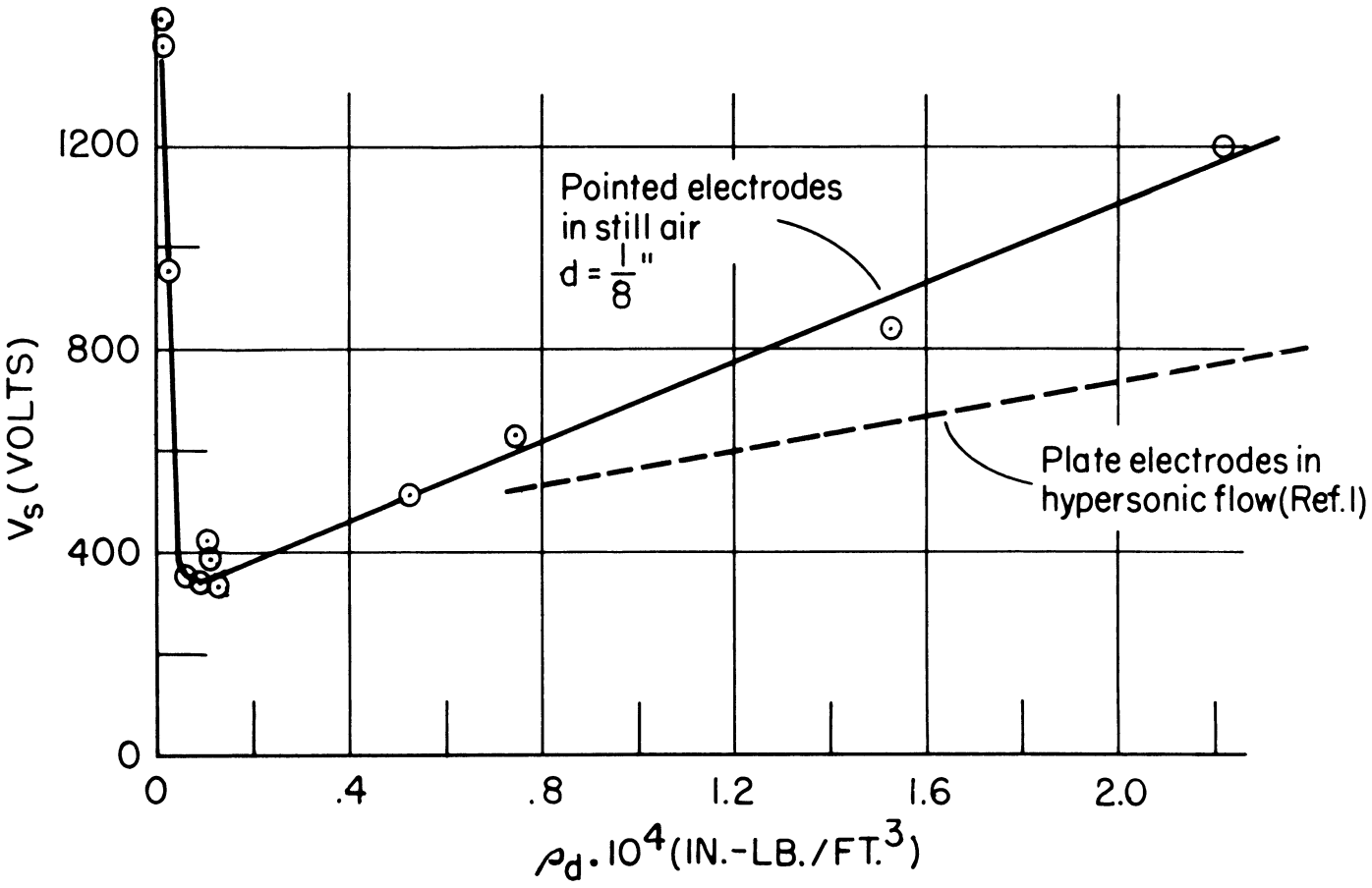

Figure F-1. Paschen Curve for Breakdown Voltage with Spark Probe

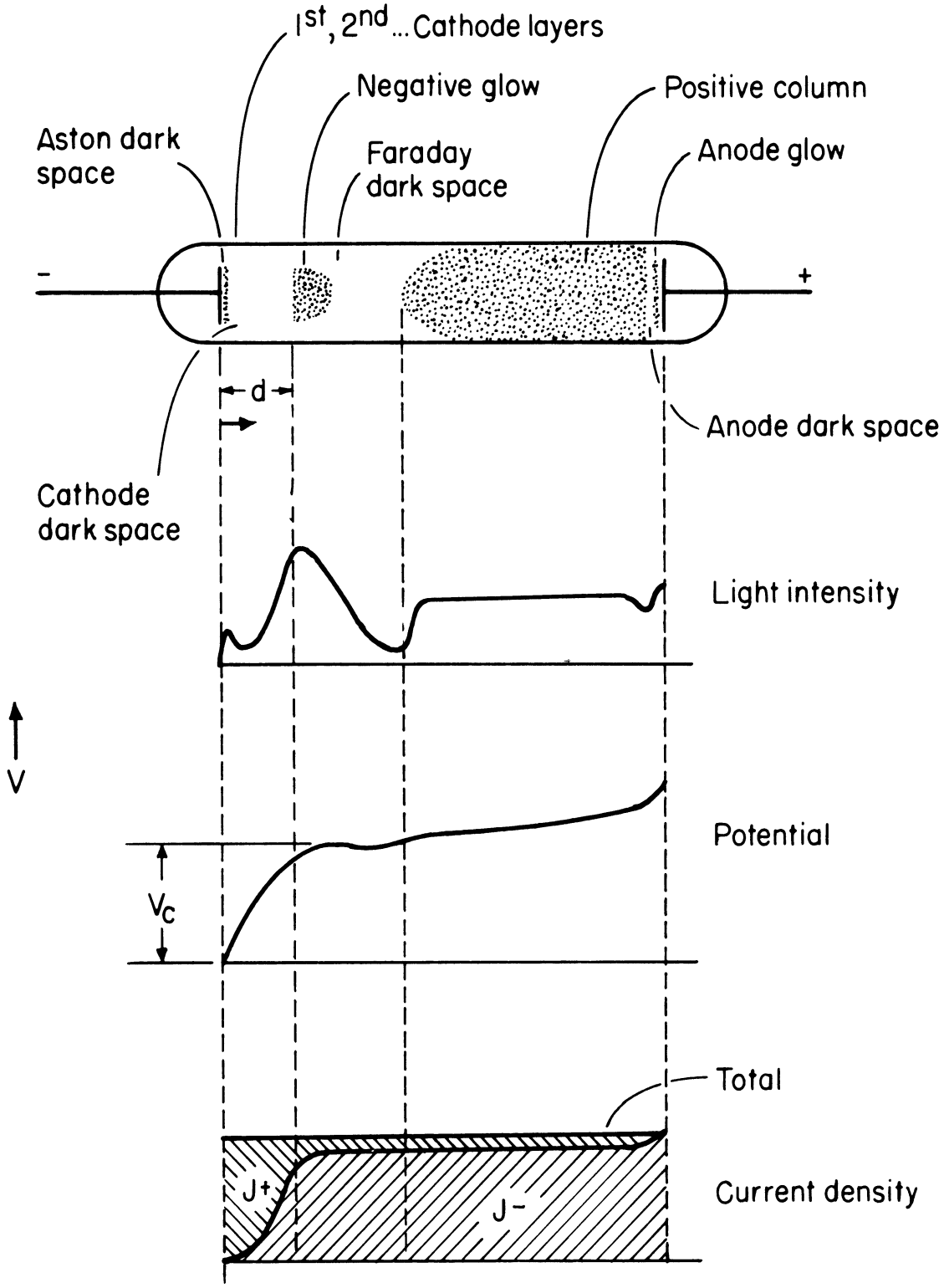

Figure F-2. Glow Discharge Tube and Variation of Glow Parameters (from Reference F-15, p. 56)

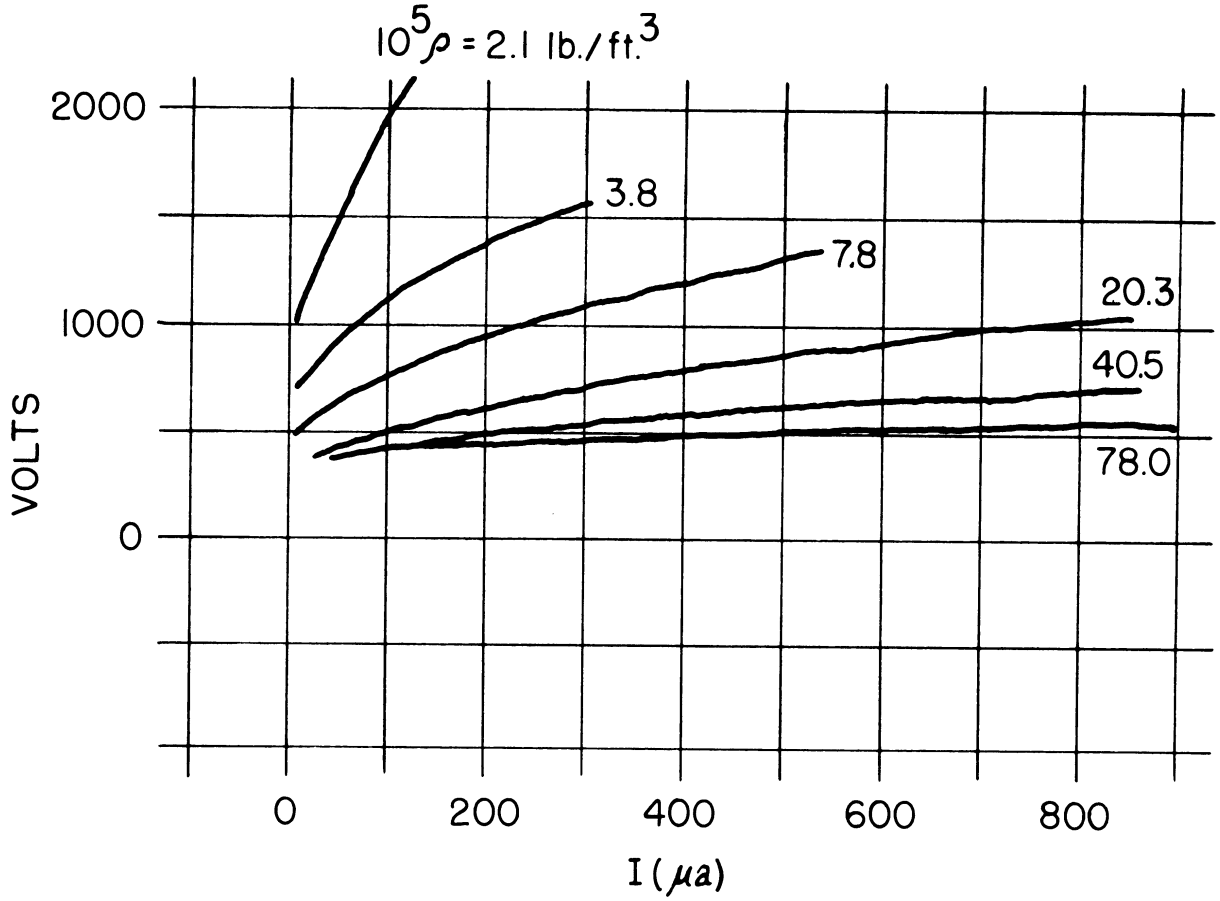

Figure F-3. Glow-Probe Dependence on Density

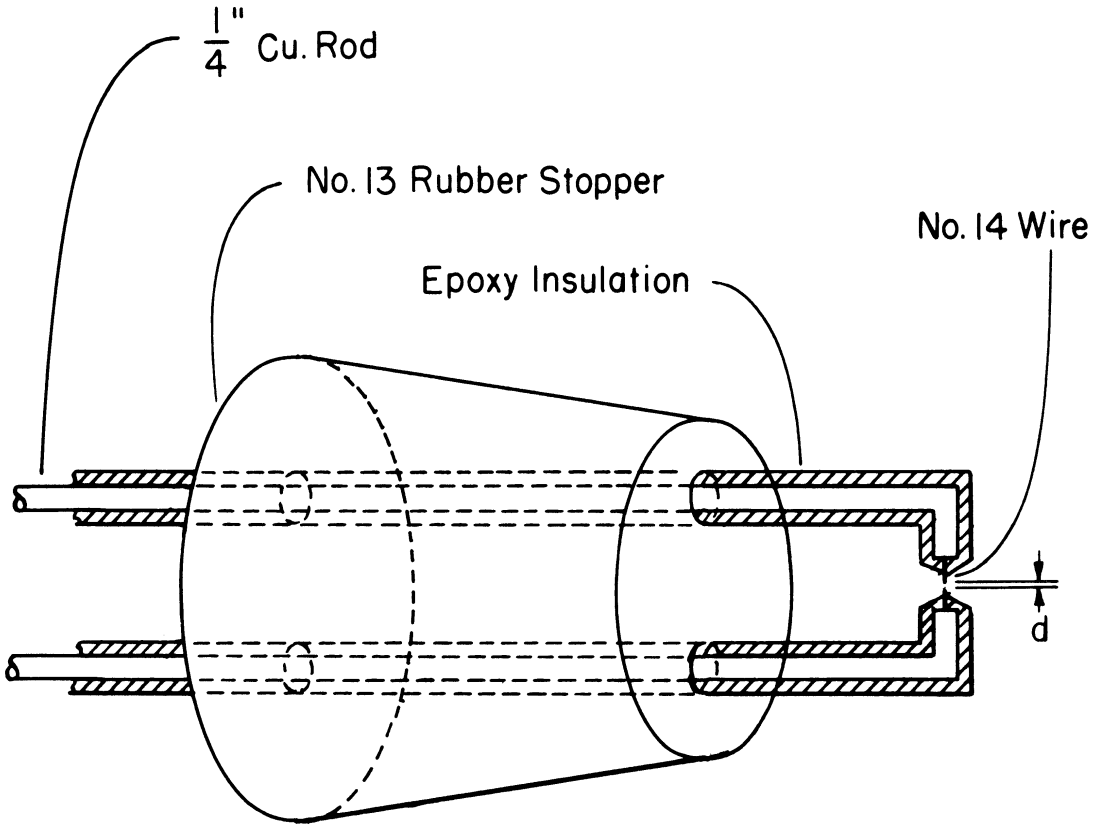

Figure F-4. First Spark Probe

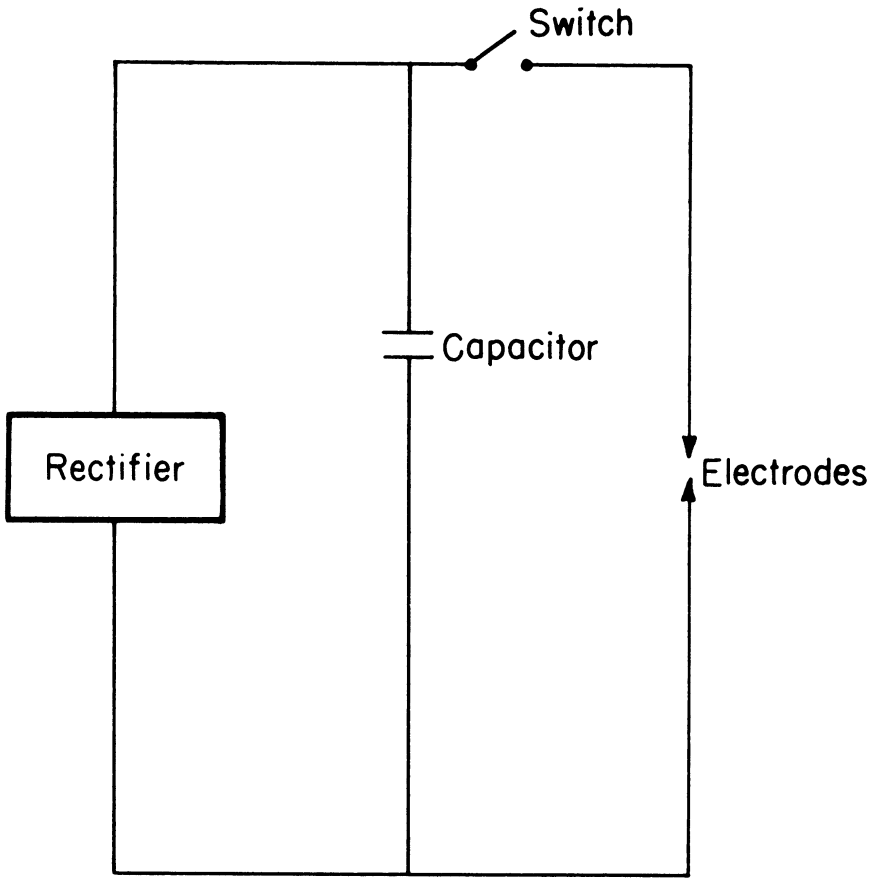

Figure F-5. Diagram of Circuit Used for Spark Probe

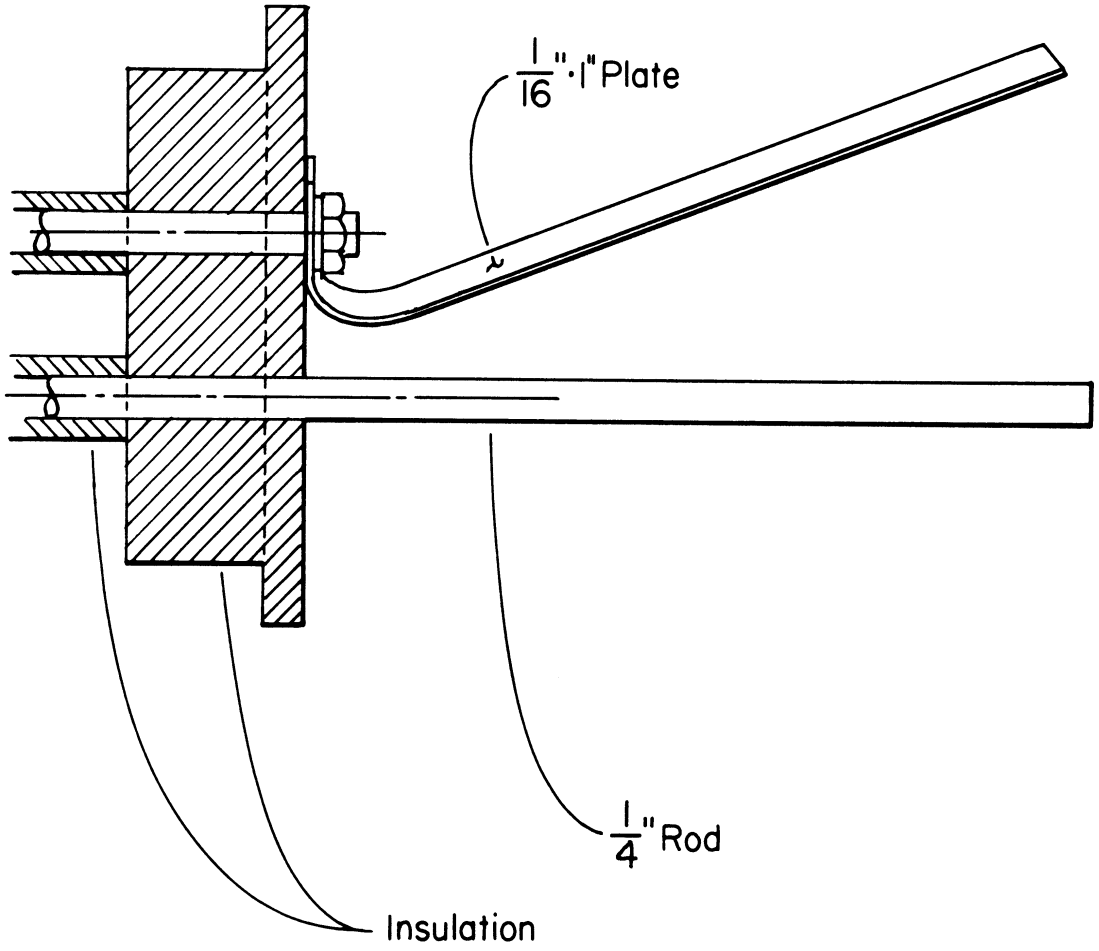

Figure F-6. Spark Probe Providing a Continuous Range of Possible Sparking Conditions

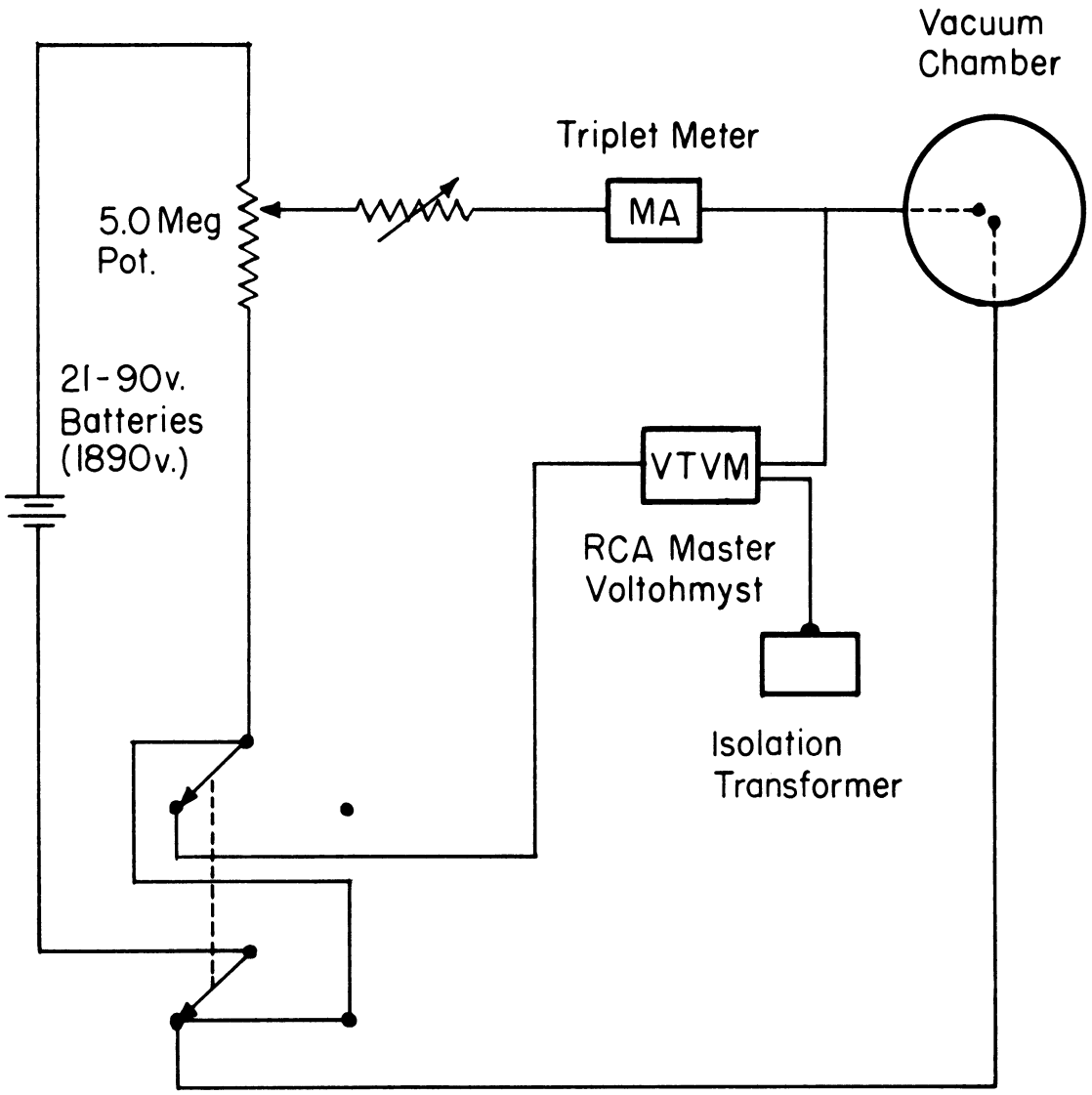

Figure F-7. Schematic of Glow Circuitry

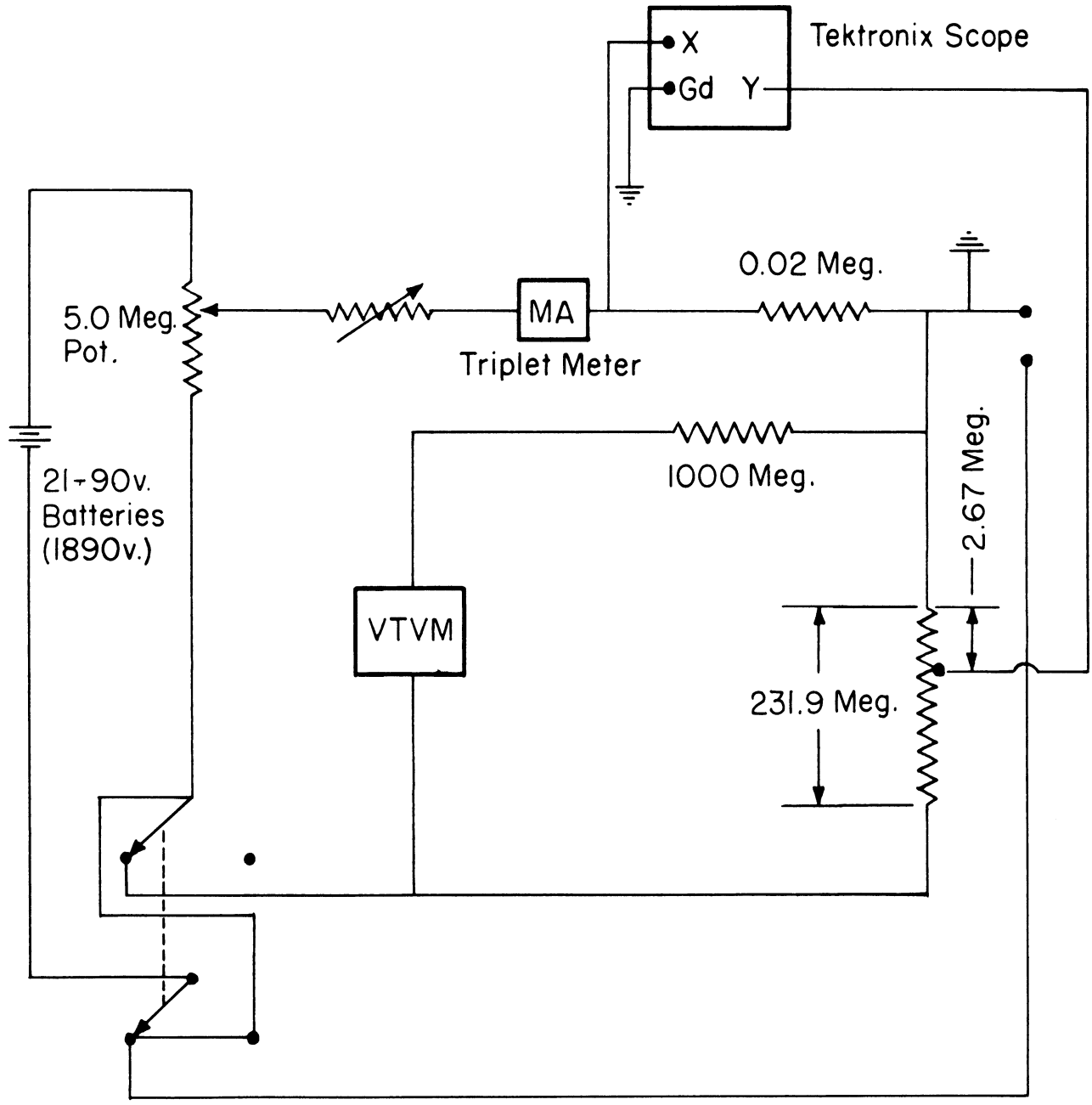

Figure F-8. Glow Circuit Diagram Showing Instrument Connections

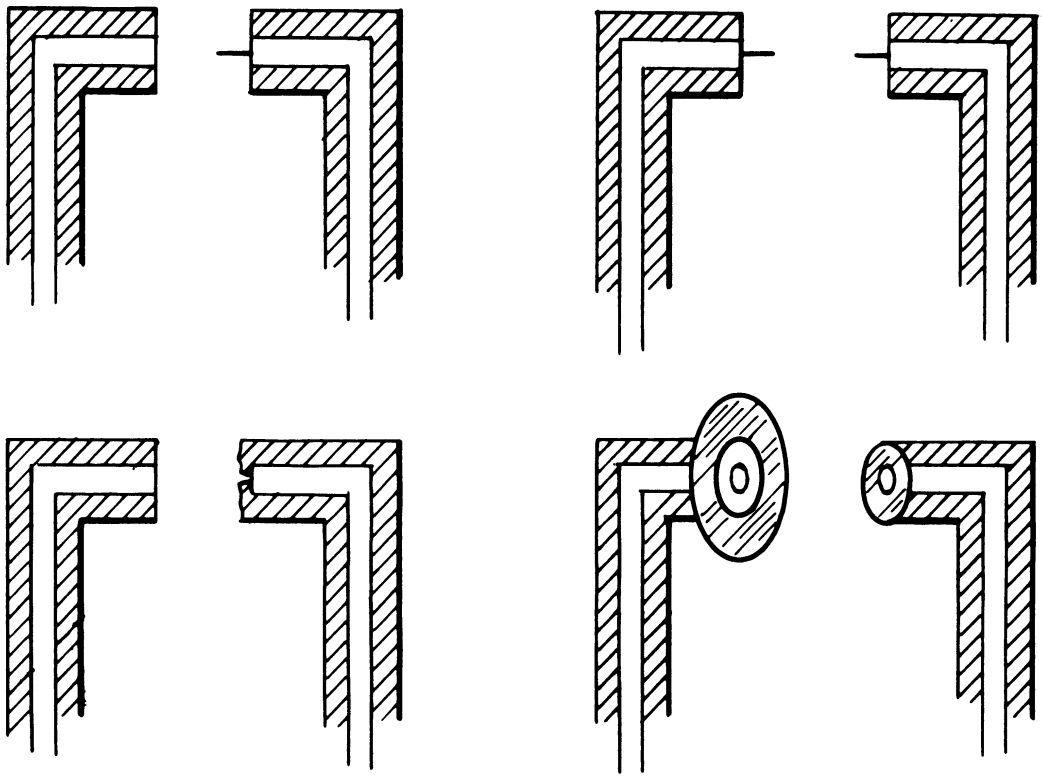

Figure F-9. Some Glow Probe Configurations Tested

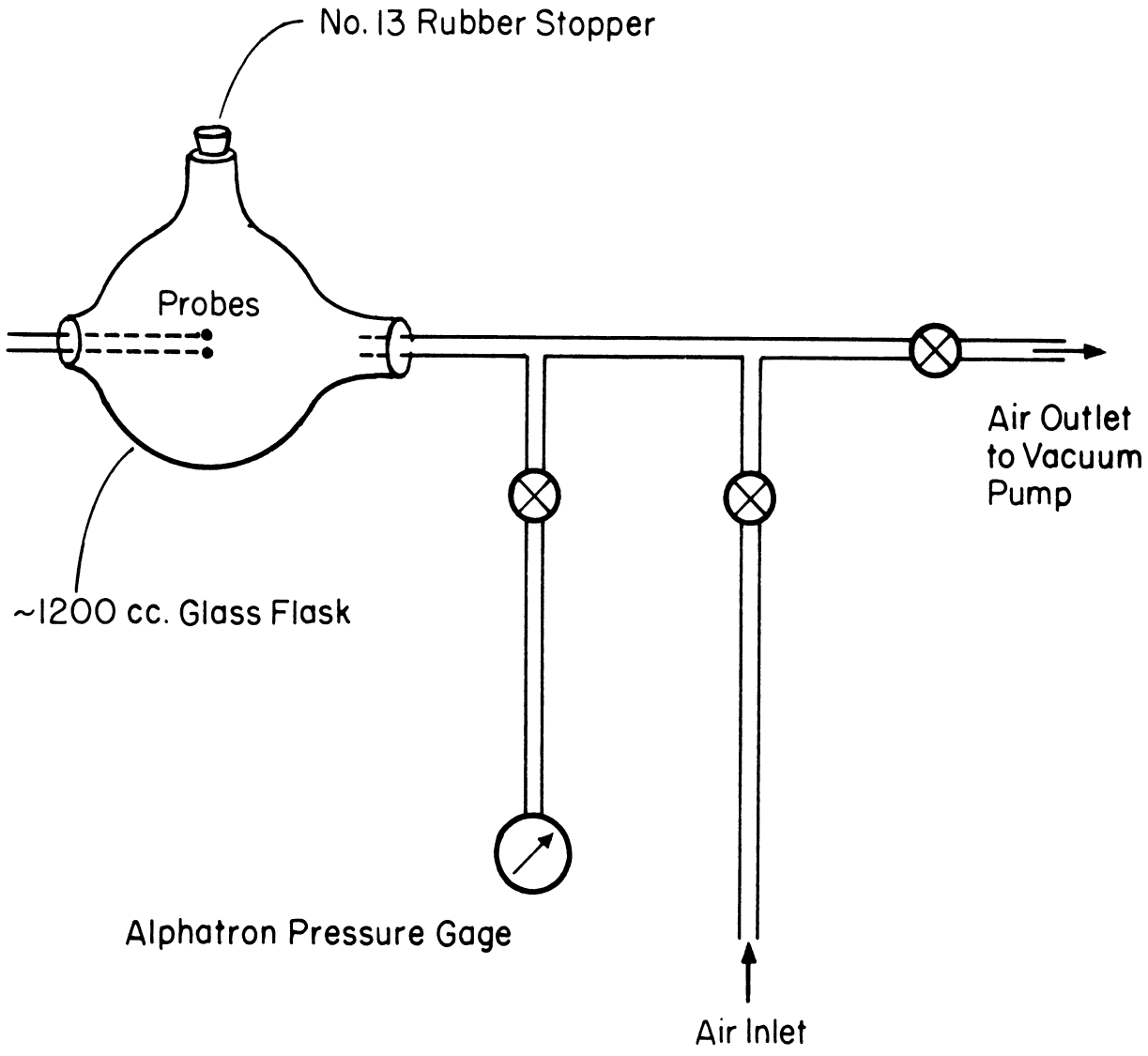

Figure F-10. Vacuum Chamber Setup

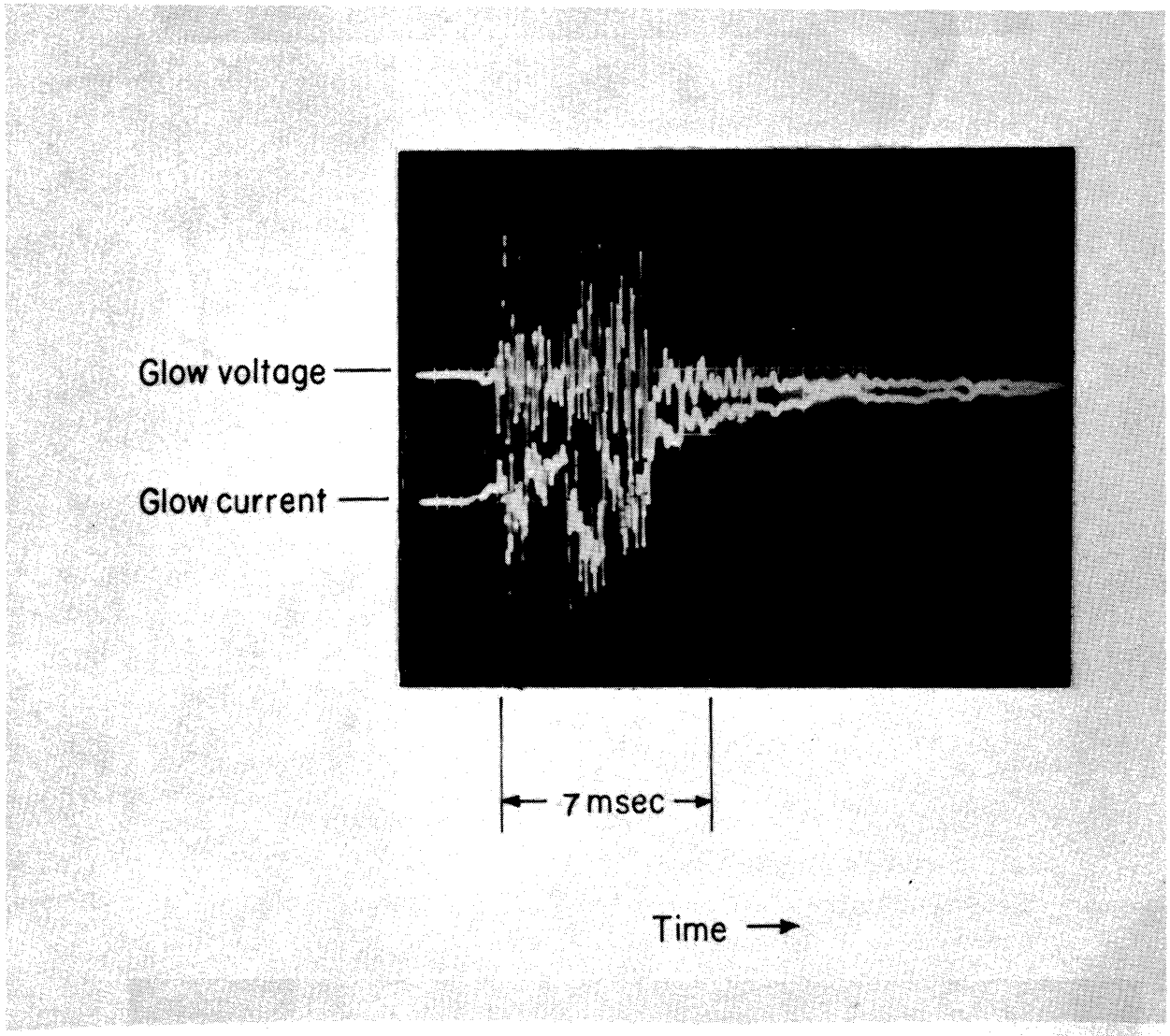

Figure F-11. Glow-Probe Time Response to Pressure Fluctuations